Faculty of Mathematics, Physics and Natural Science

Galileo Galilei Ph.D. School

XXIV Cycle

Ph.D. Thesis

Characterization and Performance assessment of read-out electronics for “On-Line”PET in hadron therapy dosimetry

Candidate:
Abolfazl Arabpour

Academic Supervisor:
Prof. Alberto Del Guerra
Academic Co-supervisor:
Dr. Nicola Belcari

Acknowledgments

I just finished up writing my thesis, and about couple hours away from submitting it. That would conclude one of the most important chapters in my life. However, writing this little section of acknowledgement seems much more difficult than I had expected. There are so many people who helped me out in many ways during my graduate school years. Listing them all in a piece of paper would be quite difficult. But that is not going to stop me from trying.

I thank my family for their relentless support. I would like to thank my mother and father for bringing me to this world and always being there for me. If anyone knows anything about my life, they would know that it has been a very bumpy ride so far. There are times when I was so lost that I almost gave up. But my parents would not let that happen and always have been there for me. My sisters have there for me too. I always wanted to thank them and let them know much I love them. I hope that they already know about it. Of course, I cannot leave out

I greatly thank my supervisor Professor Alberto Del Guerra and my advisor Dr. Nicola Belcari. Without their help, I would be nowhere right now. Nicola has been my mentor for last four years, and it has been a privilege working in FIIG group. Whether he believes it or not, I tried my best to be a good student. I think that he is one of the smartest person that I have ever met, and I hope to be like him someday.

I thank Professor Roberto Pani and Professor Sandro Squarcia for being in my defense committee.

Dr. Giancarlo Sportelli has been my friend who always has brilliant ideas for facing and solving problems. He will be my friend throughout my life at FIIG. Without his advice and help, I would not be graduating. Dr. Marco Aiello, Dr. Niccoló Camarlinghi and Dr. Sascha Mohers have been my colleagues in FIIG's group. They have been one of my best friends and also a good role model. I always try to copy what they do. I will miss countless nights that we sat in front of computer screens waiting for some amazing data to roll in. I hope that they know how much I appreciate their help.

Dr. Antonio Marinelli, Dr. Andrea Cintio and Dr. Bachir Buhadef have been my best friends in graduate school. I enjoyed having computer related conversions with them over lunch. They saved my life several times. I hope that I can still count on them. Dr. Luca Marradi also has been a good friend of mine along with my very first day of PhD school. He tried to teach me Italian language. I appreciate him that was so patient to me and always helped me in different issues. We had two nice trips together to Spain and we enjoyed times a lot.

I thank scientists at section INFN Pisa for taking care of me like I am one of their own. Mr. Fabio Morsani showed me many techniques in electronics. I thank engineer Magazzù for being my friend and helping out me for the designing a new board for the translator level. I cannot forget engineer Franchi with lots of experiences in electronics and his support.

I personally thank Professor Francesco Pegoraro (President of Galileo Galilei School), for his numerous advices and helps during my PhD.

I know that I left out some people whom I owe my appreciation to. But, I really need to submit my thesis pretty soon. So I will need to thank you in person. Finally, I have always thought that I can measure someone's success by looking at how successful their friends are. If I still believe that, I have been a very successful person, and I hope to keep it that way.

List of acronyms

BASTEI Beta Activity Measurements at the Therapy with Energetic Ions
CATANA Centro di AdroTerapia e Applicazioni Nucleari Avanzate, Catania, Italy
CFD Constant Fraction Discriminator
CRT Conformal Radio Therapy
CT Computed Tomography
DoPET Dosimetry with PET
EM Expectation Maximization
FoV Field of View
CFoV Center of FoV
FWHM Full Width Half Maximum
GSI Gesellschaft für Schwerionenforschung, Darmstadt, Germany
HIMAC Heavy Ion Medical Accelerator in Chiba, Chiba, Japan
HIT Heidelberg Ion Therapy center, Heidelberg, Germany
HT Hadron Therapy
IMRT Intensity Modulated Radio Therapy
INFN Istituto Nazionale di Fisica Nucleare, Italy
LET Linear Energy Transfer
LOR Line Of Response
LYSO ($Lu_{2(1-x-y)}Y_{2x}SiO_5 : Ce_y$, $x \approx 0.1$, $y \ll x$), Lutetium-Yttrium Oxyorthosilicate
LUT Look Up Table
ML Maximum Likelihood
OS-EM Ordinary Subset EM
PET Positron Emission Tomography
PMMA PolyMethyl-MethAcrylate
PMT Photo Multiplier Tube
PSPMT Position-Sensitive PMT
RBE Relative Biological Effect
SCD Symmetric Charge Division
SOBP Spread Out Bragg Peak
SPECT Single Photon Emission Computed Tomography

Contents

Out line of the project

The TPS[1] project is a flourishing case of collaboration of INFN, composed of twelve groups with physicists, radiotherapists and oncologists covering several different scientific aspects. Funding of the TPS project is partially provided by IBA. Applying "In-beam" PET monitoring is the participation of the Pisa group to this project derives from the experience accumulated by the group in Catania where proton therapy is applied in uveal melanoma treatment [1, 2, 3, 4, 5, 6, 7, 8].

Other ophthalmic targets, such as angiomas and haemangiomas have also been treated with protons with promising results [5]. A miscellaneous number of other ocular tumors are also treated with protons, such as retinoblastomas under general anesthesia and metastatic lesions [5].

The collaboration accounts for several INFN research groups, active in different scientific areas: experimental and theoretical / phenomenological nuclear physics, Monte Carlo calculations and techniques for numerical analysis, Radiobiology and Hardware / Software development for dose monitoring purposes. These groups are working together within the TPS project with the goal of developing an improved TPS for carbon-ion therapy with active scanning.

Radiotherapy with hadrons (protons and light ions), allows highly conformal treatment of deep-seated tumors with great accuracy and, while traveling through the patient, there is minimal lateral diffusion [9, 10]. Although the implementation of safety margins around the tumor and the selection of appropriate portal beams minimize over- or under-shooting effects, discrepancies between planned and actual delivered dose can be derived from patient set-up errors, anatomical variations or beam delivery among different treatment sessions. This is the reason why a direct verification of radiation field position and particle range would be very desirable for the quality assurance of the treatment. Many studies have shown that Positron Emission Tomography (PET) could fulfill this task adequately, by taking advantage of the spatial correlation between positron emitter (created along the hadrons' path) by nuclear interaction and dose distributions [11]. In fact, nuclear isotope cross sections fall off at low energy just a few millimeters before the Bragg peak, making it possible to obtain information on the delivered dose from the reconstructed spatial distribution of produced positron emitters.

At present, "In-beam" PET method is applied as a technique of treatment verification for fractioned carbon ion therapy at GSI, Germany [12], and is under evaluation for fractioned proton therapy at the Massachusetts General Hospital, Boston, USA [13] through the comparison of PET activity distribution predicted based on the planned dose and the measured one. Regarding the experimental aspects, a dedicated longitudinal tomograph has been developed in Japan [14]. However, commercial PET scanners have been employed [15, 16].

[1] Treatment Planning System

INFN-TPS Pisa group is developing a small PET instruments as a proof of principle toward the building of dedicated PET devices whose field-of-view (FOV) fits the patient-beam geometry and the size of the irradiated region. Toward the achievement of this objective in 2009, the performances of the DoPET[2] prototype developed at INFN-Pisa, were compared with another "In-beam" PET system at GSI Darmstadt, Germany. The two systems were simultaneously operated after low energy carbon ion irradiation of PMMA phantoms and some significant results have been achieved. Firstly, in the small field of view, the performances of our DoPET prototype were similar to those of the clinically established BASTEI[3] tomograph in terms of range resolvability, while exhibiting a superior spatial resolution due to the smaller crystal size. This supports its applicability to monitor treatment of small lesions in the case of carbon ion therapy. However, the limited geometrical detection efficiency as well as the required rejection of decay events in the first few minutes of irradiation penalized the counting statistics loosing the contribution of ^{15}O fraction [17].

Therefore, an upgrade the DoPET system is necessary. Providing an enlarged detection area with the availability of an external trigger signal in the acquisition system to tag the acquired data for real "In-beam" operation. Together with this development, a new treatment-planning system will be produced by the TPS collaboration and will be applied in hadron-therapy [18].

The value of the PET for hadron-therapy monitoring is assured by a detection capability of deviations equal to (or lower than) 1 mm in the dose distribution from the reconstructed image of the β^+-induced activity. Although the final aim of the "In-beam" PET is the determination of the delivered dose distribution, the primary goal for a proof of principle can be to reach a detection capability of deviations of the order of the millimeter for the proton range, i.e., only for one direction.

The goal of the thesis

This thesis has been addressing the hardware part of TPS project for the design, assembly and development of a PET scanner made of two detectors for dose monitoring in hadron-therapy treatment of patients. The aims of this thesis are:

1. The development of the detection system for gamma-ray-based multi-anode photo-multipliers (MA-PMT) and matrices of scintillators, which has been considered as the specific goal of the project.
2. Optimization of the acquisition system MA-PMT and in particular the development and optimization part of pre-amplification and discrimination of signals.
3. Testing the complete system for the physical characterization and determination of benefits in terms of spatial resolution and sensitivity.

This thesis is organized as follows. The first chapter reviews the rationale for hadron-therapy in treatment quality and briefly describes the reasons why hadron-therapy is used for cancer treatment. The second chapter shows the rationale for applying PET in hadron-therapy treatment and addresses the motivations of utilizing PET for monitoring the dose delivery in hadron-therapy in order to optimize the treatment. The third chapter discusses the basic concepts of PET. Chapter four presents the first version of our PET and shows the operational concept of our system with the different configurations. Chapter five presents the

[2]Dosimetry with Positron Emission Tomography
[3]Beta Activity meaSurements at the Therapy with Energetic Ions

upgraded version of our dedicated PET which includes the hardware part of project. Chapter six contains the measurements that have been done to verify the functionality and physical characteristics of the new version of our PET. Chapter seven demonstrates our PET system's set-up as a dedicated method for verification of correct dose, which is delivered by proton beam in Catania. Chapter eight illustrates and discuss the future work and provides some suggestion for the aforementioned system. There are also three appendices, which includes the explanation of the designed translator level for DoPET system when each head of the detection system composed of nine PMTs and the designation of a passive filter, applied to the DAQ boards as part of the acquisition system is illustrated including the simulation results.

Chapter 1

Rationale for hadron-therapy in treatment quality

1.1 Motivation of hadron-therapy

Radiotherapy is by far one of the most cost-effective modality for curative cancer treatment. As well as conserving tissue functions, it has a prominent role in symptom control and pain relief for incurable patients. With increasing cancer incidence and the impact of an aging population, the role of radiotherapy will become prominent.

At present, cancer is the foremost issue of social health in the world. Approximately 11 million people worldwide are diagnosed with cancer, and almost 7 million people die annually due to different type of cancers. In Europe, each year 1.8 million people die from malignant tumor growth and it is envisaged that cancer will become the leading cause of death in the next decade [19]. After heart disease, cancer is the second most common cause of death in the world.

In general, there are four diverse ways proposed for treating different cancers: surgery, radiotherapy, chemotherapy and immunotherapy. Today the first two are of crucial importance. Surgery and radiotherapy alone are successful in 22% and 12% of the cases, respectively. When combined they account for another 6% of the cases, so that radiotherapy is involved in almost half of the curative treatments of loco-regional type. For this reason, nearly one third of the 15,000 particle accelerators running in the world (30%) are devoted to radiotherapy [20].

Although the first therapy trial was reported by Prof. Freund in Vienna on November 24th, 1896 after irradiating and removing a hairy mole on the forearm of a patient [21], there was a 5 decade gap between the discovery of X-rays in 1895 and the invention of the first Linac in 1953. During these years, scientists (with the assistance of medical doctors) struggled to improve the quality of treatment of individuals that were suffering from different cancers. Medical doctors started using X-rays and Gamma rays in 1910 and with radium needles and ^{60}Co sources in 1951, thus beginning the practice of radiotherapy.

In order to overcome the drawbacks of exponentially decreasing depth dose distribution of electromagnetic radiation and to reduce the lateral beam scattering numerous techniques have been developed and

applied. The main objective of radiotherapy is the local control of the tumor and, in some situations, of the surrounding diffusion paths (loco - regional radiotherapy). The first step was to substitute X-ray tubes with high-energy gamma rays of ^{60}Co sources, which were produced in nuclear reactors. The rationale is to deliver the target tumor a sufficiently high dose so as to destroy it, while at the same time maintaining sufficiently low dose to the surrounding healthy tissues inevitably involved in the radiation. This dose must remain within such limits so that the healthy tissue does not undergo serious or even irreversible damage or complication.

Conventional radiotherapy delivers the maximum energy near the beam entrance, and deposits significant energy at distances beyond the cancer target. One of the effective step for the optimization of the treatment was applying IMRT[1]. Distribution of photon-bremsstrahlung of high-energy electron Linacs in several directions, giving better dose conformity and minimal energy deposition to the normal tissues. By using IMRT, it is possible to surmount the limitation of the exponential attenuation and absorption, and depth-dose characterization of X-ray radiotherapy. In contrast, heavy-charged particles like protons or heavier ions can be used to go over the physical and biological restrictions of the conventional radiotherapy. Ion therapy offers a promising future to those patients whose tumors cannot be treated by surgery or with conventional radiotherapy. Application of charged particles leads to a large reduction of at least 50% in the total energy (or integral dose) deposited in the body with a corresponding reduction in normal tissue damage.

Despite all of the potential advantages of the Charge Particle Therapy (CPT) compared with megavoltage X-rays, it is not without imperfections. Energy loss of the particles as they traverse a medium can alter the range, position, size and shape of the Bragg peak. These factors are detrimental as they reduce the conformity and dose distribution of the particle beam i.e. the advantage of using CPT. Range straggling occurs a s the number of interactions a particle undergoes varies as it travels through a medium, as some interact more and lose more energy and thus range is reduced [22]. This effect causes the peak to become blurred and reduces its accuracy by 1% of the Bragg peaks range [22]. Such an effect is especially detrimental if the target is adjacent to a critical structure e.g. optic chiasma particularly during single fraction treatments. Although photons may not be able to provide the desirable dose profile of CPT, its calculated and actual position are more likely to be equal and it is much easier to ensure the tumor is receiving the maximum dose as adjusting the Break Peak depth to account for this widening is much more difficult [23]. Particle interactions cause energy loss as they react with atomic electrons and nuclei in the medium. This leads to energy transfer to the medium, scattering of incident particle and in turn lateral scattering and beam divergence [22]. This effect is largely coulomb scattering of atomic nuclei and results in lateral scattering beam widening of the peak which reduces its accuracy for cancer therapy [24]. However, due to the divergence using a Gaussian distribution, it can be considered during treatments and is certainly provides a sharper beam than would be achieved with photons for superficial tumors and at lower energies [25]. However, the lateral penumbra deteriorates with depth and it is worse than that of photons. This suggests that protons are not suitable for deep-seated targets with adjacent critical structures [26].

Hadron-therapy is a comprehensive field that encompasses many different techniques of oncological radiotherapy. Protons, neutrons and light nuclei are examples of hadrons used to locally control many types of tumors. Proton therapy is considered to be a better treatment than even the best Intensity Modulated Radiation Therapies. Large tumors are, in particular, elective targets for hadron-therapy because with X-rays the surrounding tissues unavoidably receive a much higher dose. Heavy charged particles exhibit a superior dose distribution as compared to all conventionally used beams; a small lateral and range straggling, combined with an increase of the dose deposition with increasing penetration depth enables the production

[1] Intensity-Modulated Radio-therapy

of dose profiles precisely shaped to the contours of the treatment volume. In addition, heavy ion beams exhibit an elevated biological efficiency dose due to the maximum dose that is delivered to the tissue just over the last few millimeters of the particle's range; this maximum is called the Bragg peak. Therefore, beams of heavy ions deliver a high physical dose combined with a high biological efficiency to a tumor volume while the surrounding healthy tissue is maximally spared. Moreover, the dense column of ionization produced near the Bragg peak of a light ion track gives rise to many DSBs[2] and MSDs[3], when it crosses the DNA of a cell nucleus.

The possibility of using hadron-therapy (with protons or heavier ions) in every day clinical practice in cancer therapy, as a consequence of the worldwide fast growing of new proposals and facilities [9], requires an improvement of treatment-dedicated software including the development of new approaches able to provide a more accurate simulation of the interaction of radiation with biological tissue.

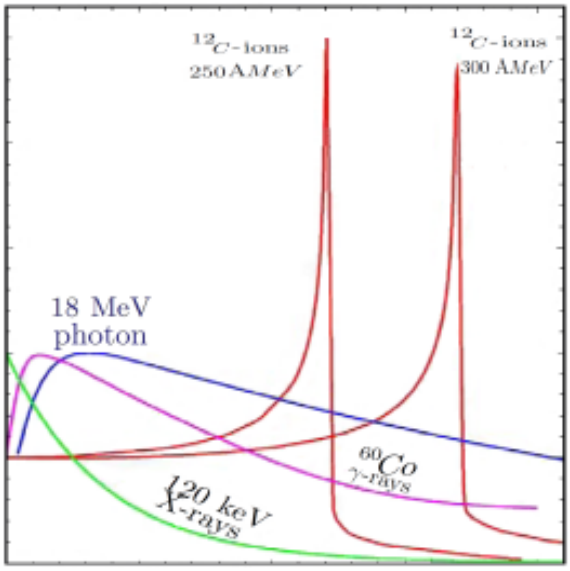

Figure 1.1: Comparison of the depth dose profiles of 120 keV X-rays, gamma of ^{60}Co, and Rontgen-Bremsstrahlung photons (E_{MAX} = 18 MeV) with carbon ions of 250 MeV/u and 300 MeV/u [27].

It is obvious that by increasing the ionization density towards the end of the particle track, there is a capability of transporting a higher dose to a deep-seated tumor than by using conventional photon beams (as it shows in Figure 1.1). As turned out in practice the small lateral scattering of heavy particles as well as the restricted range (i.e., the steep decrease in dose beyond the Bragg maximum) are the essential properties of particle beams which serve to improve radiotherapy. In addition, at a microscopic scale the increase in ionization density towards the end of the particle range causes an increase of biological effectiveness for ions heavier with respect to protons that can be used to potentiate the radiation damage selectively in the target volume when using the appropriate ion species like carbon [28].

[2]Double Strand Breaks
[3]Multiple Damage Site

1.1.1 History of hadron-therapy

The field of radiation treatment of cancer was founded by the Lawrence brothers when they employed X-rays for treatment of uterine cancer of their mother in 1937. By late 1938, they began using RT therapy in patients and a big program for the treating of 250 patients was initiated in 1940. In 1946, Harvard physicist Robert Wilson first suggested proton therapy [29]. He went on to support this idea by showing that proton therapy can place the maximum radiation dose in the tumor without harming surrounding tissues. He also showed that for larger tumors, the normally narrow Bragg peak could be spread out by using a modulator wheel. Following this publication, research on proton therapy began in 1954; the first proton therapy treatment was performed on a pituitary tumor at the Berkeley Radiation Laboratory. Between 1954 and 1974 at Berkeley, about 1000 pituitary glands and pituitary tumors were treated with protons.

In 1957, the first tumor was irradiated with protons at the Uppsala cyclotron [30] but the facility that made the largest impact on the development of proton therapy is the Harvard Cyclotron [31]. In 1958, protons were used in Sweden as neurosurgical tools and in 1967, large-field proton treatment was also used in Swedish facilities [32]. In 1968, the Dubna proton facility center was established and the year after, work began in the Moscow proton facility. Neutron therapy initiated at MD Anderson in 1972 and two years after that, Large-field fractionated proton treatments program began at HCL[1], Cambridge, MA. In the same year patients were treated with pi mesons at Los Alamos. St. Petersburg proton therapy facility center started its activity in 1975. In the same year, Harvard team pioneers started to treat eye cancer with protons. In 1976, neutron therapy was initiated at Fermi lab and the next year, Bevalac at Berkeley investigated ion treatment of patients. By the time the Bevalac facility closed in 1992, 223 patients had been treated. In 1979, proton therapy started in Chiba, Japan. In 1988, proton therapy was approved by FDA. In 1989, proton therapy was established at ClatterBridge and the year after that, the first hospital-based facility at Loma Linda in California was set up. In 1991, proton therapy started at Nice and Orsay and subsequently, Berkeley cyclotron closed after treating more than 2,500 patients. In 1993, proton therapy center opened at Cape Town and in the same year, Indiana started treating the first patient with protons. In 1994, ion therapy with carbon started at HIMAC [2] (and by 2008 more than 3,000 patients had been treated). In 1996, the PSI proton facility was established and two years after that, Berlin proton facility was launched. In 2001, Massachusetts General opened its proton therapy center, and in 2006, proton therapy was initiated in MD Anderson, and finally in 2008 neutron therapy was re-stated at Fermi lab [33].

By the end of 2007, around 54,000 patients had been treated with proton beams in a dozen subatomic physics laboratories and in about five hospital-based proton therapy centers. Another ten centers are running-in or are under construction in the world. By the same time, around 4500 patients had been treated with carbon ions at the HIMAC in Chiba, Japan and about 400 at the pilot project at the nuclear physics laboratory GSI in Darmstadt, Germany. One of the therapy centers was MGH-Harvard where has studied the survival rate of the patients who suffered from the Sarcoma of the skull base tumors under the proton therapy treatment. Due to the analysis of results which has been done on those patients with sarcomas of the skull base, the indicators of a 10-year survival rates after proton therapy were achieved which were equal to 95%, however, a statistics of 45% was obtained with the same number of patients in the GSI (Darmstadt, Germany) after the treatment with photon. These results verify the benefits of proton therapy compared to photon. The other therapy center, the HIT, Heidelberg Ion Beam Therapy Center, Germany), has reported almost 100% survived patients within 5 years of observation. They suffered from the Carcinoma of the prostate. Therefore, There were excellent results [10, 35, 36].

[1] Harvard Cyclotron Laboratory
[2] Heavy Ion Medical Accelerator

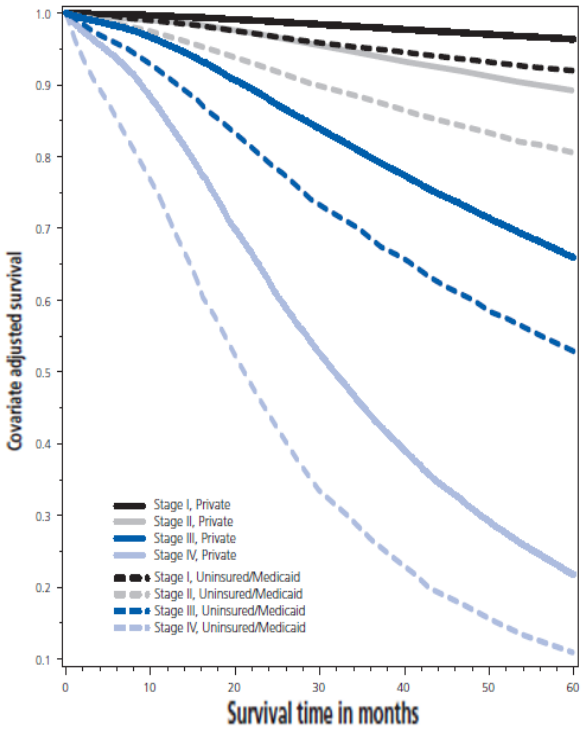

Figure 1.2: Different cancer survival among patients ages 18-64 years by Stage and Insurance Status at the end of 2008 [34].

In the past five years, European initiatives at GSI and CERN have made important steps in joining Japan in the development and construction of hospital-based dual centers for protons and carbon ions. Based on the successes of the pilot project, the Heidelberg Ion Therapy (HIT) Center designed by GSI was approved in 2001 and first treatment took place in 2008. The construction project of the Italian National center CNAO started in 2002 and the first treatment of patients is planned for 2011. Further centers are under construction or planned Marburg in Germany, Wiener Neustadt in Austria and ETOILE in France [36].

Industry has shown considerable interest in the upcoming market of hadron-therapy. Five companies (IBA, Siemens, Hitachi, Optivus and Varian-ACCEL) are now selling proton therapy units, and two firms (Siemens and Hitachi) have designed facilities for combined proton-carbon beams. The strong interest of industrial companies in ion therapy is supported by the large potential of this strategy for curing cancer, which is often rooted from the instruments developed for fundamental research in subatomic physics.

Proton therapy is booming, with about 50,000 patients treated worldwide. Several dedicated hospital-based centers with significant capacity for treating patients are now replacing the first generation $R\&D$ facilities hosted by the physics research laboratories. In Europe proton therapy centers for deep-seated tumors exist at Orsay in France, at Munich in Germany, at Uppsala in Sweden, at Villigen in Switzerland. Various facilities exist in Catania (Italy), which produces lower energy proton beams to treat eye melanomas. Today, five companies offer turn-key centers and about ten new centers are under construction around the world. However, less than 1% of the patients have been irradiated with the more technologically advanced active scanning techniques, which are an exclusive European contribution developed recently at PSI in Villigen for protons and at GSI (Darmstadt) for carbon ions.

1.2 Physical rationale for applying hadron ions in RT

Radiotherapy with Hadrons is primarily different from conventional radiotherapy. The interaction of protons with matter is the basis for the therapeutic potential of these beams. When a proton beam interacts with tissue, most of its energy is lost by collision with atomic orbital electrons. Since the proton is some 1835 times more massive than the electron, it does not significantly deviate from a straight-line path as it interacts, slows down and eventually stops. The proton deposits energy with an energy loss inversely proportional to the square of its speed.

The favorable depth dose distribution is a direct consequence of the interaction mechanism of heavy, charged particles with the penetrated material and is different from that of electromagnetic radiation. Within the energy range used for therapy, heavy charged particles interact predominantly with the target electrons and the interaction strength is directly correlated with the interaction time. At high energies of the projectiles, the interaction time is short and the energy transfer to the target small. When the particles are slowed down and close to the end of their range, the interaction time becomes larger and the value of the energy transfer is at its maximum. The energy loss as function of particle energy and atomic number is given in the Bethe-Bloch-formula [37, 38, 39]:

$$\frac{dE}{dx} = \frac{4\pi^4 e^4 Z_{eff}^2 N}{m_e v^2} \ln \frac{2mv^2}{I(1-\beta^2)} + relativistic\,terms \tag{1.1}$$

where m_e is the electron mass, v the projectile velocity, N the density of the electrons of the target material, e the elementary charge, and I the mean ionization potential. Finally, Z_{eff} is the effective charge

empirically approximated by Barkas [40]. The relativistic terms in Eq. 1.1 will be described in Eq. 1.2. For high energies, all electrons are stripped off the projectile and the effective charge equals the atomic number. At low energies, electrons are collected from the target and the effective charge decreases, yielding zero when the particles stop. The change of Z_{eff} is the main reason for the sharp decrease of the energy loss at lower energies, which is the essential criterion for the use of heavy particles in therapy.

Hadron-therapy benefits from a more selective energy deposition in depth with respect to conventional radiotherapy. The superior dose con-formality offered by this modality demands a higher accuracy in the planning and delivery of the treatment. This has led to a growing interest in quality assurance techniques such as “In-beam” PET during the irradiation, and “Off-beam” PET soon after the irradiation.

1.2.1 Lateral and longitudinal scattering

When the energy loss is plotted over the penetration depth a Bragg curve for a single particle results in a dose ratio from plateau to peak of 1 to 2 orders of magnitude. However, measured Bragg curves have a much lower dose ratio due to the statistics of the energy loss process. The interaction of the projectile with the electrons is a process involving many collisions and most of the differences in the individual energy transfer are compensated but yield a small straggling of the particle range [41, 42]. Range-straggling broadens the individual Bragg curve and decreases the peak to plateau ratio. Because this process strongly depends on the atomic number of the projectiles, the Bragg peak is always broader for protons than for carbon ions. In fact, this is rather irrelevant for therapy because the tumors to be treated are larger than the natural width of the Bragg peak and various methods are now being used to extend the Bragg region over the size of the target volume. Only at the distal side of SOBP[1], the natural decay is visible. Dose distribution with depth has been shown in Figure 1.3. It exhibits a strong Bragg peak towards the very end of the range, beyond which the dose very rapidly falls to zero and on the proximal side of which, the dose is only some 20% of the peak dose.

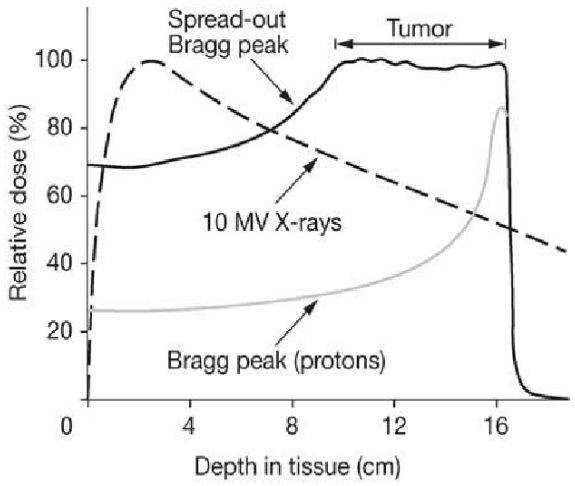

Figure 1.3: Depth-dose curve for an un-modulated and a modulated 160 MeV proton beam, compared with that for a 10 MV x-ray beam. The advantage of the proton beam is the complete absence of dose beyond the Bragg peak and the avoidance of surface dose [43].

[1] Spread-Out Bragg Peak

In 1904, Bragg and Kleeman observed the pattern of dE/dx and by this observation it has been clarified that by irradiating a target by photons the dose proximal to the target is higher than the target dose and the distal dose is non-zero; when the irradiation of the proton is applied to the target the dose proximal to the target is now lower than the target dose and the distal dose is absolutely zero. This is the fundamental advantage of proton therapy. This arrangement is ideal for radiotherapy if a target can be arranged to coincide with the Bragg peak. To give a quantitative feeling for this, the range of 160 MeV protons in tissue is about 16 cm and the width of the Bragg peak at the 80% level is only 7 mm [43]. About $1-2\%$ of the energy loss arises from collisions with the atomic nuclei during which a much larger fraction of the proton's energy is transferred to the medium. This causes a high LET[2] and in turn a higher RBE[3] than the electron-collision component which is identical to that of X-rays (RBE = 1).

A commonly adopted value for the RBE of a proton beam is about 1.1, determined from clinical studies with fractionation [44]. A commonly used unit is the CGE[4], being the dose in proton gray multiplied by 1.1, which gives the dose in cobalt gray [45].

Because the RBE for protons is similar to that of X-rays, conventional X-ray clinical experience can be translated into proton-therapy management. Therefore, protons present a challenging opportunity to improve conformal radiotherapy due to the better dose distributions which can be obtained [46], and the slightly enhanced RBE. Because dose distributions can be more tightly conformed to the target volume, dose escalation can be practiced [47].

1.2.2 Inelastic interaction with atomic electrons

Inelastic interactions with bound atomic electrons represent the principal process by which protons lose energy along their trajectory at the energies and in the materials of clinical interest, creating atomic excitation or ionization, as well as a small deflection of the incident proton. Although it is possible for electrons to lose a large fraction of their energy and be deflected through large angles in an inelastic interaction, the energy transferred by protons at each interaction is always small, the maximum possible value being approximately $4m/M$, where m is the rest mass of the electron and M is the rest mass of the proton. The amount of energy transferred in each interaction has a probability distribution, which results in energy and range straggling after passing through a given thickness of absorber. This is the reason for the finite slope of the final part of the depth-fluence curve. The energy straggling distribution is represented by a Vavilov distribution, which resembles a Gaussian at high energies (corresponding to very small energy losses) and with a tail associated with larger energy losses at low energies [48]. In practice, energy and range straggling for clinical proton beams can be assumed to have nearly Gaussian distributions. The fluctuation in the path length of clinical proton beams in water is of the order of $1-1.3\%$ (1σ) of the range [48]. The average loss of energy by collision per unit distance along the path of a proton (dE/ds) is represented by the collision stopping power:

$$(\frac{dE}{ds})_{col} = 4\pi Z_{eff}^2 e^4 \frac{N_A Z}{A} \frac{1}{m_e v^2} \{ln(\frac{2mv^2}{I(1-(\beta)^2)}) - \beta^2 - \sum(\frac{C_i}{Z})\} \tag{1.2}$$

Where the quantities not thus far defined are: $N_A Z/A$ the number of electrons per gram, β the ratio of the velocity of the particle to the velocity of light, and Σ (C_i/Z) includes density and shell correction terms.

[2]Linear-Energy Transfer
[3]Radio-Biological Effectiveness
[4]Cobalt Gray Equivalent

1.2.3 Elastic interactions with the nucleus

Elastic interactions with the nucleus cause a deviation of the incident proton, with a negligible change in energy; this process is often called Rutherford scattering. The total cross section for this process decreases rapidly with the energy of the particle and the differential cross section decreases with increasing deflection angle [48]. Thus only very few of the protons undergo single, large deflections. Most collisions involve a distant interaction of the particle with a nucleus; the nuclear charge is partially screened by the atomic electrons, and the incident particle experiences only a small deflection. The multiplicity of small-angle deviations along the proton path is known as multiple Coulomb scattering. Moliére, Highland and others have evaluated this scattering [41, 49]. This subject has been reviewed by Gottschalk et al. who also considered scattering in thick absorbers [42]. The angular distribution of particles after traversing a thin foil can be represented to first order by a Gaussian, where the mean angle of multiple scattering is given by:

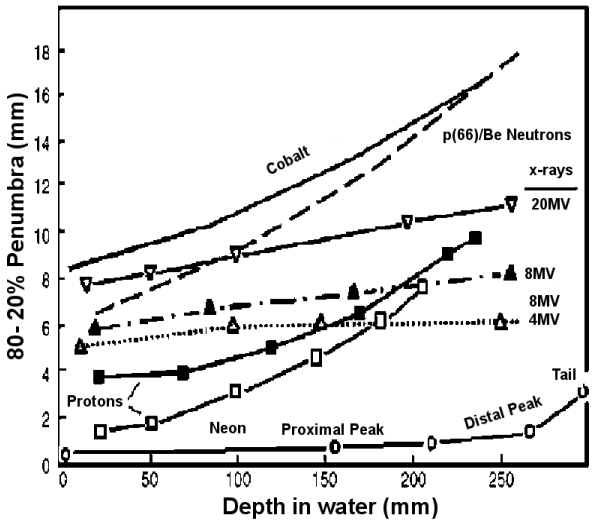

Figure 1.4: Lateral penumbra as a function of depth in water for beams of ^{60}Co γ-rays, neutrons, 4, 8 and 20 MV x-rays, protons and neon ions. Proton and photon penumbras are rather similar at large depth. Clinical light ion beams have intermediate penumbras between those presented for proton and neon beams [50].

$$\bar{\theta_0} = 14.1\frac{Z}{pv}\{\sqrt{\frac{L}{L_R}}(1+\frac{1}{9}log(\frac{L}{L_R}))\} \tag{1.3}$$

Where "Z" , "p" and "v" are the charge number ($charge/e$, which for protons is unity), momentum and velocity of the incident proton, respectively; L is the thickness of the scatterer; L_R is the radiation length characteristic of the scattering material:

$$L_R \propto \frac{A}{NZ(Z+1)}log(188Z^{-1/3}) \tag{1.4}$$

Where N is Avogadro's number, "Z" is the atomic number and "A" the atomic weight of the target material. The scattering power is the mean square scattering angle per unit thickness of an absorber traversed by the charged particles. It is analogous to the concept of stopping power.

In Figure 1.4, the dependence of multiple scattering on an inverse power of the proton (kinetic) energy explains the broadening of a proton (pencil) beam near the end of the range has shown.

1.2.4 Depth-dose curve: range and modulation

The main reason to use heavy charged particles in therapy instead of photons is the inverse dose profile i.e., the increase of energy deposition with penetration depth up to a sharp maximum at the end of the particle range. Bragg peak of a mono-energetic beam must be adapted for clinical use. The maximum depth of the target volume determines the range necessary, and consequently the energy of the beam. This range can be changed either by using an absorber, or by a change of the energy produced in the case of a variable energy accelerator. The raw peak is too narrow for clinical applications. One solution is to superimpose, during irradiation, a certain number of peaks placed at various depths with a modulator to ensure a homogeneous coverage of the target volume [51]. With this approach, the dose at the surface will be increased relative to that of the resulting spread-out Bragg peak. This is one of the principal limitations of the use of a single beam of protons in therapy; the skin dose could be higher than that caused by a high-energy photon beam.

The modulation is produced by interposing in the beam a wheel with sectors of variable thickness. The angular opening of each sector is calculated to obtain a plateau over the desired range of depths. In Figure 1.5, Figure 1.6, and Figure 1.7, modifications of proton depth-dose curves have been shown. An almost homogeneous dose in this SOBP can be obtained independently of the original quality of the beam. However, the surface dose and especially the distal slope of the depth-dose curve are dependent on the energy dispersion of the original beam.

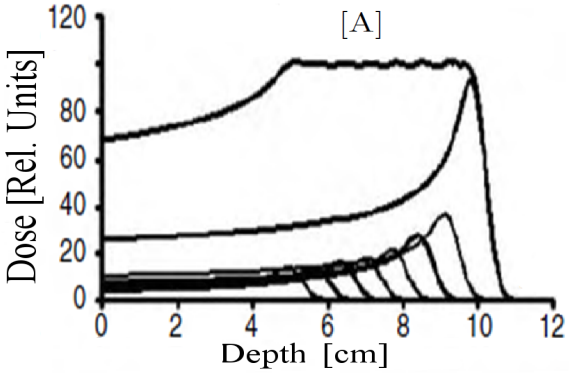

Figure 1.5: Modifications of proton depth-dose curves: [A] modulated or spread out Bragg peak (SOBP) as a result of a weighted sum of single energy peaks of different energies using a range modulator wheel, ridge filters or dynamic techniques [52].

Fast heavy ions were first studied in outer space but the development of accelerator technology has made it possible to obtain the correct energies in the laboratory. In August of 1971, Berkeley Bevatron produced penetrating deflected beams of nitrogen nuclei. Conventional dosimetry measurements cannot give an explanation for the depth-dose characteristic of heavy charged particles because they are not able to provide any information on nuclear fragmentation of the high-energy heavy ions, predominantly in interaction with tissues.

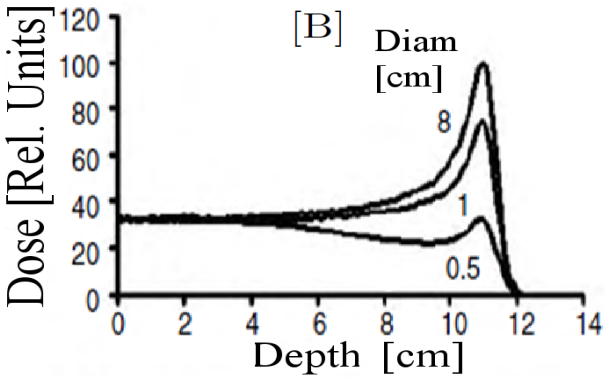

Figure 1.6: Modifications of proton depth-dose curves: [B] Single-energy depth doses for small beam sizes showing the effect of the lack of lateral proton equilibrium [52].

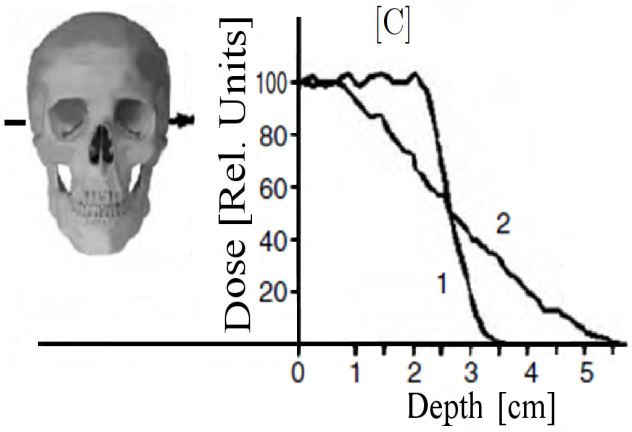

Figure 1.7: Modifications of proton depth-dose curves: [C] Effect of inhomogeneities on the distal fall-off of a SOBP [53]: (1) after traversing a homogeneous phantom; (2) after the complex inhomogeneities in the base of the skull.

Nuclear fragmentation complicates treatment planning for radiotherapy. Measurements at particle accelerators can be used to evaluate fragmentation effects with well-defined beams and high statistics. The data required are of two general types: cross sections and fluencies. Cross-sections are probability measurements that determine whether an ion with a given charge, mass and energy incident on a given target nucleus will produce a fragment with a given set of properties (charge, mass, energy, angle). Fluencies are numbers of fragments produced at depth in shielding. The measurements involved in the two cases are similar, the principal difference being the target thickness. A cross section is the probability for a particular interaction to take place, and therefore must be measured with as thin a target as practical, in order to minimize the likelihood of secondary or higher order interactions affecting the final state of the measured fragment. Cross sections as a function of fragment energy are particularly critical for heavy ion transport model development [54]. A fragment fluence measurement can be made, in principle, behind any target thickness, and is designed to measure the cumulative effects of all the nuclear and electromagnetic interactions, which can affect the final state radiation field observed in the laboratory. Cross sections more directly reflect the dynamics of high-energy nucleus-nucleus interactions, and are fundamental information, which must be incorporated into transport models. Fluencies measurements are used to test how well a model accounts for the many different interactions, which can occur in thick targets. In order to correctly account for the dose contribution of all intervening particles, the fragmentation measurements should be performed [55].

1.2.5 Nuclear fragmentation mechanism

A very important feature of particle beams is their nuclear fragmentation. When heavy ions pass through a thick absorber like the human body even small cross sections for nuclear reactions produce a significant amount of lighter reaction products. In radiotherapy, the change in biological efficiency between the primary ions like carbon and the lighter secondary's has to be taken into account in treatment planning, as well as their longer range. However, radioactive positron-emitting isotopes are very useful to track the beam path inside the patient.

According to a mechanism that is called grazing contact, there is an intermediate range of impact parameters for which the projectile nucleus comes into tangential contact with the target nucleus. During the short period of this contact ($\sim 10^{-23}$ s), a nuclear bond may be formed between the nuclei, but the forward momentum is sufficient to break this nuclear bond. This reaction may result in single-nucleon as well as multi-nucleon transfer from one nucleus to the other [56, 57]. As a result of grazing contact a variety of fragmented products are created from the same type of incident nucleus. This phenomenon is called auto-activation and the fragments of the auto-activated particle are radioactive in nature [58].

There are various ways to study the problem of fragmentation. The differences in the various methods are due to different detection systems. For example, semiconductor detectors can identify fragments by observation of the energy-deposition characteristics of the main beam as well as those of the fragments. The detectors then combine this information with beam acceleration characteristics and particle-physics data. Such techniques have been used by [59] with a rather elaborate arrangement of semiconductors in series and by [60] in a somewhat simplified manner. The radioactive fragments have been detected and identified by half-life determinations and the slopes of their decay curves. The coulomb barrier is of little importance for the entire incident nuclei that have been produced between 240 and 500 MeV/n and the momentum of the fragments is predominantly in the forward direction.

At low energies, however, deviations from this simple phenomenon have been observed. For example,

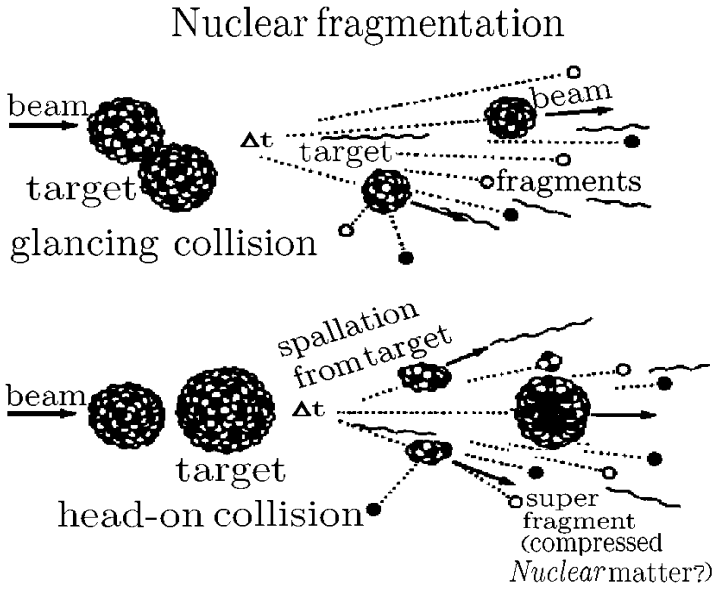

Figure 1.8: Schematic representation of the collision of a fast-moving ${}^{16}_{8}O$ particle with a resting ${}^{16}_{8}O$ nucleus in the target. In a glancing collision (top), radioactivity can be detected from two separate regions: (a) at the site of the collision producing target activity and (b) at the region where the parent beam stops, giving rise to auto-radioactivity. For a head-on collision (bottom), some of the possible products are indicated.

at 10 MeV/n, the fragments of ${}^{16}O$ were distributed between 0 degree and 40 degree with respect to the initial direction of the projectile [56]. Obviously, at these energies Coulomb potential has an important influence on the grazing phenomenon. Figure 1.8 is a diagram of the phenomenon of auto-activation for an individual oxygen particle colliding with resting nuclei in the absorber. If these particles are obtained by stripping a neutron, positron-emitting ions result. Because the energetic radioactive particles have large atomic numbers, they also exhibit precise range-energy relationships.

1.3 Radio-biological aspects of HT in specialized area

The problem of radiation therapy is to effectively kill tumor cells while protecting the normal tissue as much as possible. First, this is a problem of dose delivery precision and second, a biological problem to optimize the biological efficiency of the radiation to be used [61]. Experimentally it is found that densely ionizing radiation like α-particles or heavier ions generate a greater biological effect than the same dose of X rays [62].

DNA is the main target for cell inactivation by ionizing radiation. Therefore, all those dependencies of RBE on the various parameters become at least qualitatively evident from the mechanisms of DNA damage: at low X-ray doses, mainly isolated damage such as SSB[2], etc. is produced. The cell has a very efficient repair system for this type of damage that occurs very frequently and is not only caused by ionizing radiation. Even simultaneous damage at both DNA strands, i.e., DSB, can be repaired by the cell rather quickly with a

[2]Single Strand Breaks

reduced but still high fidelity. However, if the local damage is enhanced by higher local doses more complex DNA damage clustered damage is produced which is less repairable. This is visible in the steep decay in the X-ray survival rates at higher doses.

For light ions like protons, only at the very end of the track i.e., at the last few micrometers, is a clustering of DNA damage realized. This does not seem to be of major importance in therapy. For protons, a small increase of RBE of 10% is used throughout clinical therapy. Very heavy ions like Argon or heavier are extremely efficient in killing cells but unfortunately the efficient region also extends into the normal tissue in front of the tumor, causing heavy late damage. For ions between protons and Argon, in the region of carbon, the RBE dependence is very favorable for therapy. At high energies, the local ionization is low. Therefore, individual DNA lesions are produced with a large repair potential and the damage produced in the normal tissue in front of the target is as repairable as it is for X-rays. This yields an RBE of 1.0 at the end of the carbon ions range, in the last centimeters, the local ionization density reaches a level where a majority of irrepairable DNA damage is produced in a single particle track yielding high RBE values and efficient tumor inactivation.

The extensive range of literature hints at the role of applying proton therapy for the treatment of cancers in different sites and especially in eyes. Its clinical results and trial protocols for the treatment of skull-base, cervical-spine chordoma and low-grade chondrosarcoma, skull-base meningioma, pituitary tumors, paranasal sinus carcinoma, glioblastoma multiform, artero-venous malformations, uveal melanoma, macular degeneration, retinoblastoma, thoracic spinesacrum tumors, prostate carcinoma and other lesions, have been reported in [63, 64, 65, 66, 67, 68].

Our interested site is eye and related cancers of eye such as uveal melanomas. The promising results have been achieved and mentioned in [1, 3, 4, 5, 6, 7, 8, 69]. Moreover, dosimetric studies were done and many clinical trials have been initiated to treat age-related macular degeneration [70].

It is believed that by utilizing heavy charged particles in radiotherapy, two main advantages will be achieved: firstly, particle beams reveal a superior dose depth distribution and have a smaller lateral scattering than any other conventional radio-therapeutic beam like photons or electrons or even neutrons. It is a characteristic feature of all ion beams that the energy deposition by heavy charged particles increases with increasing penetration depths and is maximal shortly before the particles are stopped. Secondly, heavy ions exhibit an elevated biological efficiency in the region of increased energy deposition, which diminishes differences in the radio response between well-oxygenated and hypoxic cells as well as differences between fast and slowly proliferating cells. In addition, with high values for relative biological efficiencies, the repair capacity of the cells is selectively reduced. Both effects, the high-energy deposition and the elevated RBE values at the end of the particle track are due to the physical interaction mechanism of heavy ions with the target material, i. e., the human tissue [28].

It is well known that anoxic cells are about three times more resistant to low-LET radiation than normally oxygenated cells. Evidence has also been accumulating that many tumors have anoxic cells, particularly tumors with necrotic portions. Since low-LET radiation allows preferential survival to anoxic tumor cells, the rationale for high LET therapy of any kind includes the requirement that the oxygen effect should be reduced as far as possible. In fact, one of the main properties that differentiates heavy ions from protons and Helium ions is the greater reduction of the oxygen effect by heavy ions. The study of the oxygen effect has become complex. High-LET particles generally lower OER[1] but the actual value of OER also depends on the particle velocity.

[1] Oxygen Enhancement Ratio

Generally, at the same LET, the OER is assumed to be higher for a higher speed particle. In addition, OER seems to be related to physiological state of cells and to their ability to repair radiation lesions. Finally, different strains of cells exhibit different OER ratios [58, 71].

Chapter 2

Rationale for applying PET in HT

2.1 The role of PET as a feasible technique for dose quantification

The high physical and radio-biological selectivity of ions for tumor therapy demands technological solutions for reliable monitoring of the dose delivery in situ [28]. Since ions, unlike photons, are completely stopped within the target volume, a technology like electronic portal imaging for controlling the lateral field position is not feasible [72]. Moreover, imaging in the third spatial dimension is required, since in ion therapy the formation of the Bragg maximum at the correct depth is crucial.

Shifting the spread of the Bragg peak by a few millimeters may result in severe dose reduction within the target volume or overdosing in organs at risk. The treatment planning of ion therapy requires accurate values of the particle range in tissue which are obtained from the Hounsfield units of X-ray computed tomograms (CT) leading to uncertainties of $1 - 3\%$ in range calculations [73, 74, 75, 76]. Furthermore, during the several weeks of fractionated treatment, unpredictable range deviations may occur due to minor inaccuracies in patient positioning or anatomical changes leading to local density modifications with respect to the CT planning. The method should be applicable simultaneously to the therapeutic irradiation and it should not prolong the treatment in a significant way. Consequently, an imaging technology that is based on a highly penetrable signal, i.e., X or γ rays, is required and such a signal carrying the desired information has to be separated from the much more intensive primary and secondary radiation representing the background.

At present, the two feasible techniques meeting these requirements: one is prompt gamma (PG) and the other is PET. PET which is discussed here is based on the time correlated detection of the annihilation photon pairs emitted collinearly with a well defined energy of 511 keV and a mean time delay distribution (determined by the half-life of the particular isotope) with respect to the production time. Since the positron emitters are formed during the irradiation, with the assistance of "In-beam" PET data, local dose quantification would be achieved. Several attempts to utilize PET for treatment control have been undertaken by researchers since the year of 1978 [77, 78, 79, 80, 81, 82].

Prompt gamma-rays (PG) is also currently under research to be used for dose monitoring. Nuclear fragmentation reactions occur along the proton track resulting in the prompt emission of large numbers of neutrons and gamma rays. These gamma rays arise from the statistical decay of nuclei exited at energies below the nuclear binding energy ($\approx$ 8 MeV) [83]. PG rays are a likely candidate for dose monitoring because their number is much larger than the number of emissions resulting from PET isotope decay [84].

Furthermore the absence of washout effects and the close correlation between the proton range and the PG ray production position are important additional advantages [85, 86]. This correlation is the result of the fact that nuclear reactions occur up to the last few mm of the track where the proton energy falls below the Coulomb barrier threshold [87].

The PG method showed higher gamma production rate than the PET method before, and higher production after including the washout and time corrections. This rate was directly proportional to the tissue density. For passive fields, the correlation between dose and PG / PET is strongly dependent on the location of the line profile within the field. This dependence can be related to the tissue heterogeneity and the position of the distal falloff within the patient. For pencil beams, the distances between both PG / PET and dose falloffs are consistent and therefore well correlated. This is mainly due to the smaller beam size and better-defined distal falloffs. The PG imaging is found more appropriate than PET for pencil beam scanning due to in-situ capabilities and reduced limitations and uncertainties. However, current detector technology does not allow full utilization of this method, while PET range verification has already been studied clinically [88].

2.2 PET as a dedicated method for verification of correct dose delivery in HT

The production of β^+ emitting radionuclides by accelerators is a process known by nuclear medicine physicians who exploit it to produce a multitude of PET tracers. The same type of process, i.e., the production of β^+ emitting radionuclides, also occurs in vivo when biological tissues are hit by high-energy radiation, including heavy ions and protons. In fact, this is the case of some types of radiation therapy. In particular, the nuclear interactions of heavy ions and protons with biological tissues during hadron-therapy lead to the production of many radionuclides, including ^{11}C, ^{13}N and ^{15}O. For almost 30 years, this principle has stimulated many researchers to develop "In-beam" PET scanners with the aim of monitoring the accuracy of the targeting and dose delivery, i.e., PET systems capable of detecting the photons derived from the β^+ decay of radionuclides formed in the target organs by the incident beams used for hadron-therapy [77, 79, 80, 89].

It must be remarked that the use of "In-beam" PET is preferable to that of "Off-beam" PET, as most of the signal derives from the decay of ^{15}O and ^{11}C, i.e., two rapidly decaying radionuclides. This approach, however, presents numerous methodological problems, including the low signal to noise ratio.

Current limitations arise from the fact that "In-beam" PET data are highly corrupted by random coincidences that arise from prompt γ-rays following nuclear reactions of the projectiles with the atomic nuclei of the tissue [90].

The applicability and usefulness of "Off-beam" PET monitoring is limited to the detection of the long-lived isotopes. Furthermore, the moving of the patient from the treatment site to the PET scanner after irradiation may introduce additional position uncertainties.

The biological decay of the produced positron emitters due to washout processes is an important factor, which is taken into account by means of space (i.e., tissue) and time-dependent weighting factors. This physical and biological washout phenomenon and decay half-lives for PET activity for the most abundant isotopes such as: ^{15}O and ^{11}C are taken into account in the data analysis. The biological washout process effects introduce discrepancies between the measured and expected values at positions where the proton beam

stops in soft tissue. These effects, including motion cause spatial deviations between measured and expected activity distributions in tumor sites. Therefore, the activity distributions are found to cause limitations on spatial accuracy values which depending on the physical, biological parameters of the irradiated tissue and specific tumor locations [13, 84]. "In-beam" PET data, could be highly corrupted by random coincidences arising from prompt γ-rays following nuclear reactions as the projectiles penetrating the tissue [91]. They cannot be suppressed with the random correction techniques used in conventional PET. Furthermore, the spatial distributions of the delivered dose and of the induced β^+ activity are not congruent, and for the monitoring of therapy, dedicated procedures have been developed to verify the correct delivery of the treatment plan by means of "In-beam" PET [92, 90].

2.3 The evolution procedure of applying of PET for dose monitoring in HT

Exploitation of the "In-beam" PET principle has led to the construction of the first dedicated PET scanner for in situ and in vivo treatment plan verification and beam monitoring as well as dose control during heavy-ion tumor therapy at the GSI[1], Germany [93]. The GSI researchers assembled a dual-head positron camera by using commercial detector components to measure the β^+ activity, induced by the irradiation, simultaneously with the dose application.

Crespo, Shakirin and Enghardt from the Forschungszentrum Rossendorf[2], and the Technische Universit*ä*t at Dresden[3] reported that the positive clinical impact of the use of such an approach triggered the construction of a hospital-based hadron-therapy facility with "In-beam" PET expected to monitor more delicate radio-therapeutic situations [94]. The analysis of β^+ activity distributions simulated from real treatment situations and detected with several detector arrangements allowed them to conclude that a dual-head tomograph with narrow gaps yields PET images with sufficient quality for monitoring head and neck treatments. For monitoring larger irradiation fields, e.g. treatments in the pelvis region, a closed-ring tomograph was seen to be highly desirable. Finally, a study of the space availability for patient and bed, tomograph and beam portal proved the implementation of a closed-ring detector arrangement for "In-beam" PET to be feasible.

The feasibility and clinical value of "In-beam" PET has been demonstrated for ^{12}C ion therapy using a dedicated, double-head PET scanner completely integrated into the treatment room of the experimental therapy unit at GSI, Darmstadt [11, 12, 15, 95, 96].

Muller and Enghardt from the Institut fur Kern-und Hadronenphysik, Forschungszentrum Rossendorf, and the OncoRay, Dresden, Germany have proposed that "In-beam" PET also may be worthwhile for radiotherapy with high-energy bremsstrahlung [97]. In fact, target volume activation due to (γ, n) reactions at energies above 20 MeV yields moderate β^+ activity levels, which can be employed for imaging.

Motivated by the clinical experience of "In-beam" PET tomograph at GSI [98], usage of commercial full-ring PET or PET/CT as the post-irradiation ("Off-line") scanners have been reported for three centers (two centers in Japan and one center in USA) [11, 99].

In Japan, two new experimental planar positron cameras suited for "In-beam" installation have been realized at HIMAC in Chiba [100] and at Kashiwa [101]. In USA, at MGH[1] in Boston , "Off-line" PET/CT of ^1H therapy is used. The first treatment sessions of the pilot therapy project (for patients who are mainly suffering from tumors in the head and neck region) demonstrated the value of PET monitoring for in vivo validation of the calibration curve between the diagnostic planning CT data and the ion range. In this center, the applicability of commercial full-ring, LSO (Lutetium Oxyorthosilicate)-based PET/CT scanners shortly after proton irradiation is under clinical investigation.

[1]Gesellschaft fur Schwerionenforschung
[2]Institute of Nuclear and Hadron Physics
[3]Radiation Research in Oncology-Oncoray
[1]Massachusetts General Hospital

In comparison to previous "Off-line" approaches using PET imaging alone, PET/CT combined devices provide the additional CT information for accurate co-registration between the planning and imaging positions. To further improve correlation, the treatment immobilization device is carried along and used for fixation of the patient at the remote PET/CT scanner. Duration of the continuous proton beam application as well as time delay between irradiation and imaging is manually recorded. The patient and field-specific expected pattern of activation is directly calculated on the planning CT using the Monte Carlo approach. The same computational engine is used to recalculate the dose delivery for comparison with the dose prescription obtained from the treatment planning system [102]. The activity calculation also takes into account the biological decay of the signal due to blood flow [11]. Measured and calculated PET images superimposed on to the co-registered imaging and planning CT are finally visually inspected. Activity profiles can be quantitatively compared and analyzed, especially with respect to the feasibility of in vivo range validation from the position of measured and calculated distal activation fall-offs.

An increasing interest has been devoted to PET imaging for quality assurance, not only for carbon ions but also for protons [16, 103, 104], ^{3}He [105], ^{16}O [106] and even photons [107]. In Pisa, a PET prototype (DoPET) is under the development. This PET system is used to monitor β^{+} activity distributions induced by the irradiation of hadron ion of Catania center in PMMT[1] phantoms as target volumes. Doing measurements immediately thus after irradiation with our "Off-beam" PET the number of positron emitters are not decreased much, resulting in a good statistics. Moreover, as room of irradiation is the same as the room for measurements, applying DoPET as "On-line" PET is feasible. Thus, monitoring of more delicate radio-therapeutic situations are expected. The first experimental results for this small system were obtained at the INFN Laboratori Nazionali del Sud (LNS) by using 62 MeV protons stopped in PMMA phantoms [108, 109]. [1]

[1] Polymethyl-Methacrylate

Chapter 3

Basic concepts of PET

3.1 The first prototype of our PET

Our PET scanner prototype consists of two planar detector heads, offering an active area of about $45mm \times 45mm$. One head is made up of 21×21 LYSO[1] square crystals ($2.0mm \times 2.0mm \times 18mm$ pixel dimension, with a 2.15 mm pitch) coupled to one squared multi-anode PMT (Hamamatsu H8500C), offering an active area of $49.3mm \times 49.3mm$ [109]. The movable detector heads have been placed symmetrically with respect to the measured activity region, diametrically opposed and 14 cm apart [108]. The Flood field images that have been achieved have an average peak-to-valley ratio of 7.2, an average crystal spatial resolution of about 0.7 mm and an energy resolution lower than 24% at 511 keV [109]. The total detection efficiency at the center of the positron camera was approximately 2.3% in the energy window [250, 850] keV [109]. In order to estimate the background rate expected with a LYSO / PMT detector an energy window of [350, 850] keV was considered in the first version of our PET system. The activity distributions were reconstructed by a 3D MLEM algorithm that uses a probability matrix based on a multi-ray approach and allows corrections for random coincidences as well as for non-uniform detection efficiency [110].

3.2 Data collection in PET system

Prior to doing detailed description of our modular system, some explanation about the concepts of PET scanners is essential. A simple coincidence detection system is illustrated in Figure 3.1, which consists of a pair of radiation detectors with associated electronics (amplifiers, pulse height analyzers, high voltage) and a coincidence circuit. If an annihilation occurs somewhere between two detectors, and the direction of the two 511 keV photons is such that each will have a chance to interact with one of the two detectors, it is very likely that a coincidence event will be recorded. Because all annihilation photons are emitted approximately 180 degrees apart, a recorded coincidence indicates that an annihilation occurred somewhere along the line (or more accurately, the volume) connecting the two detectors. This line or volume from which the detector pair can detect coincidences usually is referred to as a line of response or LOR. To reconstruct a complete cross-sectional image of the object, data from a large number of these LORs are collected at different angles and radial offsets that cover the field of view of the system [111].

The two detectors and associated circuitry should, under ideal circumstances, simultaneously generate the logic pulses necessary to produce a coincidence. However, due to stochastic processes in the emission of light in the scintillation detectors, a random time delay occurs exactly when the detectors respond to the light emitted by the scintillator following the absorption of the annihilation photons in the detectors. This

[1] Lutetium-Yttrium Oxyorthosilicate

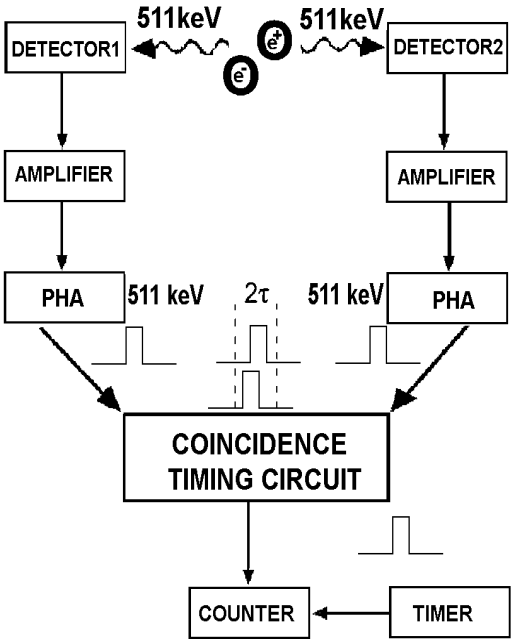

Figure 3.1: Diagram of a basic coincidence circuit of a PET scanner.

uncertainty in response (time resolution) depends on the characteristics of the detector, primarily scintillation decay time constant and light output [111]. Furthermore, small differences are noted in the arrival times of the two photons depending on the difference in the distance of the annihilation site to each detector. To avoid missing coincidence events, the logic pulses must have a certain finite width to ensure that the pulses overlap despite the finite time resolution. Typically, the width of the logic pulses, τ, should be at least as wide as the timing resolution of a pair of detectors (measured in FWHM). Timing resolution for a BGO-based PET detector is approximately 5 to 6 nanoseconds FWHM, while for LSO it is approximately 2 to 3 nanoseconds FWHM. It is important to keep the pulses as narrow as possible to minimize the detection of events from uncorrelated decays that happen to strike the detectors within the time window determined by the overlap of the two logic pulses [111].

In Figure 3.1, The two scintillation detectors are connected to individual amplifiers (Amp) and pulse height analyzers (PHA). When a photon interacts in either of the detectors, the signals are amplified and analyzed to determine if the energy is above a certain threshold. If the energy criterion is satisfied, a logic pulse is generated by the PHA. These pulses are fed into a coincidence module (Coinc), which determines if there is an overlap of two pulses from the individual channels. An overlap occurs if both pulses occur within a time period of 2τ (e.g., they differ from each other in time by $\leq \tau$), where τ is the width of the pulse. If this is the case, a coincidence has been detected and the coincidence circuit generates a logic pulse that is fed into a counter for registration of the event. In a PET imaging system, the memory location corresponding to the two detectors in which the interaction occurred is incremented by one [111].

3.3 Different types of events in PET

Under ideal circumstances, only true coincidences would be recorded, that is, only events where the two detected annihilation photons originate from the same radioactive decay and have not changed direction or lost any energy before being detected. However, due to limitations of the detectors used in PET and the

possible interaction of the 511 keV photons in the body before they reach the detector, the coincidences measured are contaminated with undesirable events, which includes random, scattered and multiple coincidences. All these events have a degrading effect on the measurement and need to be corrected to produce an image that represents as closely as possible the true radioactivity concentration [111].

Another point to be considered is that the vast majority of photons detected by PET scanners are single events, in which only one of the two annihilation photons is registered. The partner photon may be on a trajectory that does not intersect a detector (most PET scanners provide relatively modest solid angle coverage around the object), or the photon may not deposit sufficient energy in a detector to be registered or may not interact at all. These single events are not accepted by PET scanners, but they are responsible for random and multiple coincidence events. Because they must still be processed by the electronics to see if they form part of a coincidence pair, they are the determining factor in issues related to detector dead time [111].

The reduced random event contribution enabled by the narrow coincidence window is canceled by the increased scatter fraction contribution due to the larger solid angle coverage. However, the low radioactivity of the ^{22}Na source, which has been located in the field of view and has provided an small solid angle does not create a crucial problem. Using LYSO scintillator material in the detector modules results in low dead time, which coupled with high coincidence processor throughput allows the increased solid angle coverage to be converted into a significantly increased noise equivalent count rate [112].

3.3.1 Random coincidences

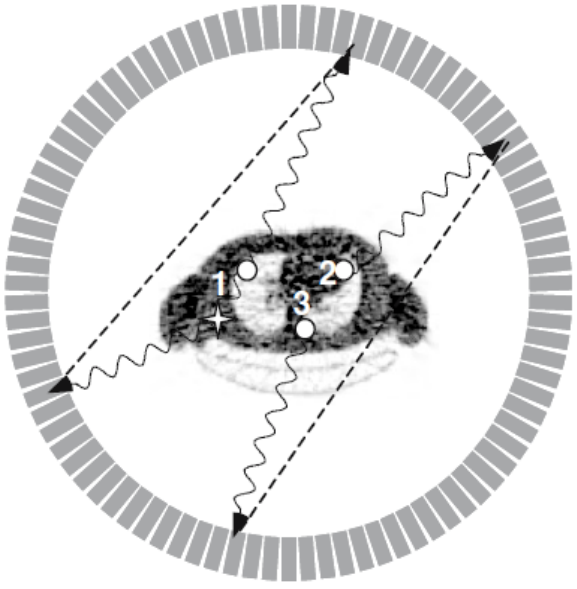

Figure 3.2: In a PET scanner: Event 1 shows a coincident event where one of the $\gamma-rays$ is scattered leading to an incorrectly assigned line-of-response (LOR, dotted) for image reconstruction (scatter coincidence). Events 2 and 3 represent two unrelated events with only one photon being detected (singles events). If they occur within the coincidence timing window, then an incorrect LOR (dotted) gets assigned (random coincidence) [113].

Random events are source of noise in the PET and are caused by the incorrect pairing of photons from different annihilations. When positron annihilation occurs, the two 511 keV photons are emitted simulta-

neously. Therefore, the detectors should ideally respond simultaneously. The finite time resolution of the detectors determines that signals must be accepted if they occur within a certain finite time interval or timing window. Due to the finite width of the timing window, it is possible that two unrelated single annihilation photons can be detected and registered as a valid coincidence. These unrelated events are referred to as random events. As random events are produced by photons emitted from unrelated isotope decays, they do not carry any spatial information about the activity distribution and produce an undesired background in the final images. As it has been shown in Figure 3.2, these coincidences reduce the image contrast. The scatter coincidences are true coincidence events from single annihilation points, but where one or both the photons undergo Compton scatter within the imaging FOV before entering the PET detector.Since scattered coincidences lead to mis-positioned lines-of response, and therefore misrepresent the true activity distribution within the FOV, the image contrast worsens [113].

If the individual photon detection rates (counts per second) in a pair of detectors are given by N_1 and N_2, then it can be shown that the rate of random coincidences, N_R (randoms per second) is given by:

$$N_R = 2\tau N_1 N_2 \tag{3.1}$$

Where τ is the width of the logic pulses produced when a photon is absorbed in the detector. The term 2τ is often referred to as the coincidence timing window. As individual detection rates N_1 and N_2 are directly proportional to the activity in the field of view of the scanner, the rate of random coincidences vary with the square of the administered activity in the field of view. However, the true coincidence events increase linearly with the administered activity. The randoms rate is directly proportional to the coincidence timing window, which is why it is important not to make this any wider than required by the timing uncertainties in true coincidence events [111].

Random events arise from a variety of situations, such as the highly likely attenuation of one photon or when the system fails to detect a photon. As with scatter correction, randoms correction algorithms can alleviate some but not all of the noise contribution of this physical limitation [114]. The noise in the PET depends on the number of events detected. This count-limited modality benefits from the long acquisition times needed to acquire as many true events as possible. Increased injected activity will not only result in a beneficial linear increase in true events, but also in a detrimental linear increase in scatter events and a highly detrimental square increase in random events. PET scanner and acquisition protocols are designed to optimize the trade-offs of true, scatter, and random events [115]. But it is obvious that rapid transients in local tissue concentrations will involve a trade-off between the accuracy of each image acquired and the number of events recorded.

Figure 3.3 shows an implementation whereby each timing signal opens a gate of duration τ; if gates on two channels are open at the same time, a coincidence is recorded. If there is a timing signal on channel i at time T, there will be a coincidence on the relevant LOR[1] if there is a timing signal on channel j at any time between T - τ and T + τ. Therefore, the total time during which a coincidence may be recorded with the event on channel i (a parameter known as the resolving time of the circuit, or the coincidence time window) is 2τ [113].

3.3.2 Scattered coincidences

Scattered coincidences are another type of background event that needs correction. These events are in essence true coincidences, but one or both of the two annihilation photons has undergone a Compton scattering interaction and changed direction before it reached the detector. Using the coincidence detection technique, it is assumed that all detected coincidence events originate from an annihilation which, in turn, originates from a position anywhere on a line connecting the detector pairs. Due to the change in direction

[1] Line-Of Response

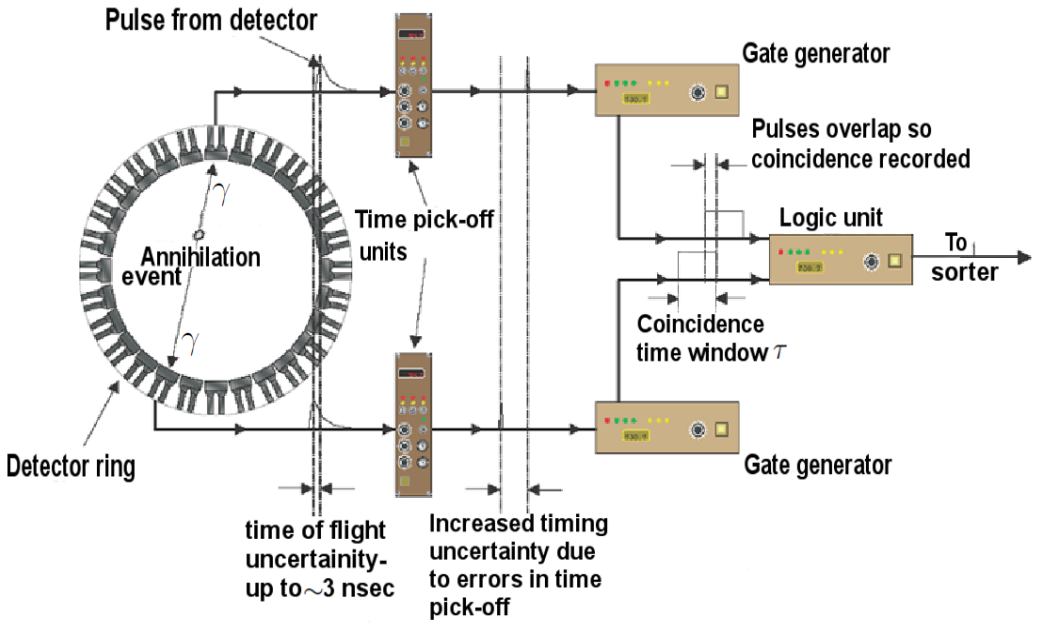

Figure 3.3: A coincidence circuitry. Each detector generates a pulse when a photon deposits energy in it; this pulse passes to a time pick-off unit. Timing signals from the pick-off unit are passed to a gate generator which generates a gate of preselected width. The logic unit generates a signal if there is a voltage on both inputs simultaneously. This signal then passes to the sorting circuitry [113].

of the photon(s) in a scattered event, this is not true and the event is assigned to the incorrect LOR. If not corrected, the scattered events produce a low spatial frequency background that reduces contrast. The distribution of scattered events depends on the distribution of the radioactivity of the source and the shape of the scattering medium (i.e., the patient). The fraction of scattered events that are detected can range from 15% to well over 50% in typical PET studies, depending on the size of the object and the geometry and energy resolution of the PET scanner.

3.3.3 Prompt coincidences

The total number of events detected by the coincidence circuit in a PET scanner are referred to as prompt coincidences. These events consist of true, scattered, and random coincidences where the true coincidences are the only ones that carry spatial information regarding the distribution of the radio-tracer. It is, therefore, necessary to estimate what fraction of the measured prompt coincidences arises from scattered and random coincidences for each of the LORs. The contribution of scattered and random coincidences are then subtracted from the prompt coincidences to yield the net true coincidence rate for each measured LOR. The number of both the scattered and random events are, in general, estimates, and therefore the accuracy of these estimates will affect the accuracy of the net calculated true coincidence rate. Any statistical or systematic noise in these estimates will also propagate into the net true coincidence rate.

3.4 Processing of Coincidences

When a scintillation detector detects a photon, the electrical pulse generated by the PMT or PMT array is used to generate a timing signal. This can be done by passing the pulse through a constant fraction discriminator (CFD), which generates a digital pulse when the signal reaches a constant fraction of the peak

pulse height. This pulse is then used in the coincidence circuitry. Once timing signals have been generated from each pulse, they are passed to a coincidence circuitry for processing. There will usually be some time difference between two timing pulses arising from a coincidence event due to the finite time resolution of the detector and CFD system. In order to deal with this, the timing pulses are passed to a gate generator (Figure 3.3), which creates an electronic pulse of duration Δt. Δt is known as the coincidence resolving time of the system. These fixed-width pulses are then passed to a logic unit, which generates a pulse if there is a signal on both of its inputs at the same time. So if a timing pulse is generated on one channel at time t, a coincidence will be recorded if there is a timing pulse on the other channel between t - Δt and t + Δt. The value of Δt must be carefully chosen. If it is too small compared to the time resolution of the detection system, true coincidences will be missed. If it is too large, more random coincidences will be counted without significant increase in the number of true coincidences.

3.5 Time Resolution

In principle, a system designed for timing measurements transforms the detector signal that corresponds to the desired event into an unambiguous digital signal, separating it from other types of events and from the background noise. The digital signal is compared to a temporal reference in a time-to-digital circuit that generates a time stamp or can be passed to a coincidence circuit that looks for the occurrence of a broader event [116].

3.5.0.1 Timing errors due to Noise

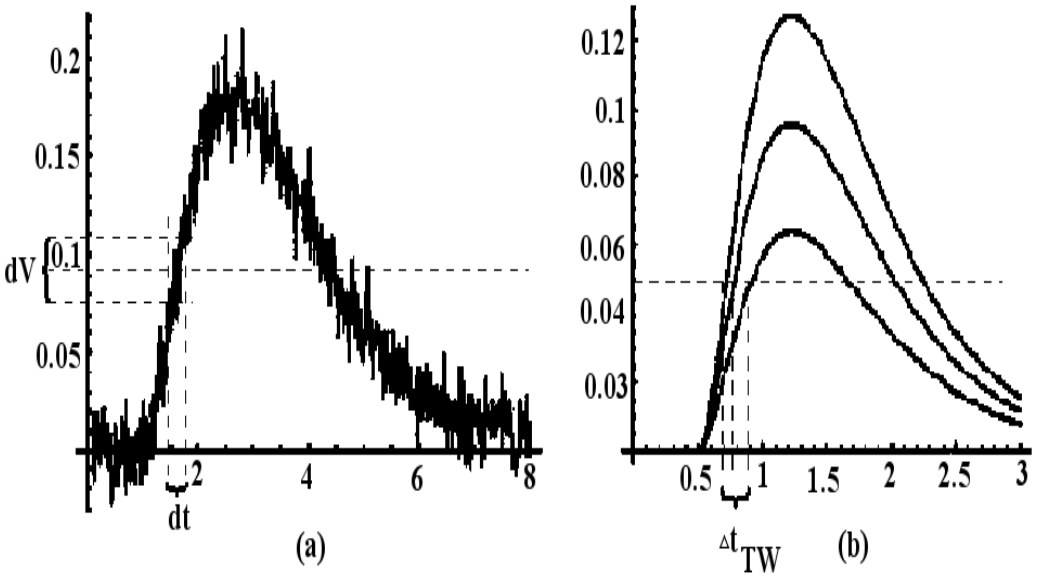

Figure 3.4: Timing errors: (a) jitter; (b) time-walk.

In a simple example, the signal coming directly from the detector, or opportunely amplified and shaped, is continuously compared to a fixed threshold level. When the signal crosses this threshold level, the digital timing signal is issued. Such a circuit is generally known as a leading-edge discriminator. In the presence

of noise, the threshold level should be set significantly higher than the noise level to limit the occurrence of fake signals triggered by noise. Apart from this, the presence of noise has a significant influence on the timing accuracy of the system, which can be understood with the help of Figure 3.4. As the signal level approaches the threshold, the noise fluctuation that modulates the signal may cause it to cross the threshold level sooner or later than in the ideal noiseless case. This uncertainty window increases with the noise level, but shrinks if the signal is faster. The effect is called jitter and is quantitatively given by the ratio between the noise and the slope of the signal [117, 118, 119].

$$\sigma_t = \frac{\sigma_n}{dV/dt} \tag{3.2}$$

This expression implies that a system for time measurement has to be optimized for maximum slope-to-noise ratio, as opposed to the signal-to-noise ratio optimization that is required for an amplitude-measuring system. This fact has important implications on the design criteria for timing systems.

Reducing noise alone does not necessarily provide a better timing resolution. Suppose that one decides to increase the integration time of the preamplifier (i.e., the amount of time the preamplifier integrates the charge coming from the detector in order to retrieve the intensity of the radiation event). This is equivalent to reducing the bandwidth of the preamplifier, averaging out more thermal noise, thus reducing the noise level. On the other hand, the signal at the output of the preamplifier is slower, so the denominator of Eq. 3.2 is smaller, which, in turn, causes a degradation of the timing accuracy [116].

In the other direction, if the front-end bandwidth is increased too much and the shaping time becomes faster than the detector signal, the slope of the signal does not improve significantly, as it is dominated by the charge collection time in the sensor. The noise level then rises because the higher bandwidth of the preamplifier determines an increase of its output noise (the numerator in Eq. 3.2, while the slope stays approximately the same, thereby degrading the jitter figure.

It can be shown that, for an optimum pulse shaping the integration time in the front-end electronics should match the collection time of the detector [119].

Another parameter that could, in principle, be manipulated to improve the timing performance is the threshold level. In fact, one can set the threshold at the exact point where the signal slope is maximum. This choice does not affect in any way the noise level, thus optimizing the time resolution. In practice, however, this is rarely possible, since the amplitude of the signal is generally variable. Furthermore, the threshold level may be imposed by the need to select a specific type of event, which prevents its use for timing optimization [116].

3.6 Spatial resolution

The spatial resolution of the PET is a measure of the ability of the scanner to faithfully reproduce the image of an object, thus clearly depicting the variations in the distribution of radioactivity in a object. It is empirically defined as the minimum distance between two points in an image that can be detected by the scanner [113, 120].

Common methods to measure this in emission tomography are to image a point source (giving a point spread function (PSF)), or, more usually, a line source (LSF[1]) of radioactivity. The resolution is usually expressed as the FWHM[2] of the profile. A Gaussian function is often used as an approximation to this profile. The standard deviation is related to the FWHM by the following relationship:

$$FWHM = \sqrt{8 \log_e 2} \times \sigma \tag{3.3}$$

[1] Line Spread Function

[2] full width at half maximum

where σ is the standard deviation of the fitted Gaussian function. There are many factors that influence the resolution in a PET reconstruction [113]. These include:

1. Non-zero positron range after radionuclide decay,
2. Non-collinearity of the annihilation photons due to residual momentum of the positron,
3. Distance between the detectors,
4. Width of the detectors,
5. Stopping power of the scintillation detector,
6. Incident angle of the photon on the detector,
7. The depth of interaction of the photon in the detector,
8. Number of angular samples, and
9. Reconstruction parameters (matrix size, windowing of the reconstruction filter, etc.).

3.7 Sensitivity

One of the most important factors in designing a PET system is to maximize the system sensitivity, since this will be a major determinant of final image quality. The more coincidence events that can be detected and used to form the image, the better. The number of events collected is dictated by the amount of radioactivity injected, the fraction of the injected activity that reaches the tissues of interest, the imaging time, and the sensitivity of the PET system [111]. The sensitivity of the PET scanner is defined as the number of counts per unit time detected by the scanner for each unit of activity present in a source. The purpose of a sensitivity measurement on a positron tomograph is primarily to facilitate comparisons between different systems, as, in general, the higher the sensitivity the better the signal-to-noise ratio in the reconstructed image (neglecting dead time effects). The sensitivity of positron tomographs has traditionally been measured using a distributed source of a relatively long-lived tracer, such as ^{18}F, in water. The value is quoted in units of counts per second per micro-Curie per milliliter ($cts.sec^{-1}.\ \mu\, Ci^{-1}.ml^{-1}$) in non-SI units,without correction for attenuation or scattered radiation [113, 120].

A method has been developed to make absolute sensitivity measurements in PET [121], and has been adopted in the new updated NEMA testing procedures [122]. It employs the measurement of a known amount of ^{18}F (or ^{99}Tc for SPECT) in a small source holder made from aluminum. The thickness of the aluminum wall of the source holder used is sufficient to stop all of the positrons, causing annihilation radiation to be produced, but which also causes some attenuation. The count rate for this source is found by measuring it for a defined period in the camera.Next, another tube of aluminum of known thickness is added to the holder, causing further attenuation, and this is counted again. This is done for a number of extra tubes of aluminum, all of known thickness, and an attenuation curve is produced. The extrapolated y-intercept from this curve gives the "sensitivity in air" for the camera. The units of this measurement are $ct.sec^{-1}.MBq^{-1}$. This provides an absolute measure of sensitivity. The method can also be used for PET system calibration of reconstructed counts without requiring scatter or attenuation correction [123, 113, 120].

The system sensitivity is a product of several factors, which include the efficiency of the detectors at 511 keV, the solid angle coverage of the detectors, the location of the radioactivity with respect to the detectors, and the timing and energy windows applied to the data [111].

3.8 Detection efficiency

The detection efficiency ε, of an individual detector is given by the product of the detection probability of the incoming photon in the detector volume and the fraction of these events, Φ, that falls within the selected energy window (typically set at 350 - 650 keV) [111]. The energy window helps to reduce the influence of scattered events by only accepting events that deposit energy close to 511 keV (e.g., photo-peak events). The efficiency is:

$$\varepsilon = (1 - \exp^{(-\mu d)}) \times \Phi \tag{3.4}$$

Table 3.1: Properties of LYSO Scintillator Material for γ-Ray Detection at 511 keV

Detector Material	Refractive Index	Linear Attenuation at 511 keV (cm^{-1}) μ	Ratio between Photoelectric and Compton Φ
LYSO	1.82	0.87	0.52

where μ is the attenuation coefficient of the detector material (Table 3.1), and d is the thickness of the detector. A valid event requires that both photons be detected in opposing detectors and be within the appropriate energy range [111]. The coincidence detection efficiency is, therefore, given by the square of Eq. 3.5:

$$\varepsilon^2 = (1 - \exp^{(-\mu d)})^2 \times \Phi^2 \tag{3.5}$$

3.9 Intrinsic and Geometric efficiency

The intrinsic efficiency is the fraction between the number of events recorded and the number of gamma rays incident on the detector surface, it depends on the interaction between the gamma photons and the material of the detector [111].

The geometric efficiency of the system is determined by the overall solid angle (Ω) coverage of the detectors with respect to the source location and the packing fraction [111]. The solid angle subtended by the detectors of a circular system for a point source placed at the center is given by:

$$\Omega = 4\pi \sin[\tan^{-1}(A/D)] \tag{3.6}$$

where D is the diameter of the detector ring. For a PET scanner consisting of a single ring of detector elements, A is just the height of the detector in the axial direction [111]. For scanners consisting of multiple detector rings (e.g., a ring or rings of block detectors) or continuous detectors, A depends on the maximum acceptance angle over which data will be collected. The total efficiency is given by the product of the two components.

In the manufacturing of the detectors in a PET system using discrete detector elements or block detectors, a small gap is always between the detector elements due to the need for reflective material on the detector walls and/or detector encapsulation [111]. This dead space will produce a reduction in the overall efficiency and is referred to as the packing fraction (φ). The packing fraction is the ratio of the detector element area (width of detector element by axial height of detector element) to the total surface area, including the dead space:

$$\varphi = \frac{width \times height}{(width + dead\ space) \times (height + dead\ space)} \tag{3.7}$$

The overall system sensitivity, η, for a point source placed at the center of a ring scanner is the product of the square of the detection efficiency ε and the geometric efficiency $\varphi \times \Omega$. Expressed as a percentage, it is given by:

$$\eta = 100 \times \frac{\varepsilon^2 \varphi \Omega}{4\pi} \tag{3.8}$$

ε is squared as a result of the coincidence detection. Because of this, a small reduction in ε, due to either a reduction in the thickness of the scintillator or a tighter energy window, will produce a significant loss in the overall sensitivity. φ appears as a linear term because of the angular correlation of the two photons; however, this is only an approximation and the true contribution of packing fraction losses is position and geometry dependent [111]. For a distributed source, the expression becomes more complex due to variations in both the geometric and detection efficiencies across the field of view (FOV).

3.10 Dead time in radiation detection systems

In nearly all detector systems, there will be a minimum amount of time that must separate two events in order that they are recorded as two separate pulses. In some cases the limiting time may be set by processes in the detector itself, and in other cases the limit may arise in the associated electronics. This minimum time separation is usually called the dead time of the counting system. Due to the random nature of radioactive decay, there is always some probability that a true event will be lost because it occurs too quickly following a preceding event. These "dead time losses" can become rather severe when high counting rates are encountered, and any accurate counting measurements made under these conditions must include some correction for these losses [124].

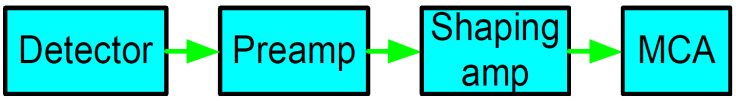

Figure 3.5: Pulse processing systems for radiation detectors.

When radiation is incident on the detector, where charge is created, a voltage pulse is passed to the amplifier where it is shaped and amplified. The pulse is then passed to the multi-channel analyzer (MCA) where its height is digitized. All of these processes take time. While one pulse is being processed, another event cannot be detected. The time this takes is called the dead time. Typical pulse processing systems for radiation detectors are shown in Figure 3.5. The dead time of a system is the summation of all the processing times of the different components, detector, amplifier and MCA. If dead time losses are not accounted for, this can lead to misleading results e.g. source activities will be underestimated [118].

3.10.1 Dead time losses from the statistical point of view

When measuring radiation from radioactive sources, it is assumed that the true events occurring in the detector follow Poisson statistics in which the probability of an event occurring per unit time is a constant. The effect of system dead time is to remove selectively some of the events before they are recorded as counts. Specifically, events occurring after short time intervals following preceding events are preferentially

discarded [118]. If the dead time losses are not small, the deviations from Poisson statistics become more significant. The discarding of events that occur after short time intervals causes the sequence of recorded counts to become somewhat more regular, and the variance expected in repeated measurements is reduced. With either paralyzable or non-paralyzable behavior, there is some chance that more than one true event is lost per dead period. A recorded count therefore can correspond to the occurrence of any number of true events, from one to many. The relative probability that multiple true events are contained in a typical dead period will increase as the true event rate becomes higher. Because true events still obey Poisson statistics, relatively simple analyses can be made to predict the probability [118].

3.10.2 Singles dead time

The main source of dead time in most PET systems is the processing of each event in the detector front-end electronics. Factors which contribute to singles dead-time in a block detector PET scanner include the light integration period, the time necessary to perform the energy discrimination and for the block to return to the quiescent state, and the time to determine and encode which crystal in a block detected the event. It is during the light integration period that mispositioning effects of pulse pile-up can occur. The integration time is typically set at 3 to 4 times the decay time constant [125]. Thus, if the integration time can be reduced, for instance, by using a faster scintillator, the amount of detector dead time can be reduced.

Other contributions to dead time in a PET system can come from the coincidence event processing, real-time sorting of data into sinograms, and data transfer [126]. Correction for dead time typically involves a model of the dead time behavior of the system at different count rate levels and will generally be some combination of paralyzable and non-paralyzable dead time factors by the different processing stages in the system. Input to the overall dead time determination is usually the measured average detector singles rates and coincidence rates [127].

3.10.3 Models for dead time behavior

Two models of dead time behavior of counting systems have come into common usage:

1. Paralyzable response

2. Non-paralyzable response

These models represent idealized behavior, one or the other of which often adequately resembles the response of a real counting system. True systems, being a combination of components, will often be somewhere between the two models [124]. The fundamental assumptions of the models are illustrated in Figure 3.6.

At the center of the figure, a time scale is shown on which six randomly spaced events in the detector are indicated. At the top of the figure is the corresponding dead time behavior of a detector assumed to be non-paralyzable. A fixed time τ is assumed to follow each true event that occurs during the "live period" of the detector. True events that occur during the dead period are lost and assumed to have no effect whatsoever on the behavior of the detector. Figure 3.6 shows that the non-paralyzable detector would record four counts from the six true interactions. In contrast, the behavior of a paralyzable detector is shown in the middle section of Figure 3.6. The same dead time τ is assumed to follow each true interaction that occurs during the live period of the detector. True events that occur during the dead period, however, although still not recorded as counts, are assumed to extend the dead time by another period τ following the lost event. Figure 3.6 shows, only three counts are recorded for the six true events.

The two models predict the same first-order losses and differ only when true event rates are high. They are in some sense two extremes of idealized system behavior, and real counting systems often display a

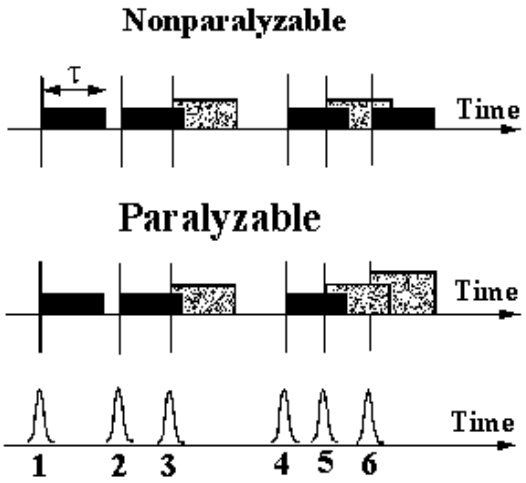

Figure 3.6: Models of dead time behavior: at the top, non-paralyzable and in the middle paralyzable dead time, events that arrive before complete processing of earlier events are rejected (events 3 and 5). In a system with paralyzable dead time, the usual dead time effect is experienced; however, the arrival of a secondary event extends the dead time, causing the secondary event to be rejected. This feature is demonstrated by the rejection of event 6 in addition to events 3 and 5.

behavior that is intermediate between these extremes. The detailed behavior of a specific counting system may depend on the physical processes taking place in the detector itself or on delays introduced by the pulse processing and recording electronics.

In the discussion that follows, the response of a detector system to a steady-state source of radiation is examined, and the following definitions are adopted: $n = true\ count\ rate$, $m = recorded\ count\ rate$ and $\tau = system\ dead\ time$. It is assumed that the counting time is long so that both n and m may be regarded as average rates. In general, obtaining an expression for the true interaction rate n as a function of the measured rate m and the system dead time τ is necessary, so that appropriate corrections can be made to measured data to account for the dead time losses.

3.10.3.1 Non-paralyzable response

In the non-paralyzable case, the fraction of all times that the detector is dead is given simply by the product mτ. Therefore, the rate at which true events are lost is simply nmτ. But, because $n - m$ is another expression for the rate of losses,

$$n - m = nm\tau \tag{3.9}$$

Solving for n, it is obtained:

$$n = \frac{m}{1 - m\tau} \tag{3.10}$$

3.10.3.2 Paralyzable response

In the paralyzable case, dead periods are not always of fixed length, so applying the same argument is not possible. Instead, rate m is identical to the rate of occurrences of time intervals between true events

which exceed τ is mentioned. The distribution of intervals between random events occurring at an average rate n is Eq. 3.11.

$$P_1(t) = n \exp^{-nt} dt \tag{3.11}$$

Where $P_1(t)dt$ is the probability of observing an interval whose length lies within dt about t: The probability of intervals larger than τ can be obtained by integrating this distribution between τ and ∞ Eq. 3.12.

$$P_2(\tau) = \int_{\tau}^{\infty} P_1(t)dt \approx \exp^{-n\tau} \tag{3.12}$$

The rate of occurrence of such intervals is then achieved by simply multiplying the above expression by the true rate n. The paralyzable model leads to a more cumbersome result because explicitly solving is not possible for the true rate n. Instead, Eq. 3.12 must be solved iteratively if n is to be calculated from measurements of m and knowledge of τ.

$$m = n \exp^{-n\tau} \tag{3.13}$$

When the rates are low the two models give virtually the same result, but the behavior at high rates is markedly different.

A non-paralyzable system approaches an asymptotic value for the observed rate of $1/\tau$, which represents the situation in which the counter barely has time to finish one dead period before starting another.

For paralyzable behavior, the observed rate is seen to go through a maximum. Very high true interaction rates result in a multiple extension of the dead period following an initial recorded count, and very few true events can be recorded.

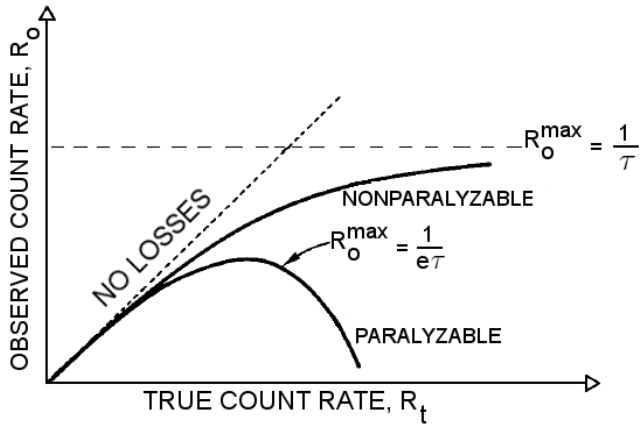

Figure 3.7: Observed rates (y axis) as a function of the true rate (x axis) for the two dead time models.

One must always be careful when using a counting system that may be paralyzable to ensure that low observed rates actually correspond to low interaction rates rather than very high rates on the opposite side of the maximum.

$$m = \frac{n}{1 + n\tau} \cong n(1 - n\tau) \qquad Non - paralyzable \tag{3.14}$$

$$m = n \exp^{-n\tau} \cong n(1 - n\tau) \qquad Paralyzable \tag{3.15}$$

The ambiguity can be resolved only by changing the true rate in a known direction while observing whether the observed rate increases or decreases. For low rates ($n \ll \frac{1}{\tau}$) the following approximations can be written as in Eq. 3.14 and Eq. 3.15. Thus, the two models lead to identical results in the limit of small dead time losses. If possible, one should avoid measurement conditions under which dead time losses are high due to the errors that inevitably occur in making corrections for the losses. The value of τ may be uncertain or subject to variation, and the system behavior may not follow exactly either of the models described above.

3.10.4 Dead time correction

Dead time is considered as one of the main figures of merit of our PET acquisition system. Our PET study is applied in hadron therapy dosimetry and for the PET, which is used for clinical study, the radiation dose and scanning interval have to be minimized, thus making of superior importance to minimize events losses.

It is necessary to measure the counting rate wide range of scanning conditions. To characterize dead time of DoPET system, the scanner response should be fitted by either a paralyzable or nonparalyzable dead time model. Mathematically, these models are described by Eq. 3.14 and Eq. 3.15.

Two common methods are being explained in the following. These methods are based on a phenomenological model which does not depend strongly on the hardware configuration of the tomograph and are thus adaptable to our case. However, by considering that an accurate estimation is needed to characterize the performance our modular PET system, a long data acquisition was done and then the second method was applied to measure dead-time of PET scanner.

3.10.4.1 Dead time measurement: two - source method

The method is based on observing the counting rate from two sources individually and in combination. Due to the nonlinearity of counting losses, the observed rate owing to the combined sources will be less than the sum of the rates of the two sources counted individually, and the dead time can be calculated from the discrepancy.

It is assumed that m_l, m_2, and m_{l2} represent the corresponding observed rates and n_l, n_2, and n_{12}, as the true counting rates (sample plus background) with source 1, source 2, and the combined sources, respectively. Also, it is deemed that n_b and m_b be the true and measured background rates with both sources removed. Then

$$n_{12} - n_b = (n_1 - n_b) + (n_2 - n_b) \tag{3.16}$$

$$n_{12} + n_b = n_1 + n_2 \tag{3.17}$$

By assuming the non-paralyzable model and substituting, it is obtained:

$$\frac{m_{12}}{1 - m_{12}\tau} + \frac{m_b}{1 - m_b\tau} = \frac{m_1}{1 - m_1\tau} + \frac{m_2}{1 - m_2\tau} \tag{3.18}$$

Solving this equation explicitly for τ gives the following result:

$$\tau = \frac{X(1 - \sqrt{1 - Z})}{Y} \tag{3.19}$$

Where

$$X \equiv m_1 m_2 - m_b m_{12} \tag{3.20}$$

$$Y \equiv m_1 m_2(m_{12} + m_b) - m_b m_{12}(m_1 + m_2) \tag{3.21}$$

$$Z \equiv \frac{Y(m_1 + m_2 - m_{12} - m_b)}{X^2} \tag{3.22}$$

A number of approximations to this general solution are often considered. In the case of zero background ($m_b = 0$)

$$\tau = \frac{m_1 m_2 - [m_1 m_2(m_{12} - m_1)(m_{12} - m_2)]}{m_1 m_2 m_{12}} \tag{3.23}$$

Other simplifications of Eq. 3.23 have appeared that are based on various mathematical approximations. However, the use of any type of approximation should be discouraged because significant errors can be introduced under typical experimental conditions [128].

3.10.4.2 Dead time measurement: The applied method for our data

The second method, which is applied to measure the dead time of our system follows the below procedure. For a non-paralyzable dead time the recorded count rate, m, is related to the true count rate, n, and the dead time, t_d, by:

$$m = \frac{n}{1 + nt_d} \tag{3.24}$$

and for a paralyzable dead time by:

$$m = n \exp^{-nt_d} \tag{3.25}$$

The dead time was estimated via the decaying source method using a ^{18}F-FDG source centered in the FoV.

If the system is non-paralyzable then substituting $n = n_0 exp^{-\lambda t}$, where λ is the decay constant of the radioisotope used, equation Eq. 3.21 becomes:

$$m \exp^{\lambda t} = -n_0 t_d m + n_0 \tag{3.26}$$

Plotting $mexp^{\lambda t}$ versus m should result into a straight line. The dead time can be obtained from the slope and the intersection point with the y-axis.

If the system is paralyzable then substituting $n = n_0 exp^{-\lambda t}$ results in:

$$\ln m + \lambda t = -t_d n_0 \exp^{-\lambda t} + \ln n_0 \tag{3.27}$$

Plotting $lnm + \lambda t$ versus $exp^{-\lambda t}$ should result into a straight line. Again the dead time can be estimated from the slope and the intersection point with the y-axis.

The singles count rates data are acquired from the phantom are representatives for that the nonparalyzable model is applicable to detector 1 or it is acceptable for detector 2. The same data for both detectors are fitted by the paralyzable model.

From the fits to the data using the paralyzable model, the dead time of each detector is estimated for detector 1 and for detector 2. This dead time is totally dominated by the off-detector electronics. This provides an estimation of the dead time in signals coming from of each detector and consequently in the coincidence rate.

Chapter 4

The first version of our dedicated PET

4.1 An introduction to the DoPET project

The goal of the DoPET project is the evaluation of a PET system as a dedicated method for dose monitoring in hadron-therapy.

DoPET project started since the beginning of 2006 within an INFN collaboration, with the purpose of realizing a small prototype of a clinical device. The system was fully validated through measurements on phantoms, in the perspective of a clinical application in tumor treatment monitoring at INFN-LNS (Istituto Nazionale di Fisica-Nucleare Laboratori Nazionali del Sud) in Catania by our group (Pisa group) [108].

The DoPET as a "On-line" PET[1] is applied to measure the β^+ activity distributions, which is produced in PMMA phantoms after the irradiation with hard photons. However, due to the fact that radiation and measurement are done in the same room, poor statistics (because of decreasing the number of positron emitters) and possibly for the relatively short-lived positron emitters like ^{11}C (with half-life of 20.33 min), 10 min for ^{13}N (with half-life of 9.96 min) and ^{15}O (with half-life of 2.04 min) could still be managed [129, 107].

The first version of the DoPET prototype, which has been constructed in INFN of Pisa, consists of two opposed $45mm \times 45mm \times 18mm$ LYSO planar detectors, 21×21 pixels ($2.0 \times 2.0 \times 18mm^3$ pixel dimensions) coupled to a square PS-PMT[2] (Hamamatsu H8500C). To reduce the number of collected signals, a position encoding readout was implemented: a detailed description of the prototype architecture and calibration procedures can be found in [108]. The distance between the two heads can be varied up to 20 cm, in view of the fact that the tomograph has to be set at the edges of a head-phantom during irradiation. The set up of the tomograph that has been used in measurements is shown in Figure 4.1.

For doing the experiments, different plastic phantoms were irradiated with a 62 MeV proton beam at the CATANA facility (LNS, Catania, Italy). The acquired data were processed using a fully 3D iterative algorithm to reconstruct the 3D β^+-activity distribution.

The experiments have proved the PET prototype capabilities to detect small differences in the practical proton ranges between materials of different density values, to map the internal structures of different chemical compositions, and to detect small range variations along the beam direction (with an accuracy near to one millimeter) and to locate air-filled cavities. These experimental results were reported in [109, 130].

[1] "On-line" PET dosimetry is a post-irradiation dosimetry, which is done in a proton treatment room).

[2] Position Sensitive Photo-Multiplier Tube

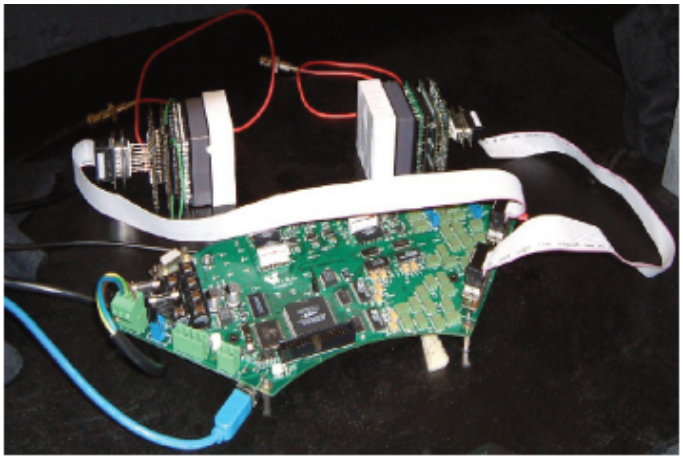

Figure 4.1: The experimental setup that was used for the measurements, where each head is composed of one module.

4.2 DoPET Architecture

The first tomograph architecture was made of two planar heads. Each head was composed of four components. These components have been illustrated in Figure 4.2. The structure has been designed somehow to provide the requirement of modularity for extension each head to 2×2 PS-PMT's arrays. In fact, by considering of compact size of the tube and its metal envelope thickness (of 0.25 mm) and assembling these tubes into an array, larger detection areas can be covered (with an improved active area of up to 89%) [131, 132].

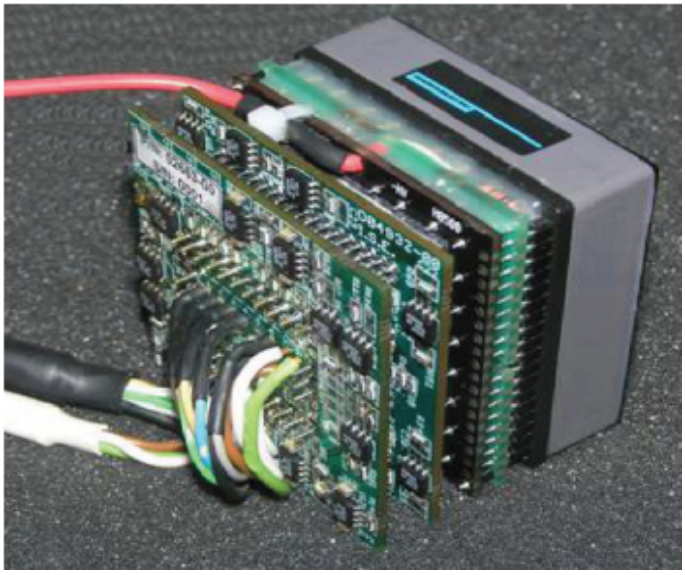

Figure 4.2: Module Constraints of first tomograph which was used in the experiments.

[1] Symmetric Charge Division
[2] Pulse Shape Amplifier
[3] Constant Fraction Discriminator

$LYSO : Ce(Lu_{2(1-x-y)}Y_{2x}SiO_5 : Ce_y, x \approx 0.1, y \ll x)$ scintillating crystal ($2 \times 2 \times 18mm^3$ pixel dimensions) has been glued to Photomultiplier (H8500C) by thermoplastic Cargille Meltmount™. Charge multiplication is provided by its 12-stage metal channel dynode. Charge collection and position calculation is satisfied due to the existence of 8×8 anodes (with the external size of $52mm \times 52mm \times 28mm$ and the active area of $49mm \times 49mm$). The PMT is connected to a SCD[1], which is responsible to read out the multi-anode PMT through a multiplexed system, and this is mainly based on networks which reduce the output of each tube to 2×2 signals. Afterwards a compact electronic board PSP[2] is used, which is in charge of signal amplification. Finally, a CFD[3] board is utilized to provide signal digitization.

4.2.1 DoPET's acquisition system

As it has been illustrated in Figure 4.3, in the pre-amplification stage of the acquisition system, the last dynode output signals from the PMTs are amplified by fast, low-noise pre-amplifiers. Then these signals are sent to the board for fast timing coincidence measurements. The role of a CFD in the time window at this stage is to provide timing independent of amplitude, which is generated by the gate for each photomultiplier tube. The constant fraction discriminator outputs are sent to a coincidence module that produces the gate signal in the PET mode. The output of each CFD directly generates the gate signal for the acquisition of the position signals.

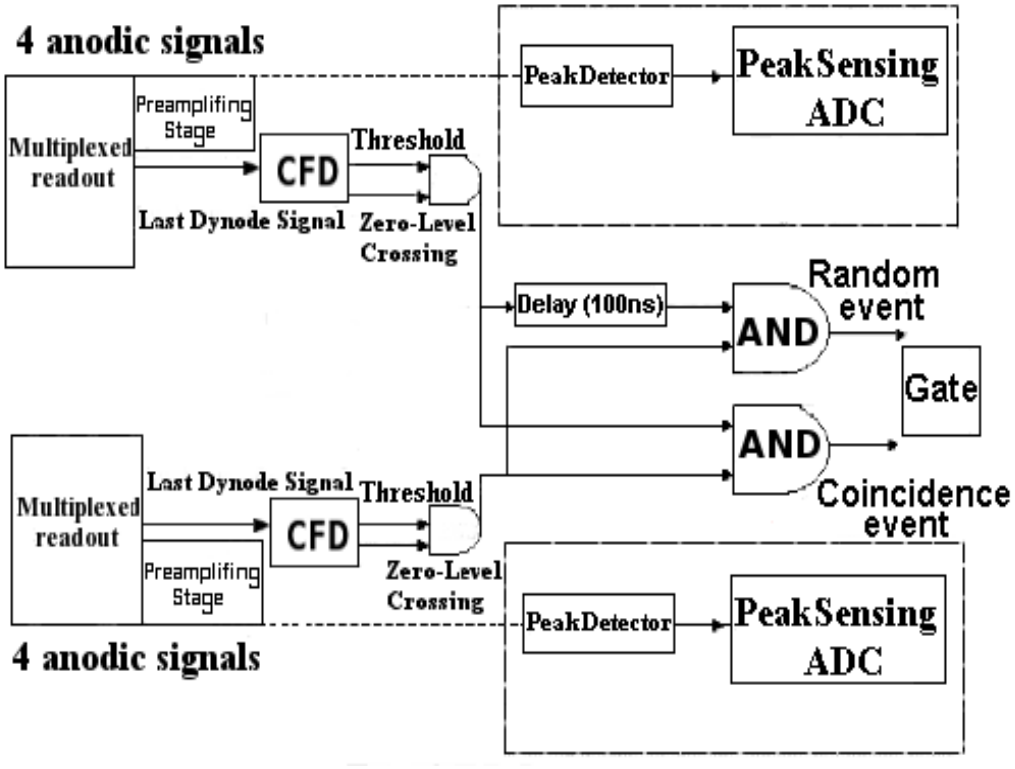

Figure 4.3: Schematic of the electronics for the data acquisition.

A second CFD output is delayed by 100 ns to generate a delayed coincidence window and the events collected in this delayed window in coincidence can be used to estimate the rate of the random coincidences used for corrections. The four position signals from each tube are digitized by a system composed of a peak

detector plus a peak sensing ADC. The digital data from both detector heads are then transferred to a local PC server and the point of interaction on the photocatode is then reconstructed off-line by software.

4.2.1.1 DoPET's acquisition software

The DoPET software for data acquisition and analysis has a server / client architecture. The Server application is dedicated to electronic equipment control and acquisition management. The client software communicates via Ethernet with the server software to drive acquisition. Both have a graphical interface, the former is needed to check the status of the electronic boards, to read and store pedestal values and to set mode parameters, such as SPECT or PET mode, number of data acquisition boards to operate (A or B), number of channels per board (A or B). The latter is used to set acquisition parameters, such as radioisotope type, injection time, number of events to be acquired or time duration of the scan. It also displays event rates on each channel and residual acquisition time. Client has also toolkits to perform off-line analysis of the acquired events, calibration, reconstruction of tomographic images and display of stored images. Figure 4.4 shows an example of the DoPET software.

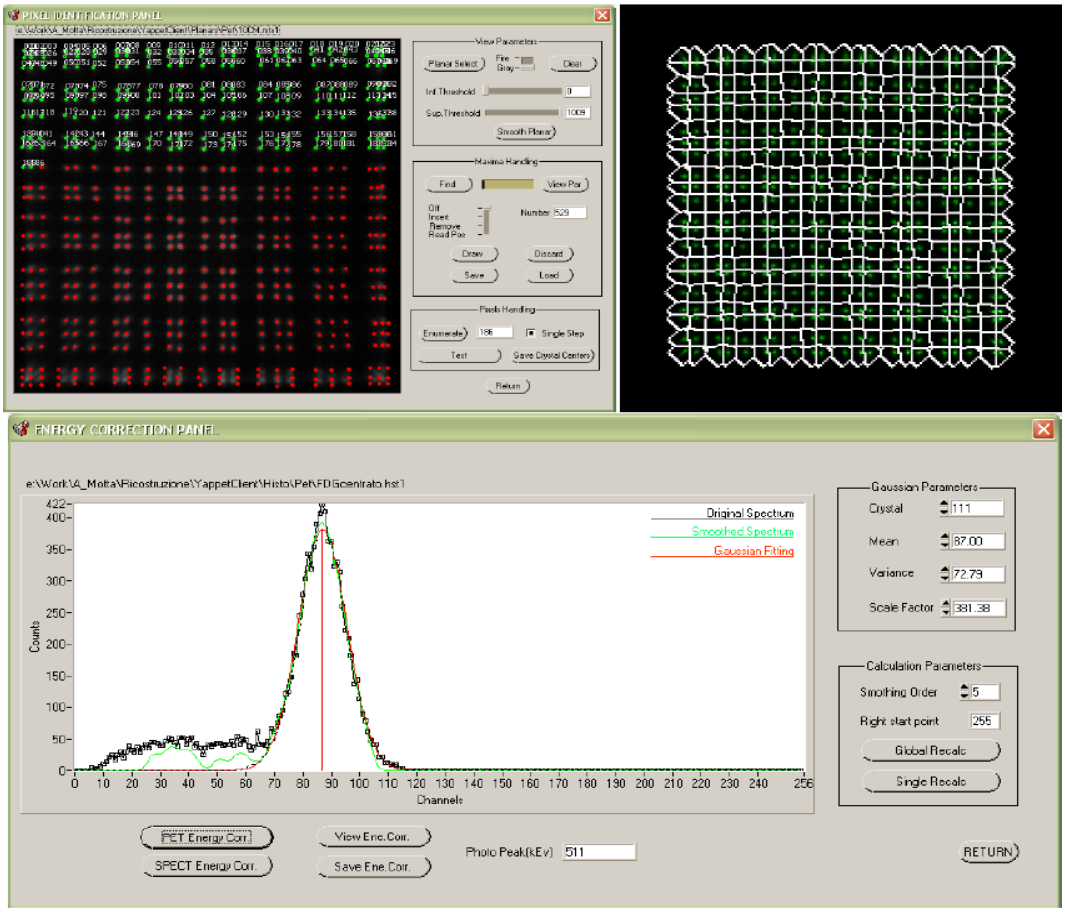

Figure 4.4: DoPET software. Top, left: graphical interface of the pixel identification software, used to determine the pixel center of gravity and to assign the proper numeration. Crystal centers coordinates are then stored and used to build the map for assign each event to the right crystal pixel. Top, right: the grid used for event assignment to pixels is shown, superimposed to the planar image used to generate it. Bottom: a screen-shot from the software used for energy calibration of single pixel spectra.

As it has been illustrated in Figure 4.3, each module of our detection module is composed of different parts. In the following, functionality of each part including is explained in details. The structure of detection module being used in the new version of our dedicated tomograph is nearly the same. Hence, three more modules are utilized to construct the new detection module of each head of our PET system. By applying this modification to the geometry structure of our module, the detection area has been increased by a factor four for each head. Thus, a new electronics for the data acquisition is necessary to detect the coincidence events.

4.2.2 Scintillator detector

In the new PET scanner detection module, $LYSOscintillator : Ce(Lu_{2(1-x-y)}Y_{2x}SiO_5 : Ce_y$ is used. It is composed of natural lutetium, Lu, that has a 2.6% radio isotopic content of ^{176}Lu ($t_{1/2}$ = 4.0×10^{10} years). This isotope emits β^+ particle and a cascade of high energy γ and X-rays. The choice of LYSO detector is based on its characteristics, namely:

1. High stopping power of the detector for 511 keV photons.
2. Fast scintillation decay time.
3. High light output per keV of deposited photon energy.
4. Good energy resolution of the detector.

The stopping power of the detector determines the mean distance the photon travels until complete deposition of its energy and depends on the density and effective atomic number (Z_{eff}) of the detector material.

The scintillation arises when a γ ray interacts with an atom of the detector material, and the atom is excited to a higher energy level, which later decays to the ground state, emitting visible light. The number light photons (photon yield), which are produced per keV of deposited energy depends on the type scintillation materials (in the case of LYSO the photon yield is about 25). The mean decay time is called the scintillation decay time and is given in nanosecond (in the case of LYSO is 50 ns). The shorter the decay time, the higher the efficiency of the detector at high count rates. A high-light-output detector produces a well-defined pulse resulting in a better energy resolution. The intrinsic energy resolution is affected by inhomogeneities in the crystal structure of the detector and random variations in the production of light (in the case of LYSO, the energy resolutions between 15% to 20% is acceptable) [109, 131, 133]. In Table 4.1, some of the main physical properties of different scintillators, which can be applied to PET scanners have been listed.

4.2.3 Position Sensitive Photo-Multiplier Tube (PS-PMT)

The second component of our detection module is a Hamamatsu H8500C photo-multiplier tube is to measure low levels of scintillation light. The structure of this PMT consists of a vacuum enclosure with a thin photo-cathode layer at the entrance window. An incoming scintillation photon deposits its energy at the photo-cathode and triggers the release of a photo-electron. Depending up on its energy, the photo-electron can escape the surface potential of the photo-cathode and in the presence of an applied electric field accelerates to a nearby dynode which is at a positive potential with respect to the photo-cathode. Upon impact with the dynode, the electron, with its increased energy, will result in the emission of multiple secondary electrons.

The process of acceleration and emission is repeated through multi-dynode structure of its structure lying at increasing potentials, leading to a gain of more than 0.5×10^5- 0.5×10^6 at the final dynode (anode).

Table 4.1: Physical properties of 6 different scintillation crystals

Detector Materials	Effective Atomic No (Z)	Density (g/cm^3)	Scintillation Decay Time (ns)	Photon Yield (per keV)	Linear Attenuation Coefficient (cm^{-1}) of 511 keV	Energy Resolution At 511 keV $(\%)$
BGO	74	7.13	300	6	0.96	10
GSO	59	6.71	50	10	0.67	9.5
LSO	66	7.40	40	29	0.87	10.1
YSO	34	4.53	70	46	0.39	12.5
LYSO	65	7.2	50	25	0.87	20
YAP	39	5.4	27	18	0.46	2.5

This high gain obtained from the H8500C leads to a very good SNR[1] for low light levels and is the primary reason for the applicability of this photo-multiplier tube as a component of our detectors. Moreover, the dynode structure of H8500C reduces the travel time of the electrons from the cathode to the anode, as well as reducing the variation in the travel times of individual electrons. In particular, this structure has a capability to restrict the spread of photoelectrons along their trajectory, thereby providing a position-sensitive energy measurement with a very little cross-talk between adjacent channels [113, 118]. The energy, timing, and location of gamma ray interactions information are coming from current signal distribution (from conversion of scintillation light due to the group of dynode segments) [134, 135].

The detailed characteristics of the 64 channel multi-anode photomultiplier of Hamamatsu H8500C have been listed in Table 4.2 [136]. Moreover, it should be mentioned that the QE[2] of PMT H8500C at 420 nm is 25%.

[1] Signal-to-Noise Ratio

[2] Quantum Efficiency: is a quantity defined as the percentage of photons (the deposition of energy by a single scintillation photon) hitting the photo-cathode surface and produce an electron-hole pair and a photo-electron escape from the cathode.

Table 4.2: Properties of Hamamatsu PMT H8500C

Parameters	H8500C
Dimensional Outline ($W \times H \times D$)	$52mm \times 52mm \times 27.4mm$
Effective area	$49mm \times 49mm$
Pixel size / Pitch at center	$5.8mm \times 5.8mm \times 6.08mm$
Dynode structure	12 stages
Cathode type	Bi-alkali
Peak Wavelength	400 nm
Spectral Response	300 nm - 650 nm
Gain	10^6
Rise time	0.8 ns
Cross-talk	3%
Transit time spread	300 ps
Supply voltage (between anode to cathode)	-1100 V
Window material	Borosilicate glass
Average Anode Output Current in Total	100 μA
Weight	125 gr

4.2.4 Symmetric Charge Division (SCD)

The third component of our detection module is the electronics readout. Hamamatsu H8500C would require a 64-channel readout.All 64 channels (one per anode of the H8500C) are coded into only 4 output lines for the position encoding readout of the H8500C tube. By reducing the number of channels that need to be read, the entire readout system can be significantly simplified, by providing a reduction of the number of analog electronic channels necessary for complete X and Y coordinate information readout. Hence, a charge division circuit based on the symmetric charge division scheme is utilized [137].

The circuit is a resistive matrix built of equal resistors and based on the orthogonal positioning algorithm. Each pad is connected to two resistors. Since the circuit is symmetrical, it provides anode current division into two equal parts; the first one is flowing into the X output line, and the other one to the Y output line. The X and Y line outputs are connected to low input impedance current collecting amplifiers. The other half in the Y collection op-amp. The charges are collected by 16 amplifiers, one for each of the X rows and Y columns [137, 138, 139]. The input characteristics of the amplifiers coupled to the readout matrix outputs determine the amount of parasitic cross-talk, noise, and circuit operation bandwidth [134, 140, 141]. The readout method is based on the processing of the analog signals after the linear amplifier front-end and it is illustrated in Figure 4.5.

The voltage can be converted to position by using a resistive division network. Amplification is performed before positional division and the amplified signal is robust enough to divide into a current signal proportional to position. This system performance gives superior performance with respect to a conventional resistive charge division. The final position of an event is determined by Eq. 4.1 and Eq. 4.2 after the two charge splitting stages. The digitization of the four position signals is then performed by peak sensing ADCs.

$$X = \frac{(X_+ - X_-)}{(X_+ + X_-)} \tag{4.1}$$

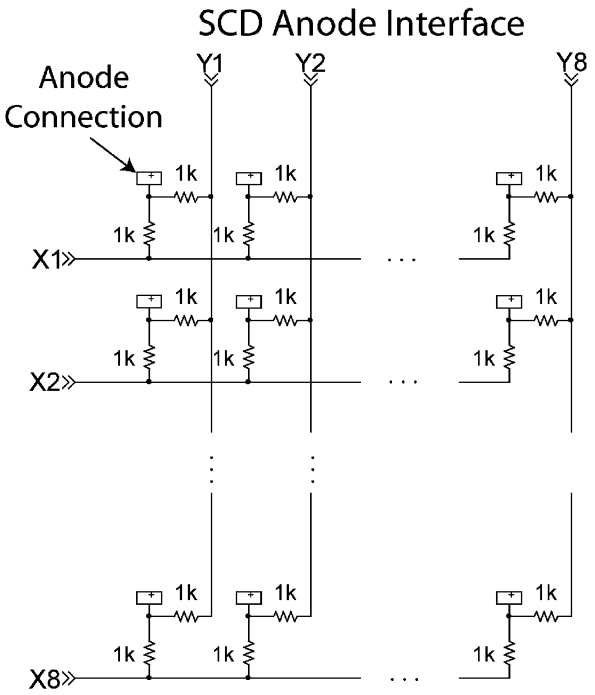

Figure 4.5: SCD anode interface presents constant impedance to the anode, dividing the charge into equal buckets of charge for collection on a ROW and COLUMN preamplifier.

$$Y = \frac{(Y_+ - Y_-)}{(Y_+ + Y_-)} \tag{4.2}$$

4.2.5 Pulse shaping Preamplifier (PSP)

Energy signals are preamplified and smoothed in a separated board, the pulse-shape preamplifier (PSP), and routed to the DAQ board for digital conversion. The role of the PSP is two-fold: on one hand it amplifies the signal in order to improve the signal-to-noise ratio and adjust dynamic range at the digital conversion stage, on the other hand it slows down the pulse, in order to introduce a certain time margin to allow the digital processing unit to resolve coincidences and trigger the acquisition.

A number of criteria are considered to choose the optimal shaping time for the detection system of the PET:

1. The shaping time must be long enough to collect the charge from the detector.

2. The shaping time must be short enough to achieve the high counting rates.

3. A shaping time has to be chosen that filters as much of the electronic noise as possible.

Electronic noise at the preamplifier output is created by a number of different aspects of the detection system. Some of these “noise components” have different frequency distributions, allowing us to use the filtering capability of the shaping amplifier to choose a shaping time that minimizes the noise for the detection system.

4.2.6 Constant Fraction Discriminator (CFD)

Choosing the right timing discriminator based on the detector characteristics for our intended application is essential. Hence, achieving the optimum time resolution is important in determining that events from two different detectors occurred simultaneously. The technique for deriving optimum time resolution depends on the type of detector and three major factors are limiting the time resolution:

1. Jitter
2. Walk
3. Drift

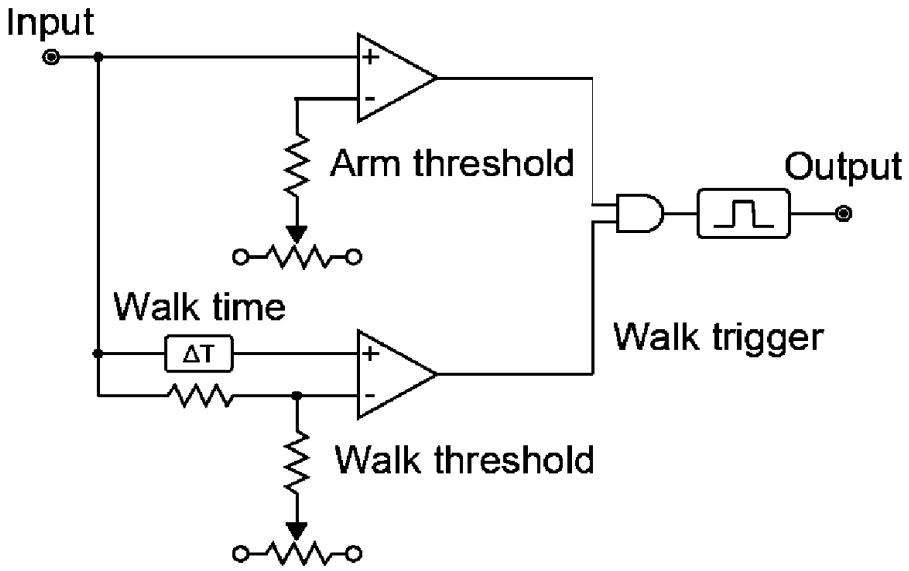

Figure 4.6: Functional Representation of a Constant-Fraction Discriminator [132].

The Primary function of the CFD is to mark the arrival time of the detected events with precision and consistency. It provides a reliable timing signal from analog pulses that have the same rise time and little variation of their timing with the amplitude of the input signal. Thus, it generates a fast logic pulse with a constant fixed offset in time with respect to the pulse. This temporal offset should not be a function of pulse amplitude; hence, the CFD avoids the threshold problem of leading-edge discriminators that leads to walk [142, 143, 144].

Figure 4.6 illustrates a simplified scheme of the constant fraction discriminator, which is used in the new version of DoPET. The signal discrimination is obtained employing two adjustable comparators, one for the minimum amplitude threshold and the other for the signal fraction threshold. The first is called arm comparator, the other walk comparator. The amplitude independent function that determines the digital trigger instant is the subtraction between the input signal f(t), delayed by ΔT, and an attenuated copy αf. The timing diagram of involved signals is reported in Figure 4.7. The understanding of the way the CFD works is principal for the fine tuning of front-end electronics. In the CFD, a delayed and inverted version of the anode pulse is subtracted from the attenuated anode pulse and when the result of the subtraction crosses zero, the logic pulse is generated. The time of the zero crossing is independent of the pulse amplitude. The attenuation fraction, f, which can be between 10% to 20%, and the delay, t_0, are the parameters to optimize

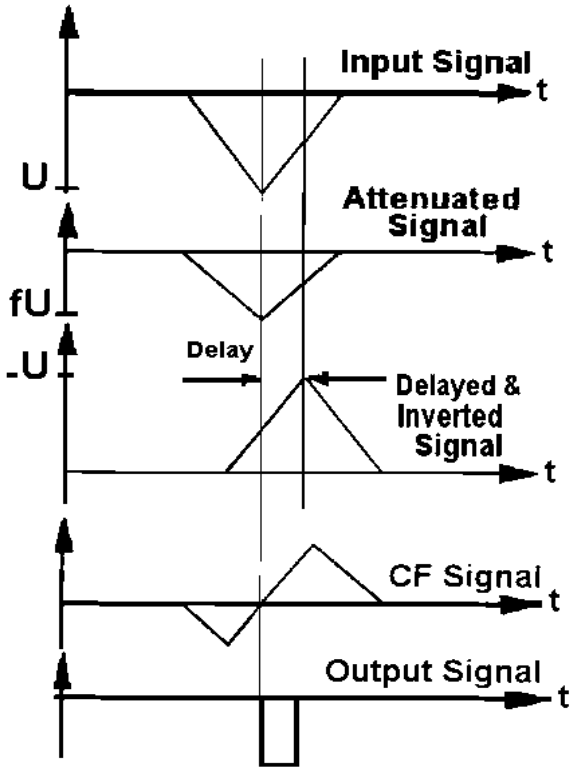

Figure 4.7: Principle for the CFD discriminator. The input signal is split into two identical pulses. One is attenuated a factor f (<1) and the other pulse is delayed and inverted. When the two signals are added up, the sum pulse will have a bipolar shape with a zero-crossing point.

the CFD with respect to the amplified anode pulse [145]. The procedure, which expresses the functionality of a CFD, is illustrated in Figure 4.7.

The CFD is one of the components that contributes most to the total system dead time, thus being a critical stage in the overall performance characteristics. Its dead time is of the blocking type, thus subject to paralysis at high count rates. Moreover, the timing precision of the generated trigger constitutes a major limiting factor for coincidence resolution and detection efficiency.

Chapter 5

The upgraded version of DoPET

5.1 Description of the new version

The new version of our PET scanner was designed somehow to provide a simple and adjustable planar geometry, to be used as "On-line" PET for dosimetry of proton beam in hadron therapy.

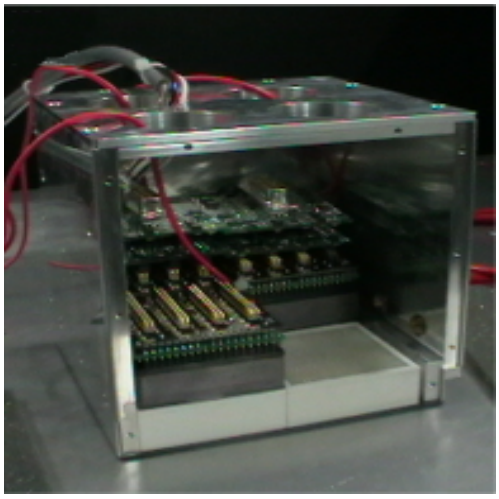

Figure 5.1: A detector block of our upgraded PET scanner. The modules are tightly packed and pushed towards the crystal matrix by means of metallic springs.

The structure is composed of two planar heads of $10.4cm \times 10.4cm$ each one mounted in front of each other. Each head contains four detector modules, which are tightly assembled and optically coupled to the scintillator crystals. Each scintillator is a LYSO matrix of 23×23 pixels $1.9mm \times 1.9mm \times 16.0mm$, with a 2.0 mm pitch and a total active area of $46mm \times 46mm$.

Each matrix is coupled to a multi-anode PMT (H8500C). Each detector module has 64 output signals, which are proportional to anode current, and have to be considered for energy and position characterization. These output signals and a a timing signal, which is taken from the last dynode, pass through a conditioning stack made of a coding board, a pulse shape preamplifier board (PSP) and a timing board.

The coding board consists of a Symmetric Charge Division resistive network. The SCD reduces the 8×8 anode signals of each PMT into 8 + 8 signals, that codify separately the X and Y centroid of the PMT currents. These 16 signals enter a passive resistive chain that further reduces the number of signals to Anger-like 2 (x) + 2 (y) [137]. The last dynode signal is passed through up to the Constant Fraction

Discriminator (CFD) [146], which is the last board of the stack. The CFD generates a differential PECL trigger synchronous to the crossing of a variable voltage threshold that corresponds to the 17% of the energy pulse peak level. The outputs of the whole module consist eventually of four analog Anger-like signals, which are sent to a Data Acquisition (DAQ) board, and a digital timing signal that goes directly to the Control FPGA for coincidence processing [147].

5.2 Overall architecture of the acquisition system of DoPET

The acquisition system, which has been designed specifically for the modular head detectors is illustrated in Figure 5.2.

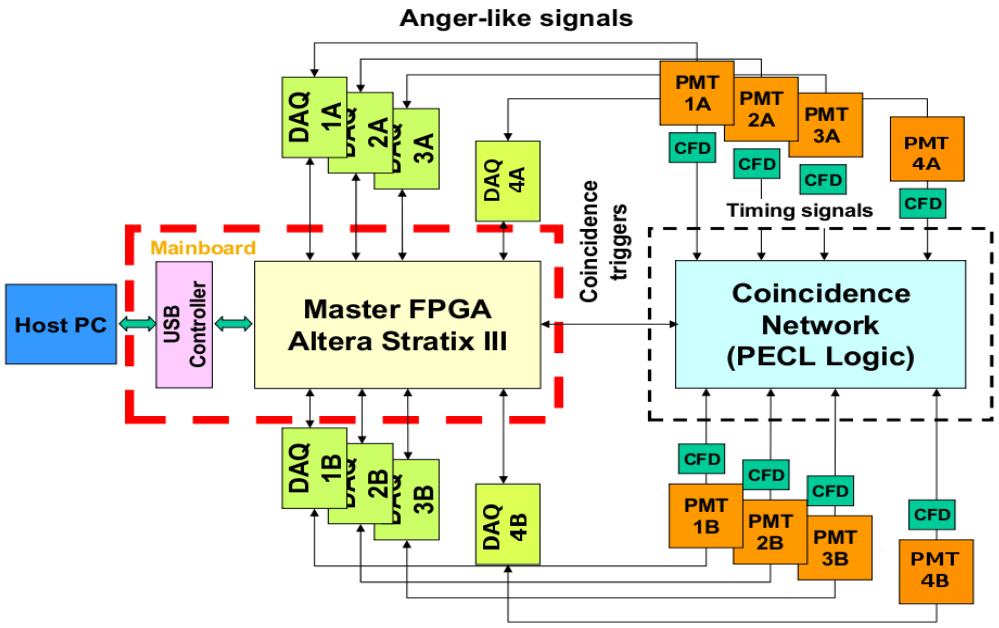

Figure 5.2: Scheme of the acquisition system, which was applied for the new version of DoPET. It represents a modular detector system (4 VS. 4 modules).

Coincidence triggers are processed by the FPGA which keeps track of past events and triggers the interested DAQ for energy acquisition. Event tracking provides a robust control over pile-ups and enhances data transfer efficiency from the DAQs. DAQ boards operate independently from each other; therefore, only a fraction of the system is busy during the acquisition of each coincidence. This, together with an adequate buffering on each DAQ, allows multiple simultaneous acquisitions, which is the key for dead-time reduction. The data link between DAQ boards and mainboard is obtained with two asynchronous 16-bit wide parallel buses, one per detector side. This choice has been made so as to keep the asynchronous boundary between all involved boards, which is commonly referred to as GALS[1] system design, particularly suitable for lowering system complexity and power consumption [148]. Tests showed that proper buffering and efficient data retrieval from the DAQ boards make the bandwidth of this kind of connection well sized with respect to the rest of the system [147].

[1]Globally Asynchronous Locally Synchronous

5.2.1 The mainboard

Due to the fact that the geometrical efficiency loss can be largely compensated by a gain in count rate characteristics, a flexible and expandable acquisition system was specifically designed to work with the modular detectors.

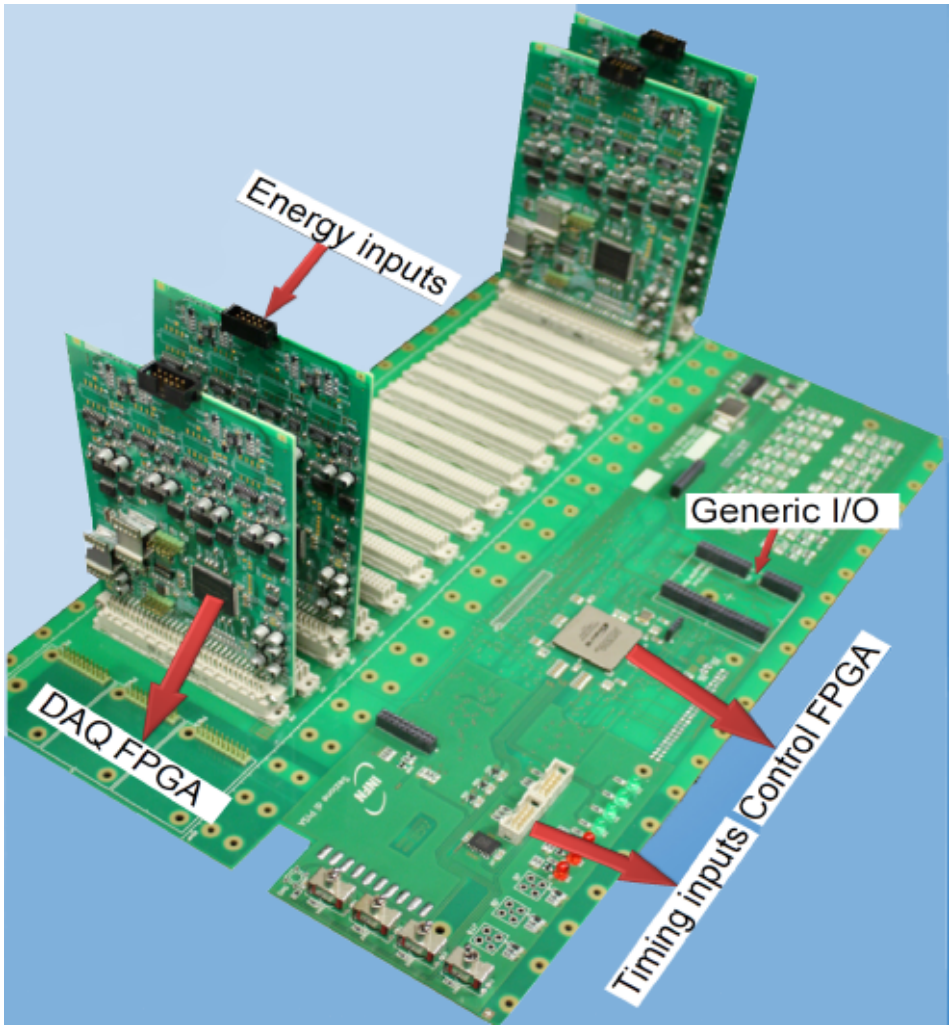

Figure 5.3: The mainboard of the new version of DoPET. Four DAQ boards have been connected. The current acquisition implementation is capable of handling up to 18 DAQ boards.

The mainboard, which has been illustrated in Figure 5.3, powers the whole system and provides data connection. It is equipped with a high-end model FPGA Stratix III (Altera Corp., San Jose, CA, U.S.A). The FPGA must have enough memory to buffer incoming data from the coincidence network and all the DAQs, and must be fast enough to send acquisition triggers in time to fetch energy peaks. The FPGA provides high memory resources, needed for data buffering, high I/O pin count and low propagation delays, required for prompt coincidence monitoring. It streams data to the Host PC at 480 Mb/s through an USB 2.0 controller, which is a CY7C68013A FX2LP (Cypress Semiconductor Corp., San Jose, CA, U.S.A), and is connected asynchronously to the coincidence and DAQ boards. The mainboard also provides circuitry necessary for logic translation and physical socketing for the DAQ boards. The 4 DAQ boards, which have been mounted on the mainboard are controlled by the Cyclone II FPGA (Altera Corp., San Jose, CA, U.S.A)

and implements four peak detectors.

5.2.2 The DAQ boards

Each DAQ[1] board mounts a Cyclone II FPGA (Altera Corp., San Jose, CA, U.S.A.), which implements buffering, bus control and triggers the four on-board peak detectors. The DAQ board converts signals from the PMTs with four 12 bit ADCs. The results of the conversion are stored in an interfacing FIFO accessible by the mainboard. The components are:

1. Sensors that convert physical parameters to electrical signals.
2. Signal conditioning circuitry to convert sensor signals into a form that can be converted to digital values.
3. Analog-to-digital converters, which convert sensor signals to digital values.

Figure 5.4 shows a DAQ module. Each DAQ board is provided with an input inductive delay pad, which is used to compensate coincidence processing delay.The implemented delay must be sufficiently long in order to turn on the peak detector before the actual energy signal peak has passed through. The input stage of the board also provides a pedestal leveling circuitry. In fact, a positive pedestal value is required so as to correctly convert the incoming signals. This depends on the fact that the ADC input stage has been configured having ground as lower dynamic range bound.

Each peak detector, when active, follows the voltage of an incoming Anger coded signal from the PMT and holds on the highest value, which is in turn converted by a 10 MHz, 12-bit A/D converter. Peak hold and registration is enabled only after an acquisition trigger is received from the main board. This is because RC peak followers could not sustain charge-discharge cycles at typical single photon rates.

The total DAQ dead-time is composed of two main contributions: the peak waiting time, and the time required by the voltage-followers capacitors to discharge. The peak waiting time is the programmable interval during which the DAQ is turned on and follows the Anger signals (Figure 5.5).

5.2.3 The coincidence board: To record coincidence events

In order to collect data corresponding to only coincidence events within the bulk of singles, a coincidence board as a component of the new DoPET's acquisition system was constructed. Thus, the raw timing information was processed in this board. Events are identified as coincidence events, has to fulfill three criteria:

1. Come from opposite heads of the scanner.
2. Be within a pre-determined timing window (few nanoseconds).
3. Have an energy above the pre-selected threshold.

The first and second condition dictate a centralized approach for digital coincidence analysis, where all events must pass through a single analysis gateway. The proposed coincidence architecture follows the principles where sorting and coincidence analysis take place in different boards. Successive window-timing is a way to discard irrelevant events when they reach different detector heads from different β^+ annihilation. Single events can be identified by a proper coincidence window, which can be set and adjusted

[1] Data Acquisition Board

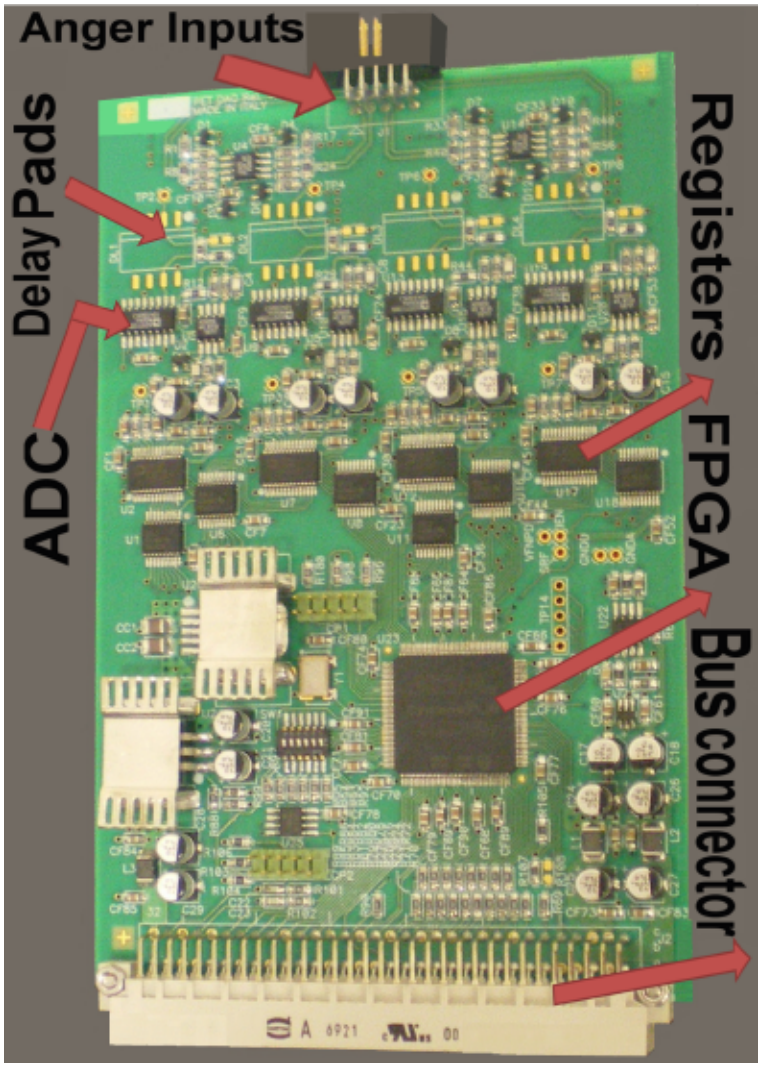

Figure 5.4: The DAQ module of the new version of DoPET.

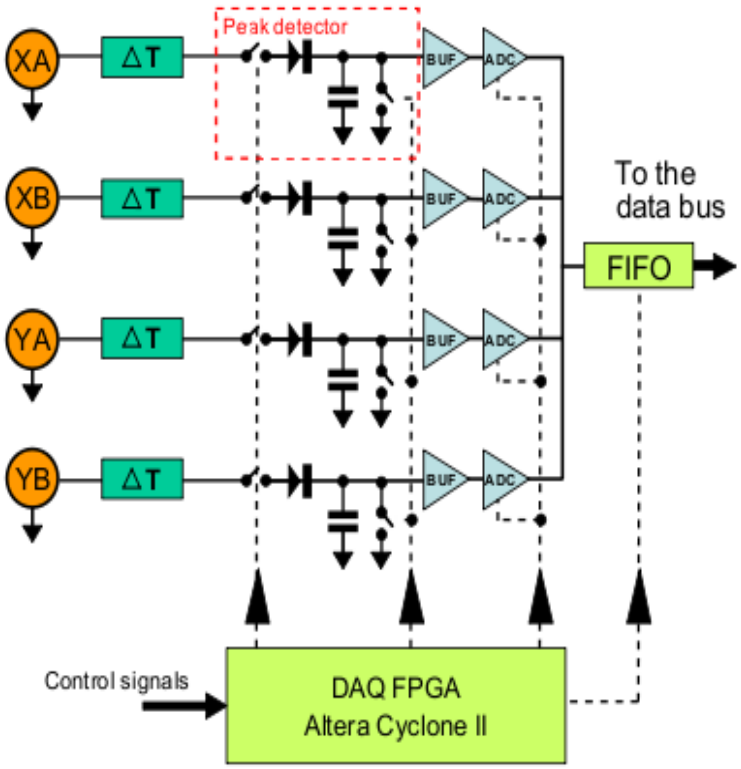

Figure 5.5: Schematic architecture of the DAQ board of the new version of DoPET. XA, XB, YA and YB are the Anger coded inputs coming from the SCD board [132].

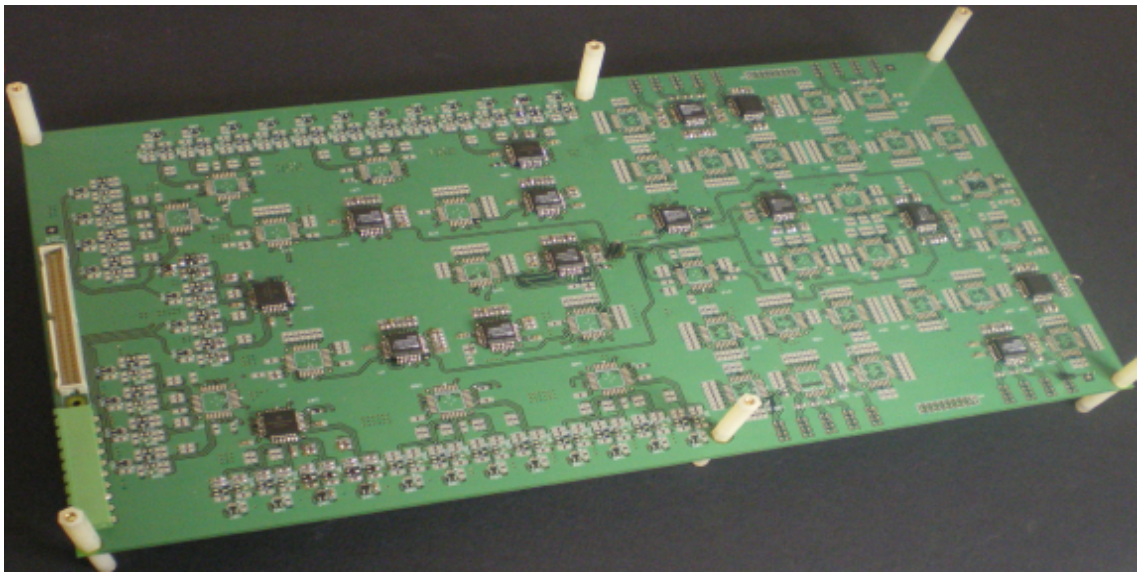

Figure 5.6: Photograph of the new coincidence board where both standard and novel delayed method have been implemented.

by an equalizer on the board. Thus, single events can be removed in order to decrease image noises and increase efficiency of the PET system [149].

The coincidence board receives timing signals from the CFDs in order to reject unqualified events and provides pile-up rejection logic outputs to ADC and individual ADC gating signals.

By utilizing a fast PECL[1] network of AND gates on the coincidence board, proper and enough coincidence events could be detected. Hence, the better physical characterizations such as efficiency and sensitivity are provided for the new version of DoPET.

1. Working in the sub-nanoseconds range and offering wired-OR gating.
2. Reducing logic cost from O(n^2) to O(n), due to the the wired-OR capabilities of ECL.
3. Feasibility of doing very fast data or signal processing.
4. Minimizing crosstalk between the different electronic components.
5. Minimizing the number of lines required for interconnecting the subsystems due to the bandwidth and line driving capabilities of ECL without sacrificing the overall performance.

Figure 5.6 shows the coincidence board. This board, which was used as a part of the acquisition system is made of glass epoxy, double sided with dimension of $21cm \times 40cm$. It has solder mask and silk screen printed on both sides for easy assembly of the components [150, 151]. The operation principles, which are followed to detect the coincidence events, are illustrated in the following. The two methods, which were implemented on this board to estimate random events have been explained in more details (Appendix A).

5.2.3.1 Prompt coincidence

With implementation of the new delayed window approach (Appendix A) in a configuration of 4 PM-tube modules versus 4 PM-tube modules dual head system, A_i and B_j signals are the timing signals from modules i and j on A and B side, respectively. The trigger scheme for a prompt coincidence is illustrated in Figure 5.7 and Figure 5.8. The acquisition of signals of a module i of the A side is triggered by CDA_i when a logic AND between A_i and the OR of all the B side is detected. Simultaneously, the acquisition of the module j on the B side is triggered by the corresponding signal CDB_j.

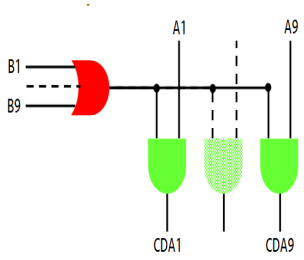

Figure 5.7: Trigger scheme for a prompt coincidence.

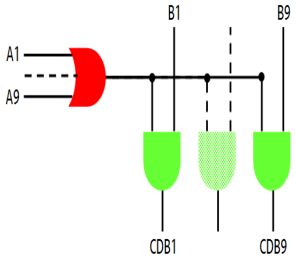

Figure 5.8: Trigger scheme for a prompt coincidence.

[1]Positive Emitter Coupled Logic. PECL is a standard ECL devices run off of a positive power supply.

5.2.3.2 Delayed coincidence

As it is shown in Figure 5.9 and Figure 5.10, in the delayed window scheme A_i and B_j signals are the timing signals from modules i and j on A and B side, respectively. The acquisition of signals of a module i of the A side is triggered by DDA_i when a logic AND between delayed timing signal A_i (by ΔT) and the OR of all the B side timing signals is detected. The acquisition of signals of a module j of the B side is triggered by DDB_j when a logic AND between the timing signal of a module B_j and the OR of all the delayed timing signal A_i (by ΔT) is detected.

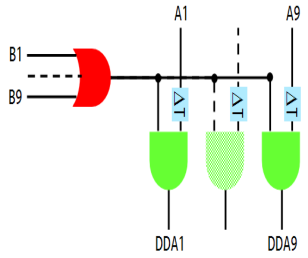

Figure 5.9: Delayed window scheme.

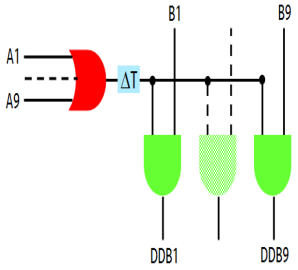

Figure 5.10: Delayed window scheme.

5.2.4 The rationale to apply FPGA

Due to the results that were achieved from utilizing the designed coincidence board for the detecting coincidence events, some problems arose that created difficulties. They have been described in more details in chapter 6. Hence, another method, which is commonly utilized for data acquisition in modern PET scanners was applied in order to detect coincidence events [152, 153]. The coincidence procedure as logical functions was implemented in Stratix III FPGA[2] (Altera Corp., San Jose, CA, U.S.A.) as part of the acquisition system by using HDL[1]. By applying this method, the high count rates could be handled and there is also the capability to increase the number of the channels read out.

This method requires low device resources and no specific peripherals and has the capability in computing power and I/O sophistication to resolve coincident digital pulses within a time window of few nanoseconds. Moreover, it is well suited for implementing low level triggers by using logic resources.

There are two ways of implementation coincidences procedure in Stratix III FPGA:

1. AND-gating.
2. TDC[3].

AND-gating method was implemented in the Stratix III FPGA (Altera Corp., San Jose, CA, U.S.A.). This method has two advantages with respect to the TDC method.

- It is much simpler.
- It is cheaper to be implemented.

The concept of AND-gating is that for each photon, a digital pulse of width W (which is of the order of few nanoseconds) is generated and combined with the pulses coming from other detectors. The total circuit generates a coincidence trigger whenever two pulses overlap, resulting in a coincidence resolution of 2 W.

[1]Hardware Description Language
[2]Field-Programmable Gate Array
[3]Time-to-Digital Conversion

5.2.4.1 Embedded synchronous coincidence processor in the FPGA

The coincidence processor operates at the maximum clock frequency available in the Stratix III FPGA, which ranges from 300 MHz in low-end devices to about 800 MHz in high-end ones. Figure 5.11 illustrates the overall architecture of the FPGA acquisition system. Multiple clock domains are possible with the use of embedded digital clock managers, and cross-domain synchronization chains prevent the propagation of flip-flop metastable states. Two synchronization batteries are located at the coincidence processor input and at the system input. These are responsible for the coincidence processing latency. The latency is established by the synchronization stage (indicated as kτ). The number of chained flip-flops and the clock period are indicated by k and τ respectively. The metastability resolving time R relies on the electrical characteristics of the target device and must be lower than kτ [154].

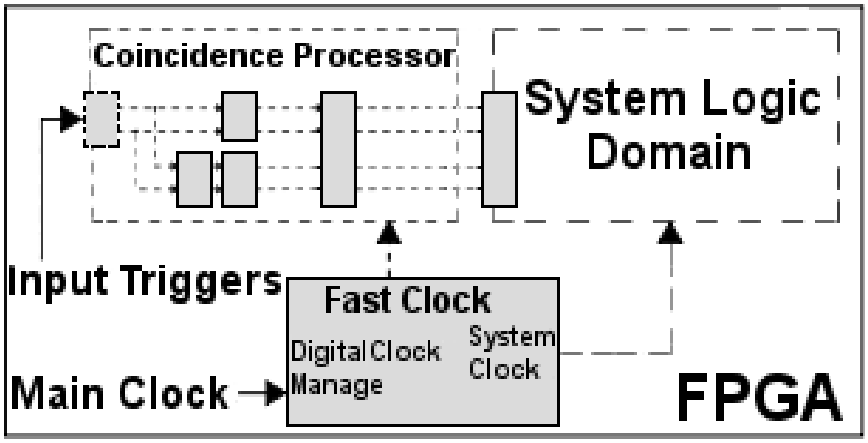

Figure 5.11: Overall architecture of a FPGA acquisition system with an embedded synchronous coincidence processor. The digital clock manager is a standard component.

Figure 5.12 illustrates, how procedure of shaping the incoming signals to one-cycle pulses and feeding both to a synchronous AND-gating network coincidence detection can be done. Within the synchronous domain, two signals rise during the same clock period. In this way all events that are separated by a delay greater than the clock period τ are discarded. However, all of the events, which fall at the two sides of a clock rising edge, will also be lost. It is referred to this undesirable condition as a hazard. One way to recover hazards could be to use two-cycles pulses. In this way, all events closer than 3τ are guaranteed to be resolved as coincidences.

Once all the inputs have become synchronized, coincidence gating is a relatively simple task. The combinatorial function is very specific for a given PET geometry. In our case, a modularized dual planar PET geometry has been implemented, in which each detector is made of n modules. With this geometry each module A_i of one side can receive a photon in coincidence with a module B_j of the other side. The gating function can then be expressed with a boolean expression, where $C_{A,i}$ and $C_{B,j}$ are the coincidence outputs.

$$C_{A,i} = A_i \cdot \sum_{j}^{n} B_j \tag{5.1}$$

$$C_{B,j} = B_j \cdot \sum_{i}^{n} A_i \tag{5.2}$$

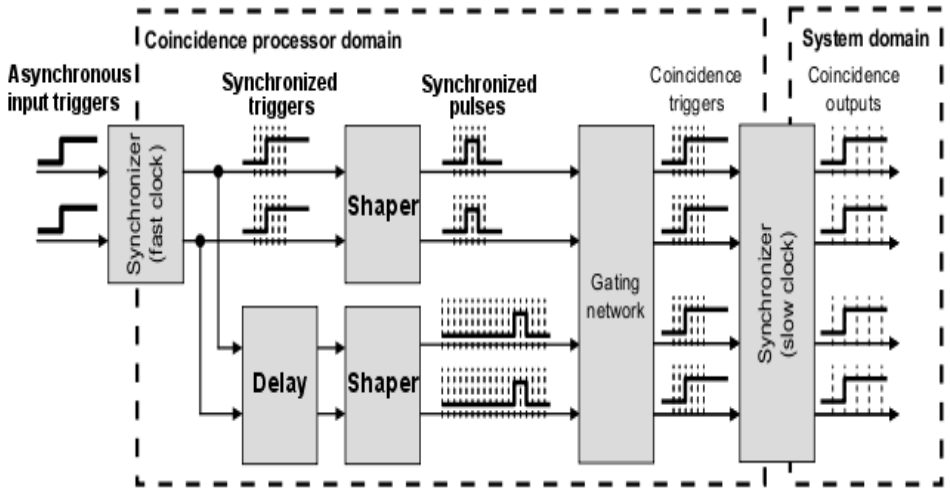

Figure 5.12: Detailed block diagram of the synchronous coincidence processor. Input pulses are synchronized with the boosted clock and combined according to a configurable AND-gating network. Coincidence outputs are then re-synchronized with the slower system clock.

At high clock frequencies and with a high number of detectors it might be necessary to divide the function in pipelined stages, in order not to incur in timing violations. Pipelining has the negative effect of increasing resources usage and detection latency by τ per stage.

Random events counting has been achieved with the delayed window technique (Appendix A). Delays have been realized using a series of shift registers. The gating function implements a variation of the delayed window technique, in which only prompt events are triggered for acquisition [133]. The adopted technique has the advantage of eliminating the detection latency due to the window delay [132].

5.3 The criterion to upgrade the DoPET

The factors, which have been listed below, are considered in the conceptual design of the acquisition boards and the modular detectors as a part of the acquisition system for data collecting of the new version of DoPET. However, the following aspects cannot be achieved and optimized simultaneously:

- Detector geometry,
- Event rate,
- Readout,
- Support structures, cabling, and
- Cost

The major physical characteristics, which were provided by the aforementioned factors were listed in the following. Moreover, the way and how are they feasible has been discussed.

1. Detection efficiency,
2. Reducing the system dead-time.
3. Reducing the probability of electronic pile-up.

4. Spreading the coincidence events.

Detector architectural design has provided a better detection efficiency for the new version of DoPET. This is due to the architectural design, which includes the acquisition system, plus the segmentation of detector area into the several readout channels and the use of a highly integrated readout circuitry. This allowed us to achieve more active detection area, capability of handling more event rate, thus eliminating electronic noise. If a detector of the detection module is exposed to a uniform rate R, subdividing the detector into n segments reduces the rate per readout channel to R/n (which is much more manageable).

By doing the segmentation for one module into n modules, dead time reduction (f_{dead}) could be estimated by the following formula [131]:

$$f_{dead} = \frac{n^2}{n^2 - (n-1)^2} \tag{5.3}$$

For instance, if the value of the segmentation is 4 ($n = 4$), which is the case that was considered for the DoPET (with 4 detection modules versus 4 detection modules), the dead time reduction (f_{dead}) would be a factor of 2.28.

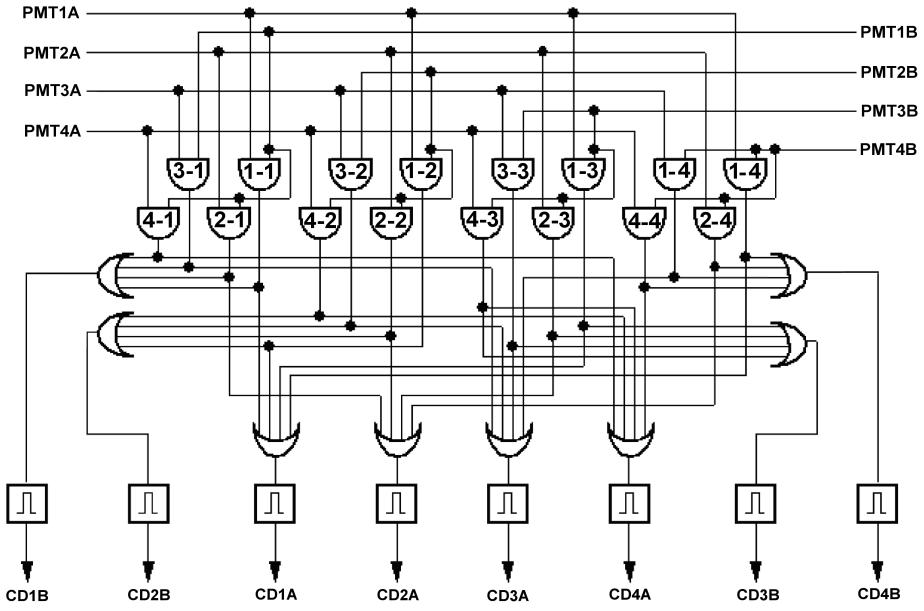

Figure 5.13: Coincidence detection components diagram for the case of a system with configuration of 4 PMTs versus 4 PMTs.

From a geometrical point of view, each head of the detection module has been designed to include 2 by 2 blocks. In this way, a larger number of coincidence events is expecting to be detected. However, the issue is how to manage the coincidence events from the detected events. The coincidence implementation on a Stratix III FPGA was the solution that was utilized. In the following the concept of this method and a short brief description of the procedure is given.

Each PMT is connected to a corresponding constant fraction discriminator, which is in charge of generating a digital pulse with a well defined delay after a light pulse arrival. The digital pulses (that is called

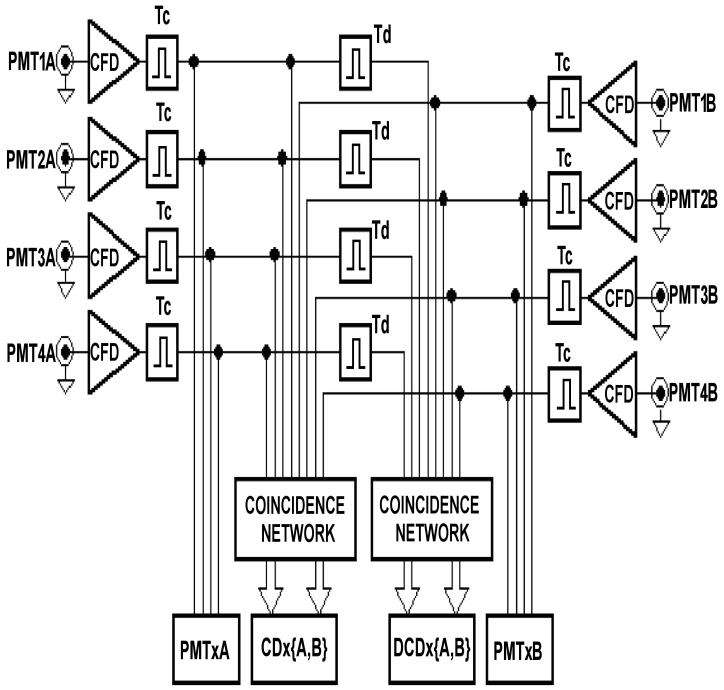

Figure 5.14: Coincidence network for the DoPET system with configuration of 4 PMTs for each head of the detection.

$PMTx_A$ for the side A of the scanner and $PMTx_B$ for the side B) are routed through an OR-AND network to generate the $CDx_{A,B}$ signals (shortly CD_x) which are asserted every time two light pulses arrive in coincidence (within a well defined interval). For calibration purposes, it is also important to count delayed coincidences (DCD_x), which are detected by the coincidence network in the same way as the real ones, but inserting a different delay between light pulses from the two sides. The mentioned behavior has been schematized in Figure 5.13 and Figure 5.14.

CD_x signals are the designed triggers to start voltage sampling in the data acquisition boards. They are also routed to the MF[1], together with DCD_x and PMT_x, to keep track of DAQ boards status and compute statistics. A set of rules can be defined to allow coincidence acquisition, pile-up[2], coincidence correction and event labeling. These rules are coded in proper finite state machines inside the MF. Every time a DAQ acquires an event, it writes significant data about that into a built-in FIFO, and waits for another trigger. .

The MF continuously empties DAQ-FIFOs and transmits their contents to the Host. Multiplexing at our modular approach allows spreading of coincidence events among the modules, thus reducing both system dead time and electronic pile-up probability in each detector. This allows to increase sensibly the field of view without increasing the NEC[3]. The modularity is kept from the front-end to the traffic unit in which acquired events are merged and collected.

[1]Master FPGA

[2]✓The energy discrimination criteria is satisfied by the combined energy of the two events, so one event is recorded at a position which is the weighted average of the two events' positions.

✓The combined energy of the two events exceeds the high energy threshold, and both events are lost. Thus, at very high counting rates, pile-up can become a limiting factor and may degrade resolution and introduce artifacts [155]

[3]Noise Equivalent Count Rate

Chapter 6

Performances of the new DoPET prototype

6.1 Introduction

The major goal of the project is developing a detection system for obtaining a good quality and detailed image of low β^+ activity distribution in order to be applied for "On-Line" dose range monitoring in hadron therapy. Achieving this depends on how well the PET scanner performs in image formation. To obtain a good image quality, parameters such as spatial resolution, dead time, detection efficiency, are critical. These parameters are interdependent, and if one parameter is improved, one or more of the others could be compromised.

Improving sensitivity and spatial resolution are the two main issues, which were considered in the designing of the DoPET. Sensitivity is related to the detection efficiency of the detectors for 511 keV photons, the packing fraction of the detectors and the solid angle covered by the detectors. However, sensitivity alone is not sufficient to obtain good image quality. It has also to be combined with other features such as low system dead time, high energy resolution and good timing resolution. PET systems operated in 3D mode limit the scatter fraction (SF) of the acquired data by setting a narrow energy window around the 511 keV photo-peak. With a good energy resolution, the energy window can be set to minimize scatter without loss of detection efficiency at 511 keV. With good timing resolution the level of random coincidences can be minimized by setting a time window equal to the trans-axial imaging field-of-view (FOV) of the system.

While the previous chapters (chapter 4 and chapter 5) discussed the detector optimization, the final assembly has been reached and a complete calibration of the detector has been performed.

6.2 The coincidence board performance

The rationale for using the coincidence board was to increase coincidence efficiency for the new PET system in order to cover better data statistics (from acquired data). The coincidence board receives the timing signals from the PMTs after the digital conversion performed by the CFD. The outputs from the CFD are shaped to have a time duration T_c and are routed to the FPGA with a series of flat twisted cables, driving the + 5V, - 5V, GND, and the differential Positive Emitter-Coupled Logic (PECL) outputs. CFD thresholds can be set with trimmers mounted on the CFD boards while the signal time delays can be set with trimmers mounted on the coincidence board.

One of the main components on the coincidence board is a quad flip-flop MC100E131, which operates at +5 V, absorbs 58 mA and is used as a chip for monostables, which are responsible for digital pulse shaping in the DoPET (The pulse shaping circuit was developed by AGE Scientific). Each flip-flop is terminated with a couple of 180Ω resistors that drain 40 mA. Hence, a single monostable drains about 55 mA at +5 V and consumes about 275 mW.

The coincidence network resolves simultaneous occurrences of two input triggers, within a time window 2 τ_c. The discrimination is achieved AND-gating the input signals of fixed length τ_c from the 4 PMTs of head A with the signals from the 4 PMTs of head B. The resulting outputs, CDA_i and CDB_j, designate which of the 8 tubes were involved in the coincidence event [150, 151]. These signals are then directly routed to the DAQ boards to trigger the peak detection and A/D conversion. The triggers are also routed to the main processing unit to enable real-time activity analysis. An equivalent coincidence network is used for the random coincidence measurement [131].

Four parameters must be optimized in the coincidence board:

- Input equalization, to compensate for differences in cables propagation delays.
- Coincidence and random coincidence window, which represents half the coincidence resolution.
- De-correlation delay, to generate random coincidences.
- Output shaping, to allow combinatorial outputs to be synchronized at frequencies compatibles with the adopted FPGA technology.

To perform this task, the shapers are arranged as illustrated in Figure 6.1.

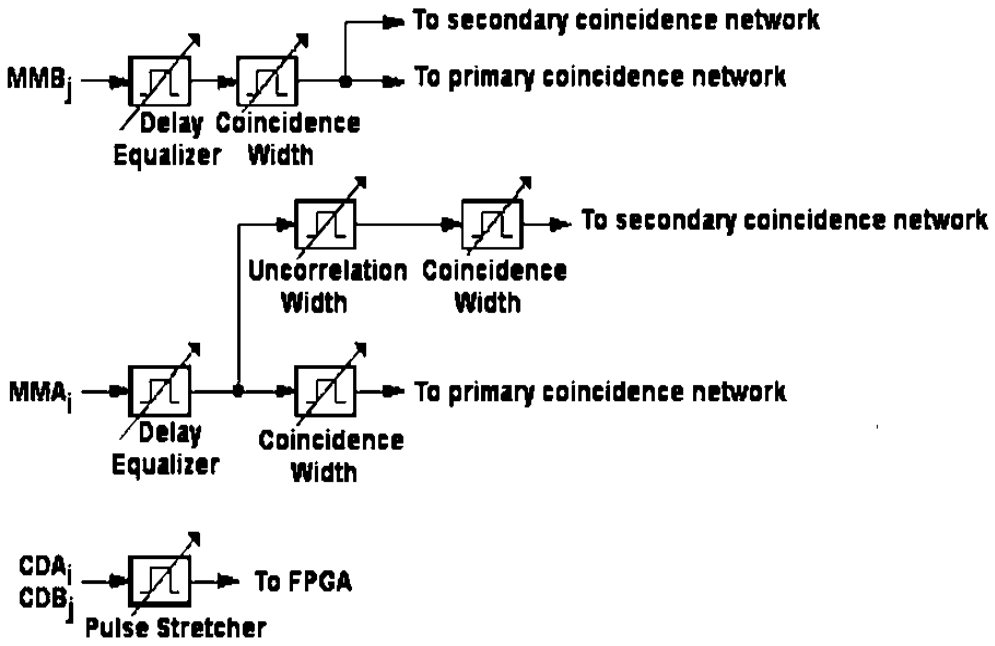

Figure 6.1: Schematic configuration of monostable circuits to implement the shaping functions.

The Gate and Delayed Gate signals were regulated to 6 ns. The reason was that the timing resolution for a typical LYSO based PET detector is approximately 5 to 6 nanoseconds and the width of the logic pulses, τ, should be at least as wide as the timing resolution of a pair of detectors (measured in FWHM) [113, 111, 124]. An Absolute Delayed signal was given a value of 50 ns (a delayed time of 50 ns is needed between recording 2 different coincidence signals, which are detected in the detector module according to a value of 40 ns as the decay time of LYSO).

As it was defined in section 5.2.3.1, when prompt coincidences are considered to be detected, delayed signals are not expected to be present in the outputs of PECLs. By checking the outputs of PECLs, some delayed signals were detected, which were undesired signals. The next step was to remove those signals and this became feasible by simply changing IC components (with type of GATE AND/NAND QUINT 2IN 28PIN). Hence, six pieces of the aforementioned components replaced the old ones. Moreover, a feedback resistor was inserted between the two ICs in order to diminish all of the delayed signals.

Several experiments were done on the board to specify physical characteristics and optimize the coincidence network in order to achieve better image quality for the PET scanner. As the time window coincidence was decreased to a certain value of 2$\sim$3 ns coincidence width for the timing measurements of the new system, many true events were missed due to the existence of large amount of time jitter. It was understood that the properties of the board was not well enough as expected. Hence, the coincidence board was replaced by an FPGA-based coincidence technique and a new version of motherboard was utilized.

6.3 Flood Histogram Performance

The characteristics of the PMT used for each head are listed in the Table 6.1. The values of high voltage supply have been chosen in order to best profit of the dynamic range of the ADCs. Slight adjustment (of few tens of volts) are necessary depending on the supply used to power the electronics boards. Therefore energy calibration and noise spectrum acquisition must always be performed before a new set of measurements.

Table 6.1: Specific parameters of the PMT used in the final detector.

head	Anode Luminosity $[A/lm]$	Anodes Gain Spread $[max/min]$	Dark Current [nA]	PMT Supply [V]
1	147	1.9	2.35	868
2	181	2.84	1.6	852

A block detector has a 2×2 LYSO scintillator matrix, which is composed of four matrix of 23×23 arrays, the pixels are $1.9mm \times 1.9mm\times$ with 0.1 mm separation and 2.0 mm pitch segments-in both the X and Y directions that covers the $49 \times 49mm^2$ PS-PMT.

The crystal array was polished on one face and directly coupled to the 1.5 mm thick glass window of the PSPMT (the other 5 faces of each crystal were "as cut") without any additional light diffuser but with a 3 mm epoxy on the both sides. The PSPMT has a $46 \times 46mm^2$ sensitive area. The readout electronics plus the acquisition system were attached to the PS-PMT coupled to the matrix of LYSO scintillation crystals. The LYSO block size of 52 mm in the Y direction is equal to the length of the PMT metal package from edge to bottom, so that the 2×2 block detectors can be closely placed in the axial direction to form a detection surface of $10.4cm \times 10.4cm$.

6.3.1 Matrix acceptance procedure

Two sets of matrices (Figure 6.2) were tested from the same manufacturer and these LYSO matrices were coupled to a reference multi anode PMT (Hamamatsu H8500C) with the same high voltage power supply.

Each matrix was irradiated with 511 keV γ-rays from a ^{22}Na source. 511 keV γ-rays were selected with a timing coincidence technique to eliminate the contribution of the 1.27 MeV γ-rays and the contribution of the ^{176}Lu decay (Figure 6.3). The four position signals (X_+, X_-, Y_+, Y_-) as obtained with the architecture,

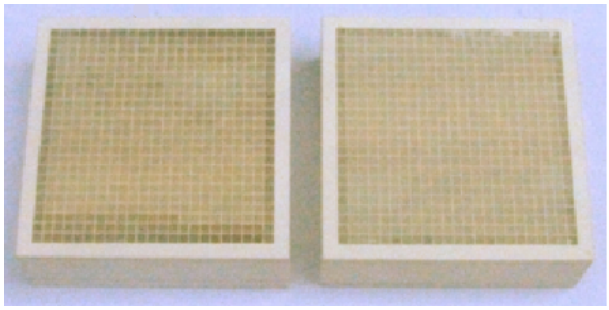

Figure 6.2: The two sets of LYSO matrix, which were under the test (Right one (the first set): old. Left one (the second set): new).

which was described in chapter 4 and a summed signal for energy and timing are produced on a front-end circuit board. These signals were fed to a position analyzer circuit through coaxial cables.

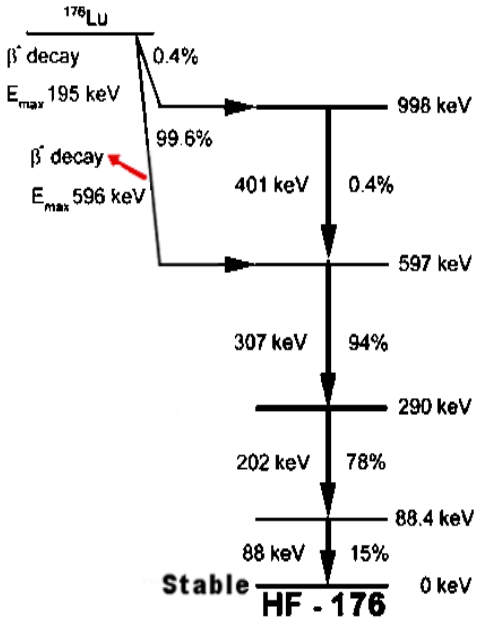

Figure 6.3: Decay scheme of ^{176}Lu into ^{176}HF by β^--emission.

The crystal coding was performed by a look-up-table on the basis of the center of gravity calculation method. The summed signal is used for timing pick-off and energy discrimination, where the energy discrimination is carried out through a look-up-table for each crystal [156, 157, 134].

The acquisition system had the capability to measure the energy spectrum of each pixel i of the matrix. The measured value (E_i) is proportional to the product of the light output of pixel i and the local Q_E of the PMT in the position of the pixel i (the energy window was set to [350-650 keV] for each module).

The relative light output of the new matrix with respect to the old matrix was obtained by dividing E_i (new) by E_i (old) and the average net reduction of the light output was 17%. In this way the factor variation

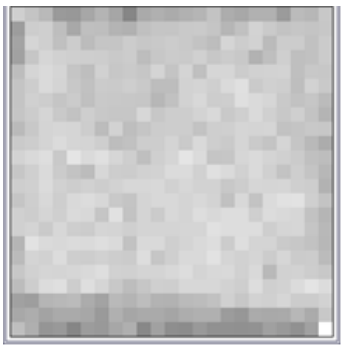

Figure 6.4: Light output measurement that was done for the new LYSO crystal matrix. This text image has achieved with the ImageJ program.

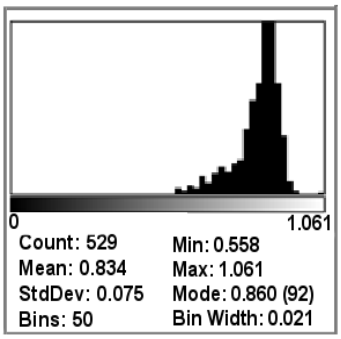

Figure 6.5: Histogram of light output measurement for the new LYSO crystal matrix.

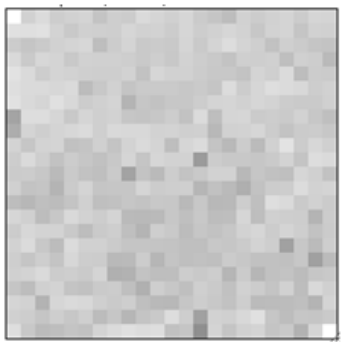

Figure 6.6: Light output measurement that was done for the first set of LYSO crystal matrix. This text image has been achieved by the ImageJ program.

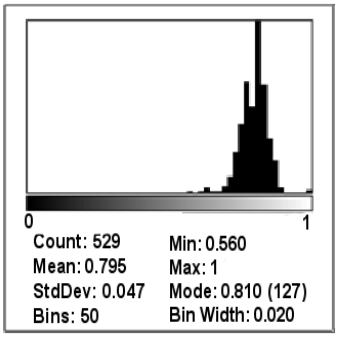

Figure 6.7: Histogram of light output measurement for the second set of LYSO crystal matrix.

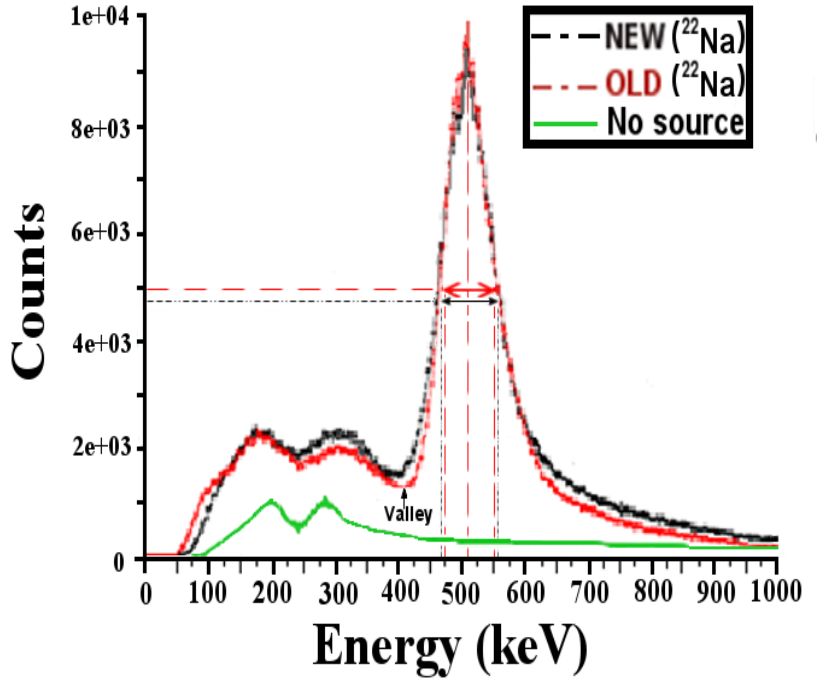

Figure 6.8: Energy resolution of the two matrices under the test (the new one is black and the old one is red).

due to the PMT photocatode non-uniformity was eliminated. The results are shown in Figure 6.4, Figure 6.5, Figure 6.6 and Figure 6.7.

In Figure 6.4 and Figure 6.6, the values of the relative light output are illustrated in gray-scale within the matrix. The histogram of the relative light outputs are shown in Figure 6.5 and Figure 6.7. The average value of relative light output was 0.834 for the old group and 0.795 for the new group. In this way a net reduction of about 4.7% was estimated. Moreover, the reduction was up to 50% for the older samples, as in the other new matrices the pixel light yields were in the range of 55% to 65%. Energy resolution of the two matrices were calculated after separately calibrating the energy output of each pixel and the results are shown in Figure 6.8. The corresponding energy resolution has been measured 19.8% for the new one while it was 18.9% for the old one. Flood field images have shown an average peak-to-valley ratio of 7.2, an average crystal pixel resolution of about 0.7 mm and an energy resolution of about 19%. As it has can be seen in Figure 6.8, the valley's energy threshold of the new one has fairly increased. The average energy resolution is 30% (FWHM) for the crystals in the center area, and 40% (FWHM) for those in the peripheral area. The matrices are acceptable if a performance resolution is observed.

6.4 Energy resolution

A series of tests with a ^{18}F-FDG source have been conducted in order to assess the proper function of position encoding logic and energy resolution. In order to obtain a flood map of each detector module a planar source of $5cm \times 5cm$ filled with ^{18}F-FDG has been interposed between two detector plates of one module each. The planar source was utilized in order to have an homogeneous activity, thus allowing to compare also pixels efficiency. The obtained flood maps have been reported in Figure 6.11 and Figure 6.12. Moreover, energy histograms are illustrated in Figure 6.10, with a cross section plot in which the pixel separation can be appreciated. As discussed in Section 5.1.2, pixels at the borders are badly separated because of the characteristics of the symmetric charge division network adopted in the front-end.

The acquisition and the analysis procedure are managed by the DoPET software. The analysis tools comprise the generation of the raw spectra of each position signal, the summation of signals, and the production of the map of events for each head. The planar images of the event distribution on the detector area are derived through a center of gravity coordinate algorithm. The possibility to select the raw ADC channel limits and to personalize the pedestal correction is foreseen. A dedicated program tool helps then the calibration of the system by performing the crystal pixels identification on the planar images, the construction of the LUT[1] and the energy calibration for the correction of the pixels gain variation. This procedure of the dedicated acquisition software of DoPET has been shown in Figure 6.10.

The energy histogram has been obtained by correcting each event by the efficiency of its own related pixel. The achieved energy resolution is 18% FWHM (with a minimum energy resolution of 15% per single pixel). These results are in agreement with measurements obtained in the previous published experiments with the DoPET scanner [137, 109]. Any improvements in this figure are related to the detector technology and front-end electronics, most notably the scintillating material and the Anger coding network.

The acquisition system reads out the 4 signals from each head, at a maximum count rate of 100 kHz for the whole scanner. The set-up being considered for this measurement is illustrated in Figure 6.9.

The modifications applied to the boards were according to a simulation, which was done by another member of our group. All of the components on the boards were checked and there was no shortcut in the circuits. By using the DoPET software (Figure 6.10) and our fast acquisition (Figure 6.9), flood field irradiation images were obtained. The results are illustrated in Figure 6.11, Figure 6.12.

[1] Look Up Table

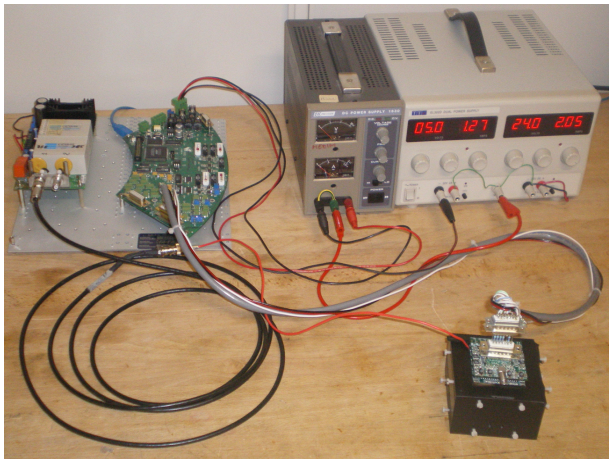

Figure 6.9: The Set up that has been applied for achieving 511 keV Flood Field irradiation (Light sharing scheme) for optimization of the PSPs (with the assistance of fast acquisition board).

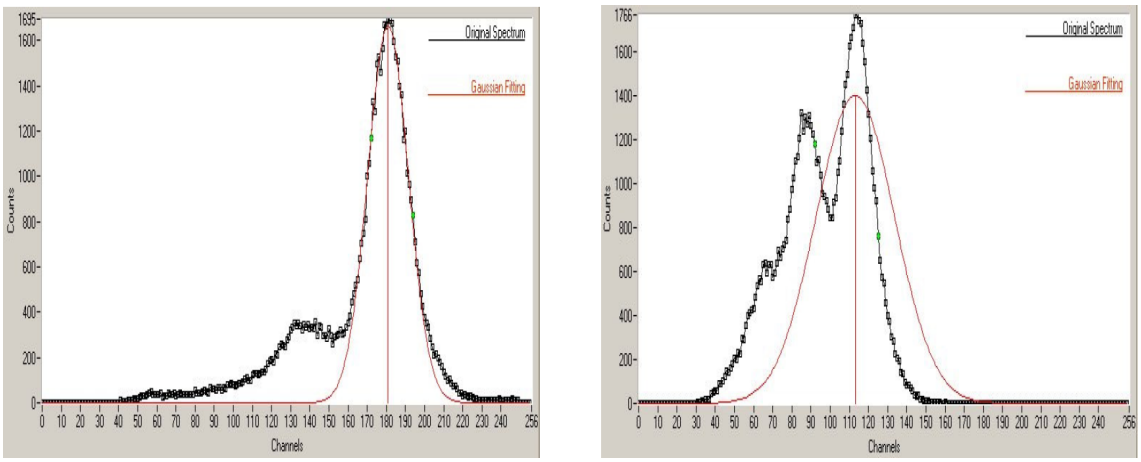

Figure 6.10: Single pixel spectra: central pixel with single photo-peak (left); edge pixel with multiple peaks (right).

In practice, one X and one Y coordinate are calculated for each annihilation photon that interacts in the block detector, where X_+, X_-, Y_+ and Y_- are the four PMT signals. The surface of a block detector is uniformly irradiated with 511 keV annihilation photons with the event locations histogrammed into a two-dimensional (2D) image based on the calculated X, Y locations.

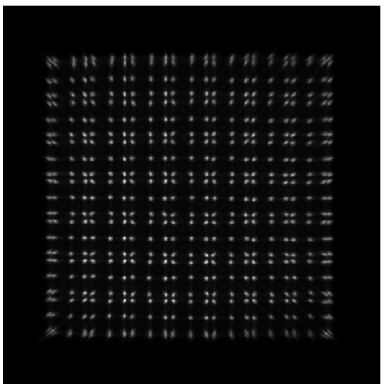

Figure 6.11: Flood image of head A, which was acquired for the LYSO matrix in PET mode (in present of ^{18}F source).

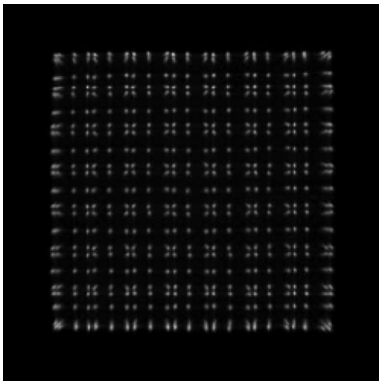

Figure 6.12: Flood image of head B, which was acquired for the LYSO matrix in PET mode (in present of ^{18}F source).

There were some spatial distortions in the array of spots, which are due to the fact that it is not possible to design the cuts so that the response is completely linear across the whole detector face. Therefore, a lookup table (LUT) is created from these flood histograms relating each calculated position X, Y to each of the 64 elements in the detector. It is also apparent that the spots are of a finite size and overlap to a certain degree. This is due to the statistical fluctuations in the PMT signals used to calculate X, Y, which in turn is caused by the limited number of scintillation photons produced and subsequently detected after a 511 keV annihilation photon interacts in the detector. These fluctuations ultimately limit the size and number of detector elements that can be decoded using four PMTs.

6.5 Time resolution

The timing measurement concentrates on the determination of the time when a γ particle interacts within the detectors, with a certain accuracy. At this stage for the optimization of the timing detection, the information on the energy associated with the event has a lesser priority or may even be disregarded [117, 118, 119]. On the other hand, a very good time resolution is needed (i.e., significantly higher than the shaping time or the collection time of the detector), and the time-walk error needs to be compensated for [116].

6.5.1 Timing jitter measurements for the temporal timing resolution

The jitter has an inversely proportional relation to the amplitude, just as the time-walk. The variation of the amplitude influences the way the jitter affects the time resolution. This has been shown in Eq. 3.2 (chapter 3), taking into account that the rising time of the signal remains constant, so its slope is reduced. In other words, low-amplitude signals generate considerably more uncertainty than high-amplitude signals do. As a result, the effect of jitter has to be tailored by the amplitude distribution [158, 119].

Because time resolution calls for noise-to-slope ratio optimization, while signal to noise ratio is the relevant figure for amplitude measurement, the simultaneous acquisition of the two quantities is often performed by splitting the signal after the preamplifier in two independent paths. In one of them, the information is

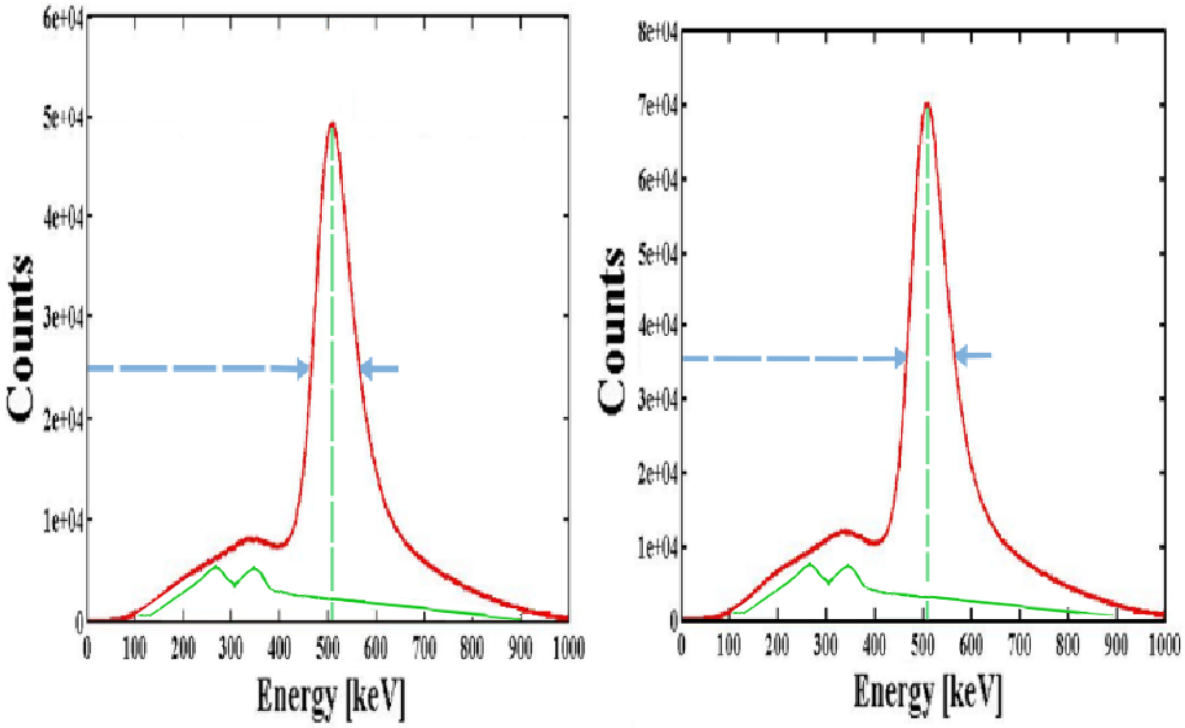

Figure 6.13: Detection heads energy spectra: the spectrum acquired for a flood field ^{68}Ge irradiation. A lower energy threshold of about 80 keV was applied during all the acquisitions to eliminate electronic noise. (left one and right one are related to head A and B, respectively.

processed by a fast shaper before being presented to the discriminator. As we have seen previously, in order to optimize the slope-to-noise ratio for timing measurement, the shaping time must be possibly matched to the detector collection time. In the other path, the preamplifier signal is fed to a shaper with a longer integration time, which can be chosen to be as long as allowed by the expected event rate or by the detector leakage current. The peak value can then be captured by a sample-and-hold and used for energy measurement as well as for time-walk correction [119, 116].

Figure 6.14, Figure 6.15, Figure 6.16 and Figure 6.17 illustrate the timing jitter measurements that were done to determine the threshold values for the walk and arm part of CFDs for doing the measurements of the temporal timing resolution. For having a better statistical estimation the value of 5 σ was considered. The value of walk threshold was calculated + 40 mV from $5\sigma_1 + 5\sigma_2$ (σ_1 and σ_2 are coming from Figure 6.14 and Figure 6.15). The value of arm threshold was calculated + 50 mV from $5\sigma_1 + 5\sigma_2$ (σ_1 and σ_2 are coming from Figure 6.16 and Figure 6.17). By applying the threshold values on CFDs, the time walk was reduced to a value of 200 ps.

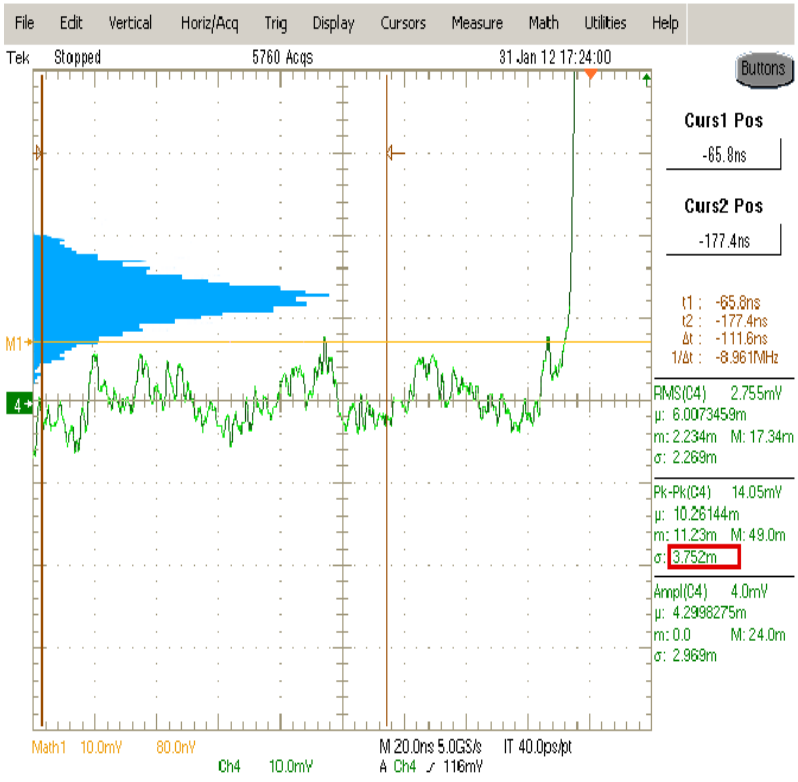

Figure 6.14: The measured jitter timing related to the delayed signal to estimate the threshold values that should be considered on the Walk part of the CFDs for the measurement of temporal time resolution (PMTs were powered by high voltage of 850 V).

6.5.2 The temporal timing resolution

The temporal timing resolution is a critical parameter for use in PET systems [159]. Setting a narrow timing window allows good timing resolution but reduces detectors sensitivity. Assessment of two head

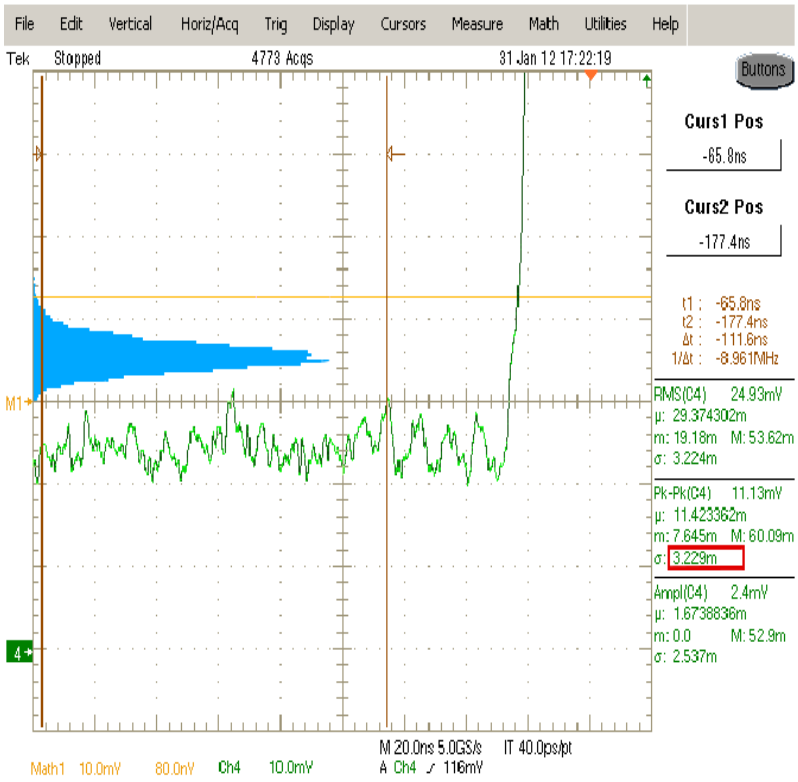

Figure 6.15: The measured jitter timing related to the attenuated signal to estimate the threshold values that should be considered on the Walk part of the CFDs for the measurement of temporal time resolution (PMTs were powered by high voltage of 850 V).

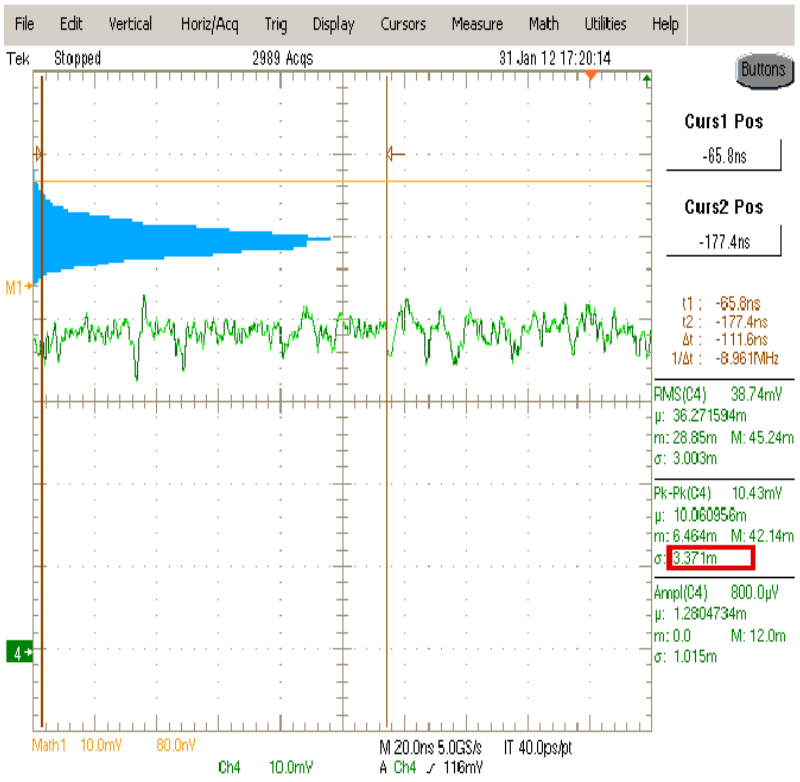

Figure 6.16: The measured jitter timing related to the input signals of comparator (related to Arm signal) to estimate the threshold values that should be considered on the Arm part of the CFDs for the measurement of temporal time resolution (PMTs were powered by high voltage of 850 V).

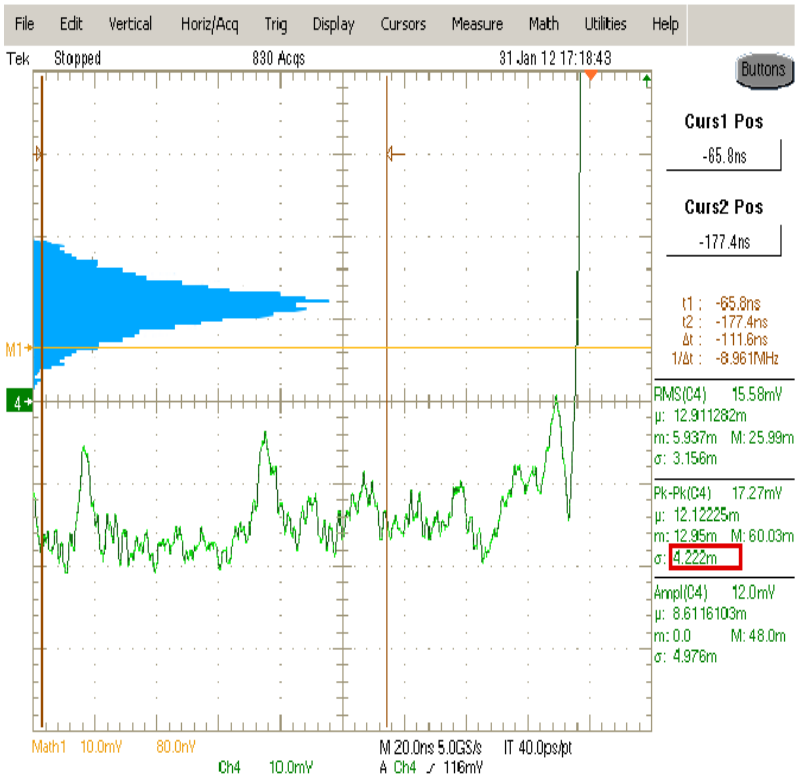

Figure 6.17: The measured jitter timing related to the input signals of comparator (related to Arm signal) to estimate the threshold values that should be considered on the Arm part of the CFDs for the measurement of temporal time resolution (PMTs were powered by high voltage of 850 V).

of detectors in timing, for coincidence detection was investigated. The temporal timing resolution was measured using the instrumentations setup in Figure 6.18.

6.5.2.1 The Experimental setup

In this measurement, two planar heads of $10.4cm \times 10.4cm$ were mounted in front of each other. However, the total active area of each crystal is $46mm \times 46mm$. Each head contains detector modules, which are tightly assembled and optically coupled to the scintillator crystals. Each scintillator is a LYSO matrix of 23×23 pixels $1.9mm \times 1.9mm \times 16.0mm$, with a 2.0 mm pitch. The operating voltage was 850 V and the experiment was operated at room temperature.

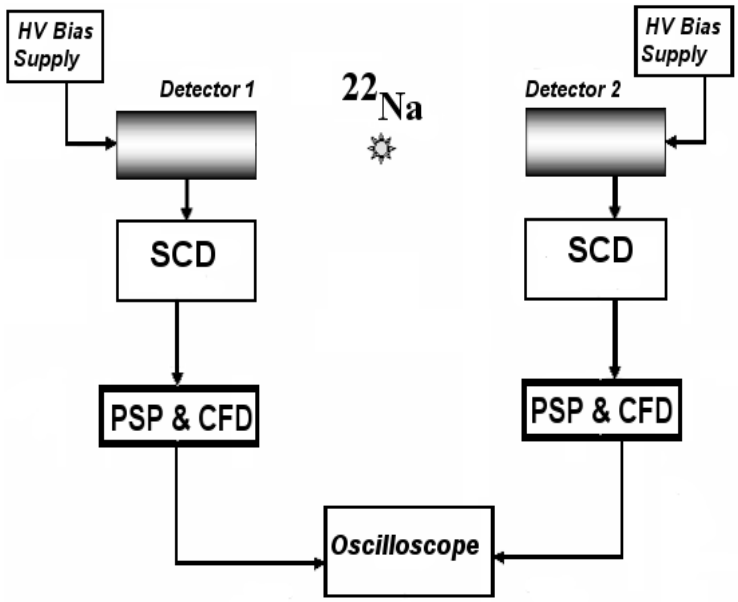

Figure 6.18: Block diagram of the electronic chain for the measurement of temporal timing resolution.

The PMT's anode is connected directly to the input of the constant fraction discriminator. The anode signals from fast PMT contained a wide range of amplitudes, but they had a relatively narrow range of rise times and pulse widths. The signal rise-time was measured with a digital phosphor oscilloscope (Tektronix TDS 5054) with bandwidth of 500 MHz and sampling rate of 5 Gs/s (which is required for measuring nanosecond or sub-nanosecond time resolution).

Initially, the output signal from each detector is taken as two channels representing the slow channel (energy channel) and the fast channel (timing channel). The energy signal was shaped and passed through a timing single-channel analyzer and gated by a delay generator, while the timing signal was delayed by a fixed delay. Then both signals were recorded using a digital oscilloscope, which was triggered in a qualified mode incorporating level crossings of both signals, effectively acting as a coincidence gate to make sure they are in coincidence and passed to the MCA to accept the 511 keV peak only [160].

The coincidence timing resolution (FWHM) was measured at different detector distances and the curves fitted with a Gaussian. The coincidence timing resolution varies with source-to-detector distance. The

measurements showed that the value FWHM does not change very much when source-to-detector distance increases from a value of 5 cm to 10 cm.

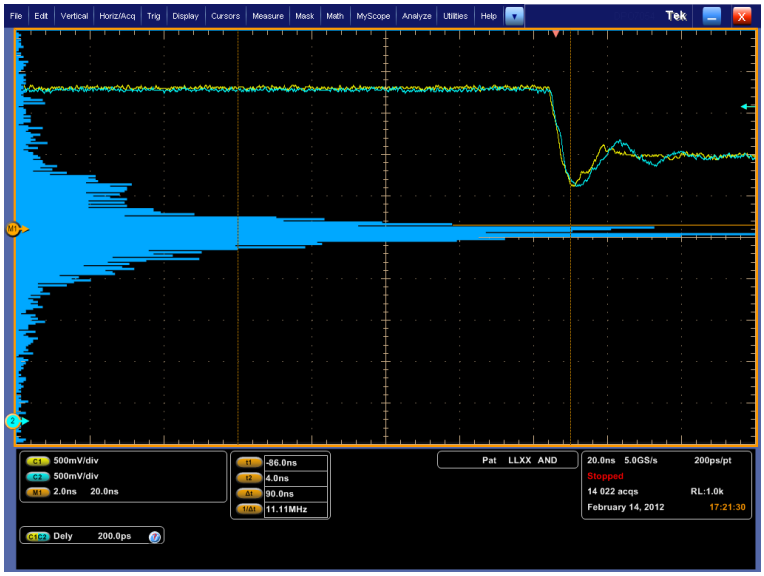

Figure 6.19: The distribution of delay between the digital output pulses coming from 2 detection modules in 2 heads of DoPET due to the applied threshold level in CFDs for eliminating time walk effect to measure temporal timing resolution with a good accuracy.

With the measuring temporal timing resolution for 511 keV annihilation γ-rays irradiating a pair of scintillation DoPET detectors, the values of 1.40 ns in the case of 10 cm detectors apart and 1.43 ns in the case of 5 cm detectors apart were acquired for half of FWHM. These values were calculated FWHM the Gaussian fits, applied to the experimental data. A large dynamic range of input pulse amplitudes into the CFD leads to problems in setting of the walk adjustment on the CFD module. Hence, in our experiment, an appreciable dynamic range of signal amplitudes (from 0 mV to -100 mV) into the CFDs was used for DoPET detectors. The threshold on CFDs was set as low as possible above the initial knee of the signal, but sufficiently higher than the noise level. For a 100:1 dynamic range, the CFDs have been presented $\pm$ 150 ps walk and jitter below 300 ps. This setting gave us a certain degree of immunity to pulse-shape variations, since very large variations in the rising time of the signal are needed to produce significant time error. The bipolar signal, which was achieved from CFD was quite symmetrical, and with a weak initial displacement from the baseline, before the zero-crossing point, still made it possible for the zero-crossing precisely (Figure 6.19, 6.20, 6.21, and 6.22). By the correct threshold setting, the offset voltage between the input nodes of the comparator did not appear and the achieved distribution of temporal timing resolution was symmetric. The σ had a value of 0.56 ns and the FWHM was $\approx$ 1.2 ns (and the measured time jitter was about 300 ps). With a threshold level of + 60 mV to accept PMT pulses, a resolution of 50 ps FWHM was measured. However, 20 ps (FWHM) was the intrinsic resolution of the utilized oscilloscope.

The attenuation factor (F), which was considered for our measurement was 17%. Theoretically, a smaller value is desirable for F, but, the acceptable factor depends on the count rate and the values could be in the region of 10% to 20% for achieving minimum time [145].

Due to the results obtained the main sources for the time walk errors in the timing measurements are:

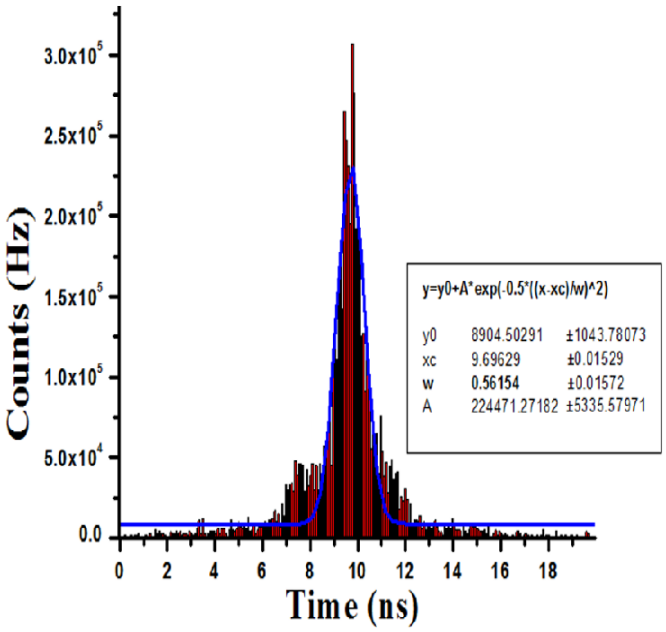

Figure 6.20: The temporal time resolution result, which was acquired from data on oscilloscope. In this measurement, the distance between two head of DoPET was set 5 cm. A Gaussian function has been used to do the fitting curve to acquired data.

Figure 6.21: The distribution of delay between the digital output pulses coming from 2 detection modules in 2 heads of DoPET due to the applied threshold level in CFDs for eliminating time walk effect to measure temporal timing resolution with a good accuracy.

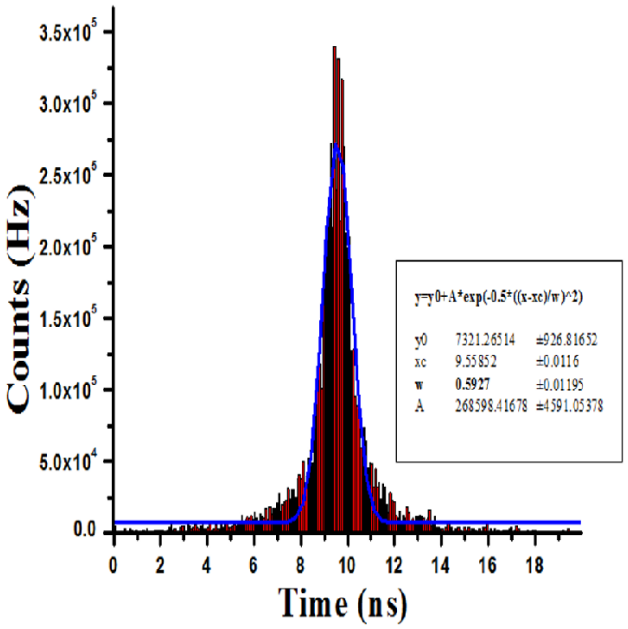

Figure 6.22: The temporal time resolution result, which was acquired from data on oscilloscope. In this measurement, the distance between two head of DoPET was set 10 cm. A Gaussian function has been used to do the fitting curve to acquired data.

1. The limited gain-bandwidth product of the comparator.
2. Offset voltage between the input nodes of the comparator.
3. Crosstalk between the input node of the comparator and some other parts in the circuit.

Therefore, employing the high gain-bandwidth product comparator and decreasing the offset voltage, which is caused by the limited speed of the comparator, could be beneficial for obtaining small time walk errors. In addition, reducing the crosstalk in the circuit by carefully designing of the circuit prevents effectively time walk error [145].

6.5.3 Dead time measurements of the constant fraction discriminators

The dead time behavior of the detector sub-system is considered as a substantial paralyzing component, because every time a photon interacts with the crystal, more energy is deposited, and light must be completely emitted before the detector can process the next event.

The count rate losses of events are calculated according to the system dead time. These losses occur at the coincidence detector and the data acquisition system. The front-module consists of a LYSO scintillator, a position sensitive photomultiplier (PS-PMT), a resistive readout, a set of ADCs, running at a fixed frequency, and a FPGA that processes and encapsulates the detected events. Pulse detection is done in the digital domain, with all processing algorithms implemented in a single FPGA. The detected pulses are sent to an external host through a fast Ethernet connection for off-line coincidence detection, image reconstruction and data storage.

To measure the dead time behavior for the DoPET scanner as a function of count-rate, a “decaying source” method was performed. A uniform source containing a known quantity of a short-lived positron emitter such as ^{18}F-FDG (with approximately 2 mCi activity) was placed in the field of view of the two

detector modules of the PET scanner. As the activity in the field of view decays, the unsorted single count rates were measured. The acquisition time was 30 minutes at a distance of 20 cm between the modules. Then every time observed count rate (Ro) was recorded. The relationship between observed counting rate (Ro), the source activity and true counting rate is determined under different conditions (chapter 3). Regarding to paralyzable dead time model, which is considered for CFDs, fitting curves have been applied (Eq. 3.14 and Eq. 3.15). Table 6.2 illustrates The brief results of the calculated dead time for the four modules of CFD. It is obvious that at low count rate there is negligible dead time loss or pulse-pile up, and straight lines are used to obtain the best fit.

Table 6.2: Dead time measurements of the constant fraction discriminators

Detector module	Dead time (ns)
A1	247 ns $\pm$ 9.37 ps
A2	227 ns $\pm$ 5.37 ps
B1	210 ns $\pm$ 4.7 ps
B2	207 ns $\pm$ 5.34 ps

Reducing CFD dead time by fine-tuning of comparators thresholds and dynode pulse amplification is not expected to change considerably these values. Thus, technological changes, such as replacing the pulse discriminating technique, were applied in the new version of CFD board. Adopting the modular approach, the total detector dead time was reduced by a maximum factor of 1.3.

The obtained results suggest that the true counting rate (input count rate) could be predicted from the observed counting rate of the system by the measuring the system dead time by $R_{max} = (e\tau)^{-1}$ from the maximum observable counting rate. Then N (input or true count rate) is determined from R (observed count rate) by applying the following formula ($R = N\exp^{-NT}$), in agreement with the paralyzable model [161].

6.5.4 Dead time measurements of the acquisition system

The dead time behavior of the coincidence processing sub-system is essentially non-paralyzing, because events arriving while a coincidence is being processed are simply ignored. Table 6.3 illustrates the results.

Table 6.3: Dead time measurement of the PET acquisition system

Detector Configuration	Dead time (ns)
A1 and A2 modules VS. B1 and B2 modules	1007 ns $\pm$ 5 ns

The same setup as described in section 6.3.4 was applied for this measurement. The dead time of the acquisition system is calculated according to the number of input coincidences, obtained by counting input CFD triggers with the internal statistics counters, and the number of coincidence actually recorded. The formula which is applied to to obtain this non-paralyzable dead time is Eq. 3.14 in Section 3.10.3.2.

According to Eq. 5.3, the expected dead time reduction for n = 2 (2 modules) is f = 1.33. The obtained dead time in this experiment is very close to the dead time, which was reported in for a single DAQ board [150, 151]. Considering this part of the system as a non-paralyzable instrument, the resolving time is calculated by applying $N = R/(1-RT)$. The observed counting rate continues to increase and by increasing the

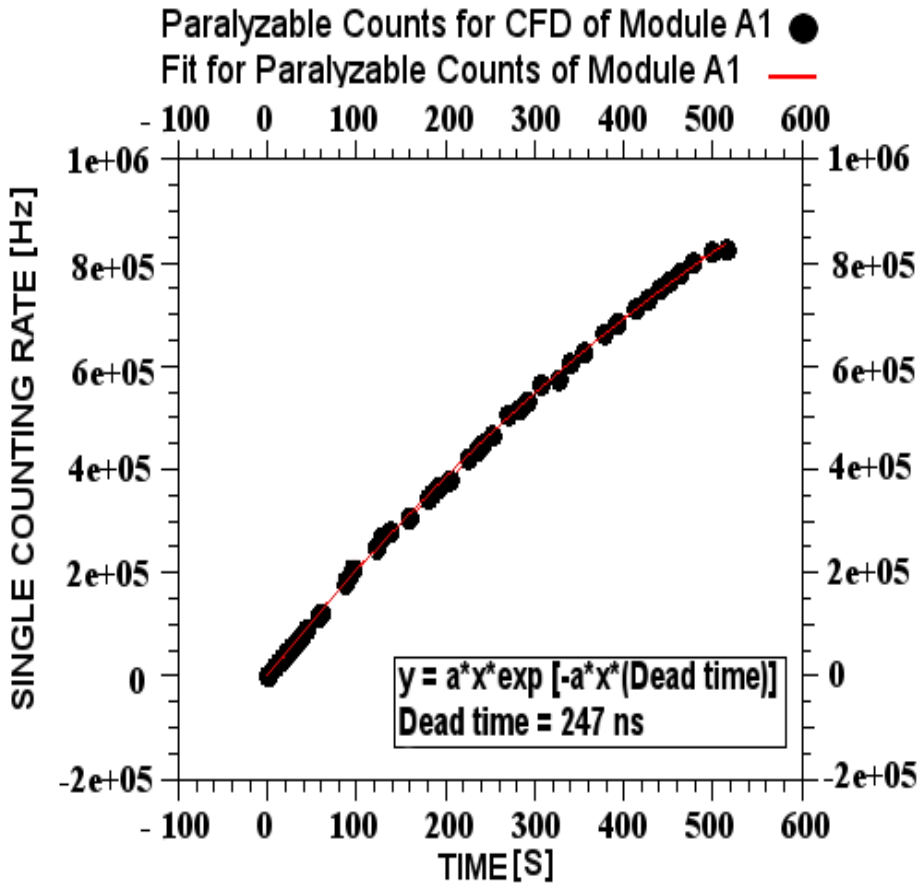

Figure 6.23: A "decaying source" (^{18}F-FDG as a uniform positron emitter source short-lived) experiment was performed in order to measure the dead-time performance of our PET scanner as a function of count-rate. Data and fitted curve for the experiment of dead time (paralyzable model) with ^{18}F-FDG source. The data is composed of the recorded single counts from the detector module (A1) versus the decay time of activity of the source.

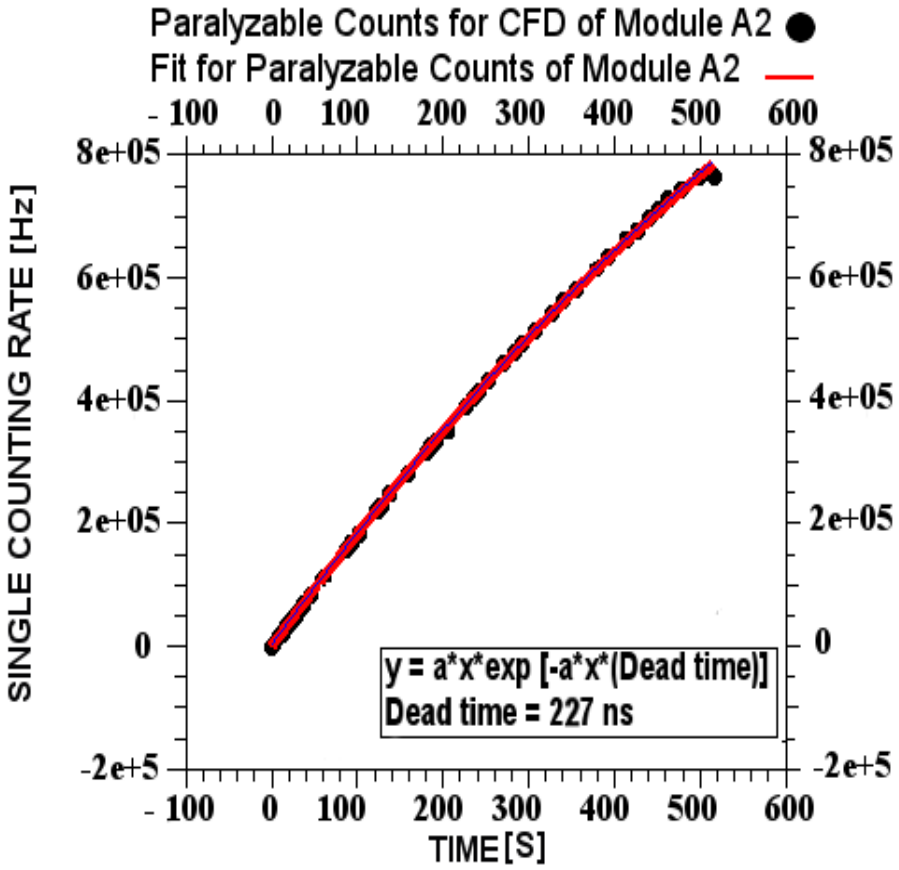

Figure 6.24: Data and fitted curve for the experiment of dead time (paralyzable model) with ^{18}F-FDG source. The data is composed of the recorded single counts from the detector module (A2) versus the decay time of activity of the source.

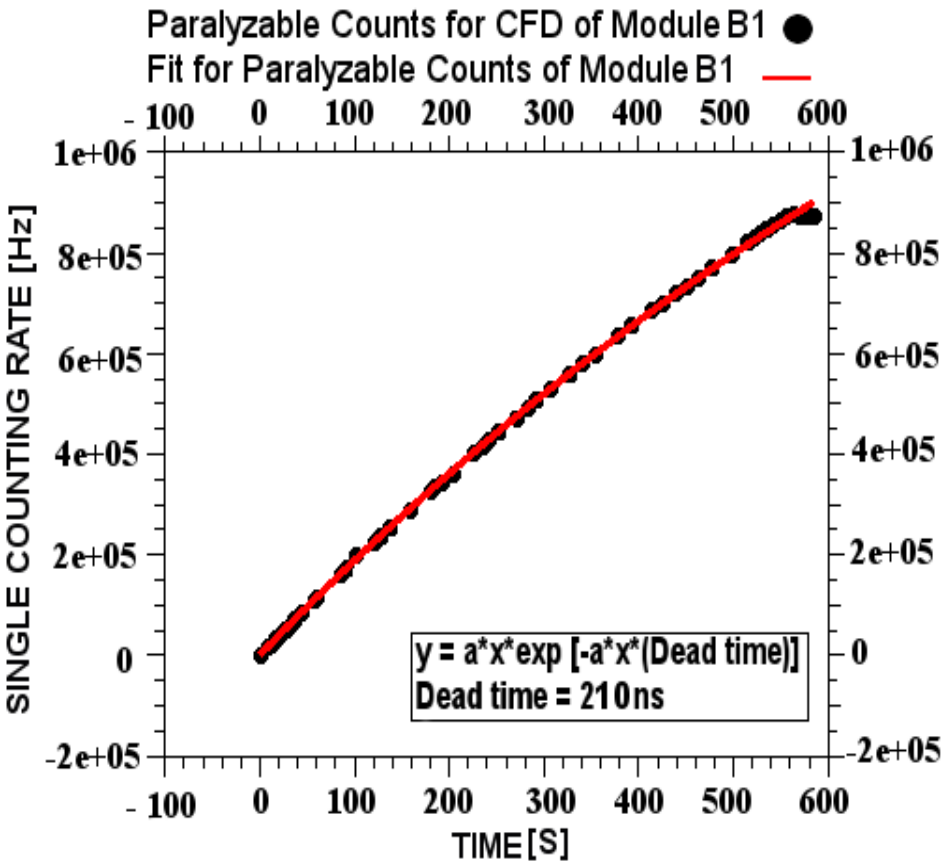

Figure 6.25: Data and fitted curve for the experiment of dead time (paralyzable model) with ^{18}F-FDG source. The data is composed of the recorded single counts from the detector module (B1) versus the decay time of activity of the source.

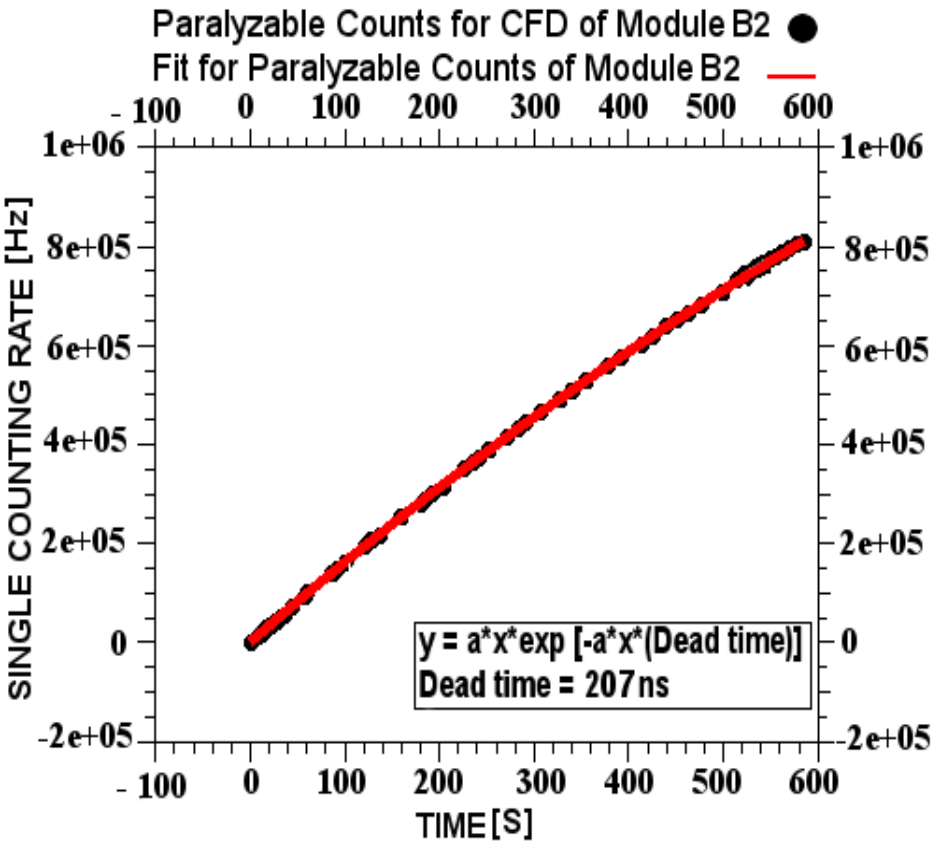

Figure 6.26: Data and fitted curve for the experiment of dead time (paralyzable model) with ^{18}F-FDG source. The data is composed of the recorded single counts from the detector module (B2) versus the decay time of activity of the source.

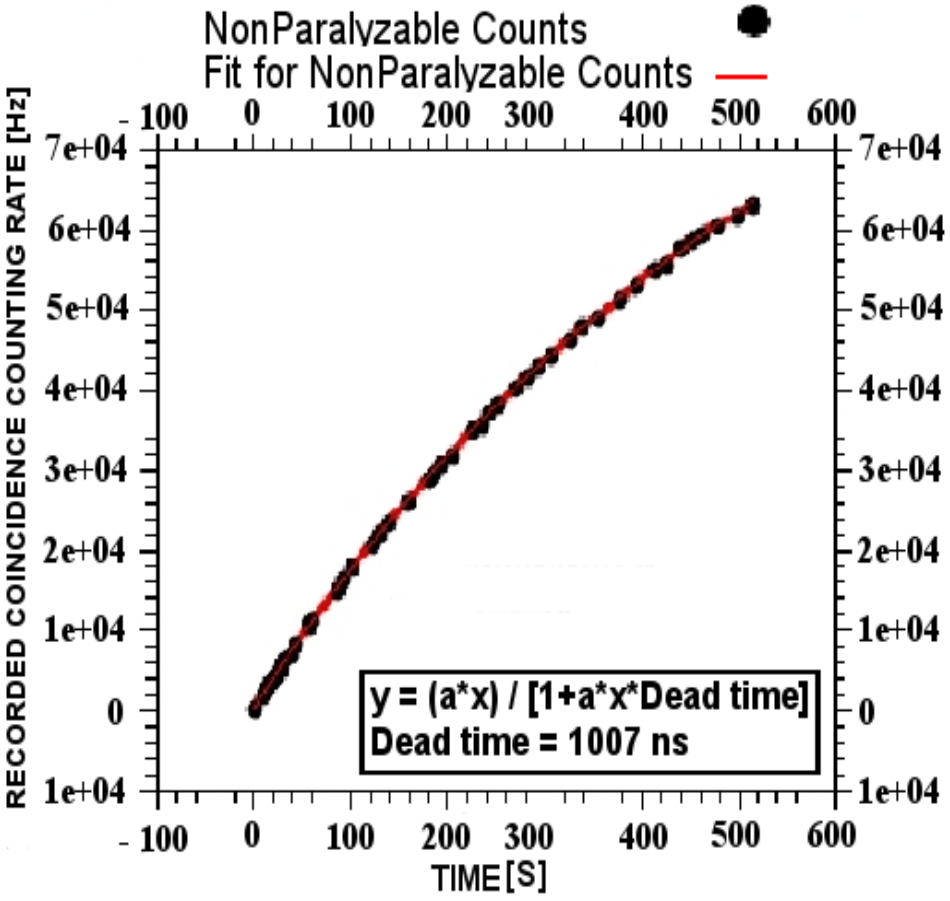

Figure 6.27: Data and fitted curve for the experiment of dead time (nonparalyzable model) with ^{18}F-FDG source. The data is composed the recorded coincidence counts versus the decay time of activity of the source.

true counting rate, approaching asymptotically a maximum of value of R_{max} equal to $1/T$ when N (input or true counting rate) is in finitely great [161].

6.6 DoPET calibration process

The result of a complete PET/SPECT acquisition is a calibration, a statistics and a list-mode events file. In order to obtain the planograms required by the reconstruction algorithm, there must be a series of data analysis on the files.

The first step is the pedestal calculation. This operation is done by the host application, which takes as input the calibration file and outputs a XML[1] pedestals file. Pedestal values for each ADC channels are necessary to decode Anger signals into module spatial coordinates. This is because it is necessary to remove the baseline in order to maintain the linear relationship between the four Anger coordinates converted by the DAQ board.

Pedestal information per channel must be flexible for the modular geometry. The effect of a wrong pedestal restoration leads to crystal identification errors, which has been shown in Figure 6.28 (the flood map).

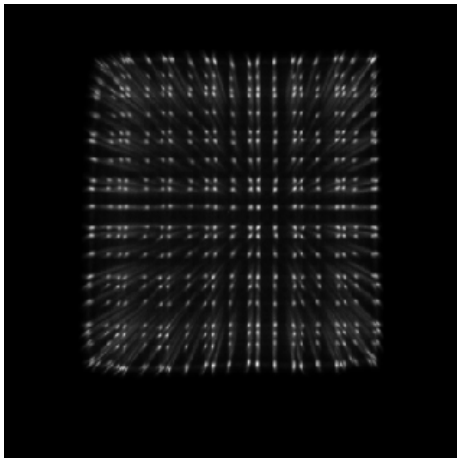

Figure 6.28: The effect of a wrong pedestal restoration on the flood map.

Once the pedestal value has been calculated, the event hit coordinates within the detector module can be decoded from the four Anger signals (X_-,X_+,Y_+ and Y_-). To reconstruct PET images with pixellated scintillators, acquired events should be grouped into 2-dimensional bins that correspond to crystal elements. In order to identify pixel location of individual pixels, a preliminary calibration PET acquisition must be done with a planar source. From this acquisition a flood map is generated. Figure 6.29 and Figure 6.30 illustrate the achieved flood map from the experiments. The map is then segmented with a semi-automatic process, that is based on image centroids detection and watershed algorithms. The result of map segmentation is shown in Figure 6.31.

Figure 6.30 illustrates that individual LYSO crystals are well resolved at 511 keV, and identifiable, separately. The apparent widths of each crystal (2.0 mm) and the high peak-to valley ratios evident in the profiles (at 511 keV) shown in Figure 6.30, suggest that individual crystals can be identified with high

[1]Extended Markup Language

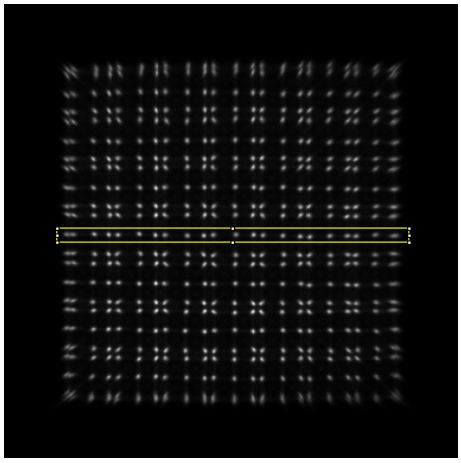

Figure 6.29: The acquired 511 keV flood field image, in the final detector configuration: 23×23 LYSO scintillating crystals, 2.0 mm pitch. The flood map is acquired with a correct pedestal restoration.

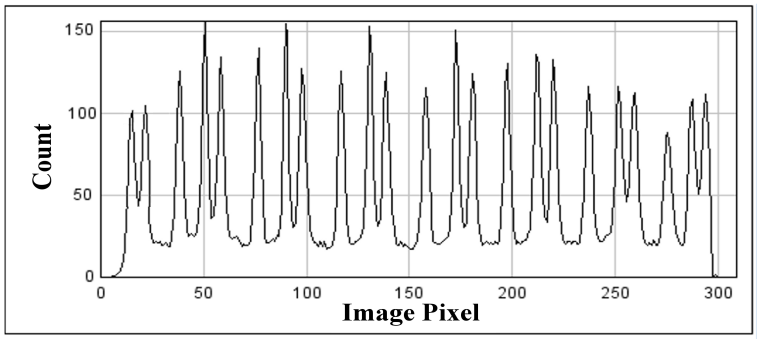

Figure 6.30: Plot of the horizontal section of a pixel row (for LYSO crystals of matrix of 23×23 pixels $1.9mm \times 1.9mm \times 16.0mm$, with a 2.0 mm). The map has been obtained with roughly 40 million events in a 400×400 pixels image, acquired from a ^{22}Na source during 40 minutes.

contrast. The identified individual crystals implies that the combination of LYSO, direct crystal-PSPMT itself, is an efficient mechanism for locating absorption events within the scintillator array. In Figure 6.30, the rather high background is mostly due to electronic noise.

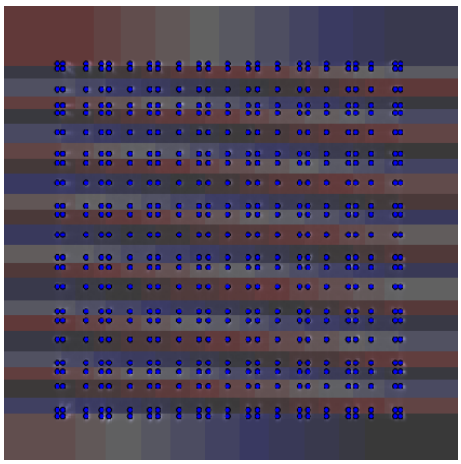

Figure 6.31: The Segmented flood map, which has been acquired for the 23 × 23 LYSO crystal array.

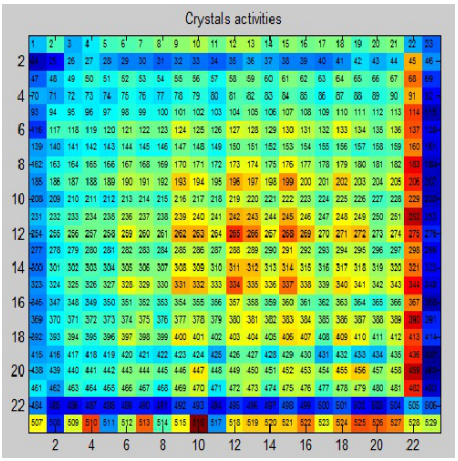

Figure 6.32: The Re-binned flood map of the 23 × 23 LYSO crystal array.

The segmented flood map is then used as look-up table to rebin acquired events (Figure 6.32). The pixel map has no direct correlation with image reconstruction, apart from its use for the generation of a pixel look-up table, and for this reason it is not stored in the hard disk.

6.7 The Energy correction

The energy correction is a process of transforming acquired values to energy-related values and it is applied to discard low-energy events that suffered scattering or those that are not product of a positron annihilation. The typical applied energy windows are at [350-700 keV]. A wider energy window, generally

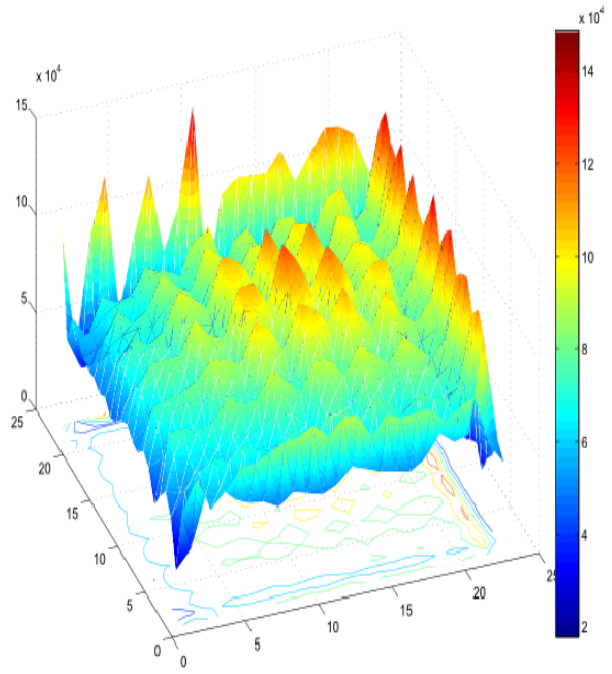

Figure 6.33: The image shows that because of higher encoding noise the pixel identification at borders does not work nicely.

can improve sensitivity, while narrower windows improves spatial resolution of the DoPET system. For this reason the energy window is left as a degree of freedom to be tuned during image reconstruction.

The filtering of events depends on their energy, the raw ADC output range must be referred to the real energy range of acquired photons. The resulting Anger voltages can change slightly between different crystal pixels for any deposited energy. Hence, it is crucial to set up the conversion factor on a pixel base. This conversion factor is named "pixel efficiency χ" by us and the conversion is expressed like:

$$E_i = E_{ADC} \cdots \chi(i) \tag{6.1}$$

where i is the index of the interested pixel element, E_i is the energy in keV and E_{ADC} is the integer ADC output. Calculating pixel efficiencies is a process, which is composed of two steps. The first step consists in deriving energy histograms on each pixel i, the second is a Gaussian fitting by which we identify the ADC channel k(i) corresponding to the 511 keV peak. The pixel efficiency is

$$\chi(i) = \frac{511}{k(i)}\,[keV] \tag{6.2}$$

In order to determine the global energy histogram and resolution by summing energies of all acquired events, it is necessary that the pixel efficiency be calculated. Figure 6.34 and Figure 6.35 illustrate the raw and converted energy histograms for a pixel at the center of the flood map, respectively. A long tail in the acquired histogram could be explained as an effect of the optical absorption on the scintillating crystal [162].

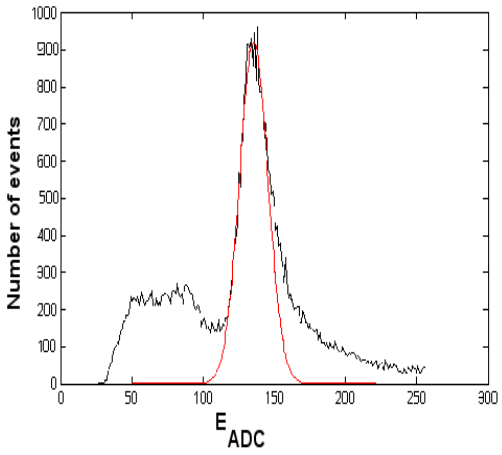

Figure 6.34: ADC channels histogram of a pixel element for a FDG source. The long tail is an effect of the optical absorption in the scintillator.

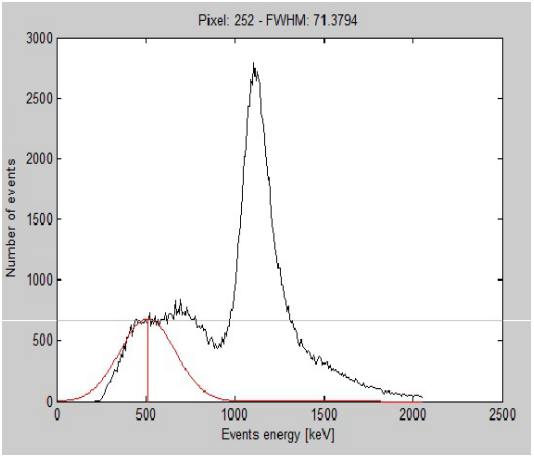

Figure 6.35: Energy histogram of a pixel element for a FDG source. The abscissa conversion has been done by dividing the ADC channels by the value of the channel under the peak mean μ and multiplying by 511 keV.

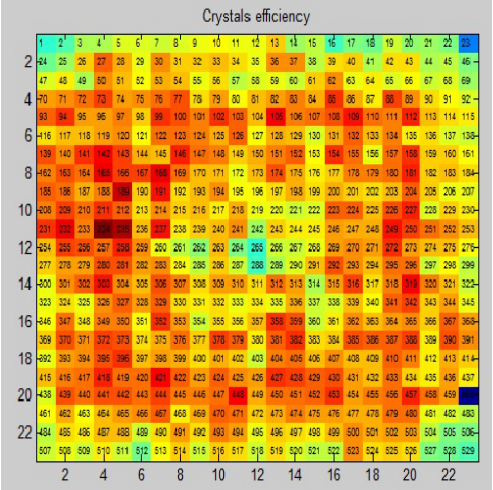

Figure 6.36: The crystal efficiency of a detector module.

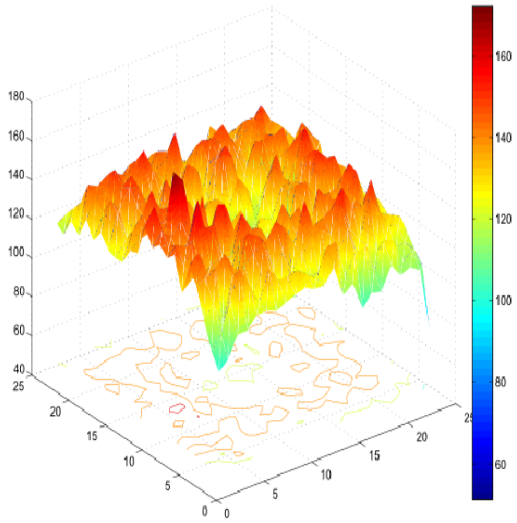

Figure 6.37: Pixel efficiency map of a detector module.

6.7.1 The coincidence timing resolution: By applying a wire

The coincidence timing resolution is a critical parameter in the PET system (DoPET) [159]. Good timing resolution permits a narrow timing window to be set and, therefore, true coincidence events could be well distinguished from the random coincidence events which cause degradation in image quality, because they reduce sensitivity. The vital requirements for the coincidence technique are detectors with good efficiency, high energy resolution and good coincidence timing resolution.

6.7.1.1 The Experimental setup

In this measurement, assessment of the timing for coincidence detection was investigated. Two planar heads of $10.4cm \times 10.4cm$ were mounted in front of each other. However, the total active area of each crystal is $46mm \times 46mm$. Each head contains detector modules, which are tightly assembled and optically coupled to the scintillator crystals. Each scintillator is a LYSO matrix of 23×23 pixels $1.9mm \times 1.9mm \times 16.0mm$, with a 2.0 mm pitch. The operating voltage was 850 V and the experiment was operated at room temperature. The coincidence timing resolution was measured using the instrumentations setup in Figure 6.38.

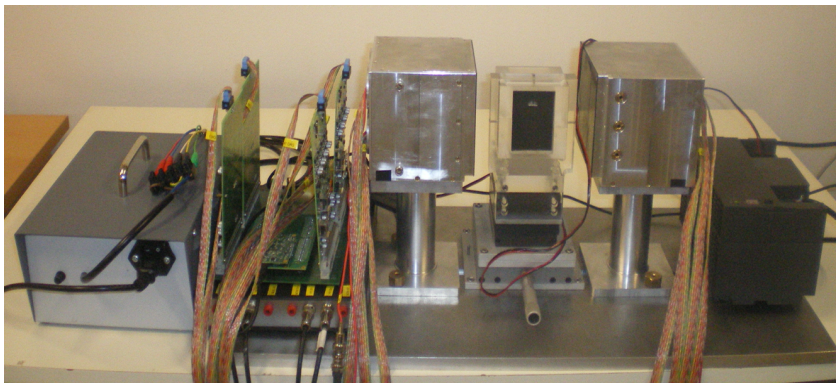

Figure 6.38: The set-up that was used to measure the coincidence timing resolution.

The acquisition data software of DoPET records coincidence, single and multi-coincidence events. A ^{18}F-FDG source (with activity of 2 mCi) was located in the middle distance of two head of DoPET. Two different coincidence window widths with values of 5 ns and 10 ns are set. The FPGA Stratix III (Altera Corp., San Jose, CA, U.S.A) on the mainboard determines if the two edges from the RTGA_2 and RTGB_2 are within a certain time window or not, and if they are close enough, it is recognized as a coincidence event. Due to the symmetrical situation for the two head of detection, a wire could be either inserted on the input pin of digital signal from the B side of detection module (which is presented on the motherboard as a name of RTGB_2) or on the input pin of digital signal from the B side (which is presented on the motherboard as a name of RTGA_2). In this way all coincidence events were recorded for each possible combination detection modules in each head of DoPET. The delay line was reduced (by cutting a piece of wire) after the first time that coincidence events were recorded. This procedure was followed till the time that recorded coincidence events tended to zero.

A little difference between recorded coincidence events was observed. It was thought that maybe it happened to the fact that events were very close to each other and they were not accepted as a coincidence but instead they caused a pile up (due to the observed fluctuation in recorded events). However, the delay between the two signals from RTGA and RTGB also were checked and no external delay was detected. The delay of histograms was of the order of $\bar{\mu} \cong 200$ ps (when $\bar{\mu}$ is the mean value) is a good prediction for the trend of curve that we are looking for.

6.7.1.2 Measurement of coincidence timing resolution by firmware of 5 ns

Figure 6.39 illustrates the first measurement that was done with the firmware of 5 ns. In this case, $\sigma \simeq$ 3.05 ns $\pm$22 ps (standard deviation) was measured (the observed uncertainty with an order of 22 ps can be related to the time delay). Due to the relationship between FWHM and standard deviation, it was calculated that the FWHM of the coincidence time resolution had a value of $\simeq$ 7.18 ns (Figure 6.38).

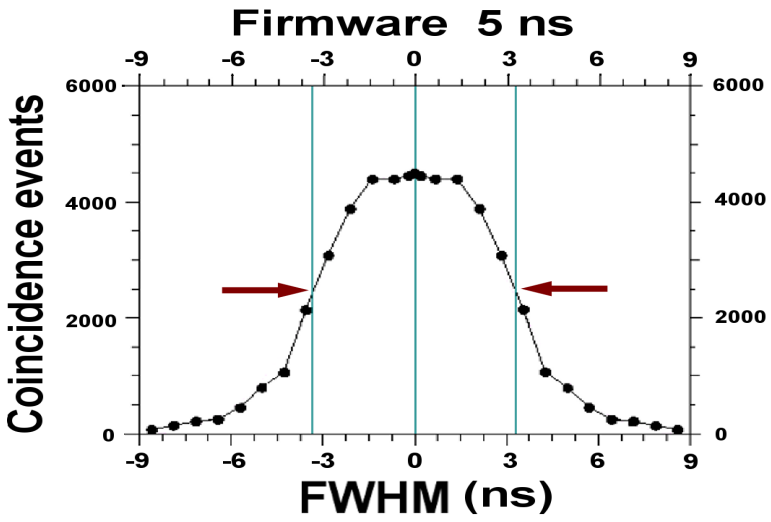

Figure 6.39: Measurement of coincidence timing resolution for the Firmware of 5 ns (with different delay times, which is applied by a wire).

One of the origins of the peak width could be statistical fluctuation in the number of charge carriers, which is produced by radiation interaction. If this process be followed a Poisson distribution, the standard deviation is the square root of the number of charge carriers. If probability associated with σ is considered to 99%, significant coincidence events are recorded but, instead the accuracy for estimating the window width of coincidence is reduced.

6.7.1.3 Measurement of coincidence timing resolution by firmware of 10 ns

Figure 6.40 illustrates the second measurement that was done with the firmware of 5 ns. In this case, σ $\simeq$ 4.4 ns $\pm$10 ps (standard deviation) was measured (the observed uncertainty with an order of 10 ps can be related to the time delay). Due to the relationship between FWHM and standard deviation, it was calculated that the FWHM of the coincidence time resolution had a value of $\simeq$ 10.362 ns (Figure 6.40).

The obtained results show that the firmware of 10 ns is a better choice for measuring of coincidence timing resolution with respect to the firmware of 5 ns.

6.7.2 The coincidence timing resolution: By applying a coaxial cable

In this measurement instead of a wire as a delay line, a coaxial cable was utilized. Moreover, a ^{22}Na source was used to have a better statistics of recorded coincidence events. Figure 6.40, illustrates the result of the measurement. By employing a coaxial cable, no reflection was observed. In Figure 6.40, there is a signal deformation from a square shape, which causes a net deterioration for the coincidence timing

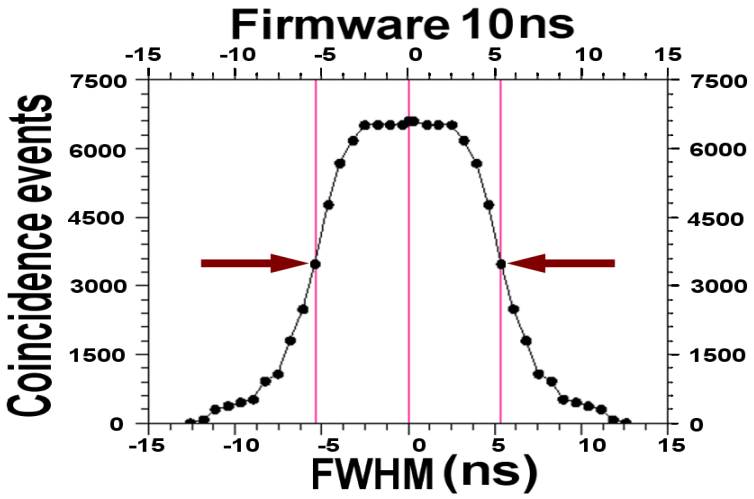

Figure 6.40: Measurement of coincidence timing resolution for the Firmware of 10 ns (with different delay times, which is applied by a wire).

resolution measurement. In this experiments, the shape of coincidence timing resolution was quite close to the expected one. By using a coaxial cable, a better transmission of high frequencies is achievable. Due to the relationship between FWHM and standard deviation, it was calculated that the FWHM of the coincidence time resolution had a value of $\simeq$ 10.362 ns (Figure 6.40).

In this measurement, $\sigma \simeq 2.55$ ns ± 15 ps (standard deviation) was measured the observed uncertainty with an order of 15 ps can be related to the time delay. The FWHM of the coincidence time resolution had a value of $\simeq$ 6.005 ns. The achieved results shows a better accuracy for measuring the coincidence time resolution with respect to the one that was done with wire and a value of 7 ns was gotten. The measurements present that when the coincidence window is considered 10 ns, there is only 3.62% difference between the measured data and firmware data, however, in the case of coincidence window of 5 ns is about 20%.

6.8 Efficiency

The geometric efficiency of the PET scanner is defined by the solid angle projected by the source of activity at the detector. In the other words, the geometrical efficiency is the ratio of the number of γ-rays reaching the detector to the number of γ-rays started from the source. It can be calculated by:

$$\Omega = \frac{R^2}{4d^2} \tag{6.3}$$

Where R is the radius of the detector surface facing the sample and d is the source-detector distance. However, the shape of our detector is rectangular, a point source of ^{22}Na was placed at a distance R from the detector head. Figure 6.42 illustrates the solid angle viewed by the source and shows how the geometric factor, depends on the distance between the source and the detector. The geometric efficiency decreases with increasing source-to-detector distance in accordance with the inverse square law (Where d is the size of the detector, d = 5 cm, and R = 10 cm). Figure 6.42 shows that the solid angle is subtended by two same-sized opposing detector elements (16 mm thickness of LYSO crystal).The thicker scintillator and higher count rate

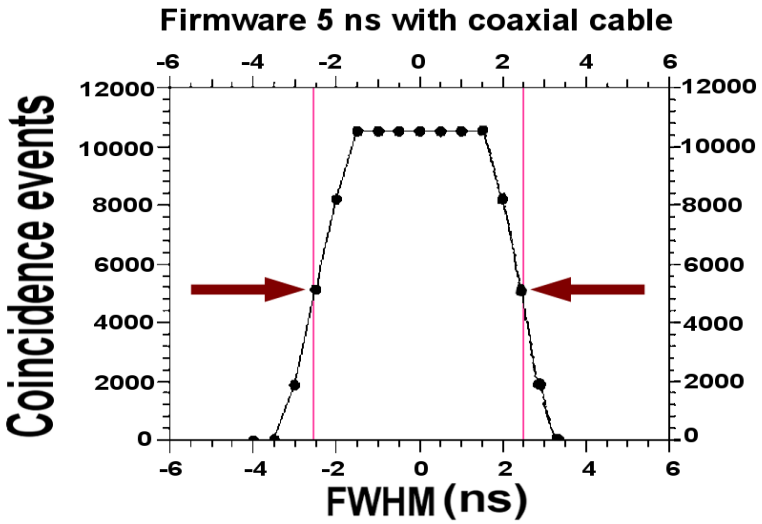

Figure 6.41: Measurement of coincidence timing resolution for the Firmware of 5 ns (with different delay times, which is applied by a coaxial cable).

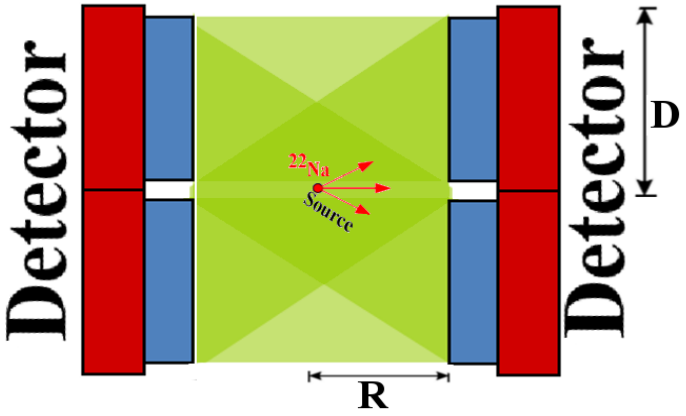

Figure 6.42: The rectangular detector that faces with a point source of ^{22}Na at a distance R in the geometric efficiency measurement.

capability allow our design to more fully utilize the increased solid angle coverage, resulting in significantly increased sensitivity.

To evaluate the detection efficiency, Eq. 6.3 was considered and the value of 6.25% (0.0625) was obtained for the Ω (as geometrical efficiency of the detector), the value of 0.56 was calculated for η from Eq. 3.4. According to the Eq. 3.8, the overall system sensitivity for a point source placed at the center of a detection module is the product of the square of the detection efficiency ε, the geometric efficiency Ω and the packing fraction φ (which was considered 1 here). Hence, a value of 0.035 was obtained.

6.9 Spatial Resolution

The 3-D spatial resolution of the DoPET detector has been evaluated as the FWHM of a reconstructed image from measurements of a point-like ^{22}Na source. The source dimension is about 1 mm diameter. One can safely assume that the source size is dominated by its physical dimension, since the average range of ^{22}Na positron[1]. The source has been placed at the center and at the edge of the FOV of the tomographic prototype. About 6×10^5 events have been acquired for the measurement.

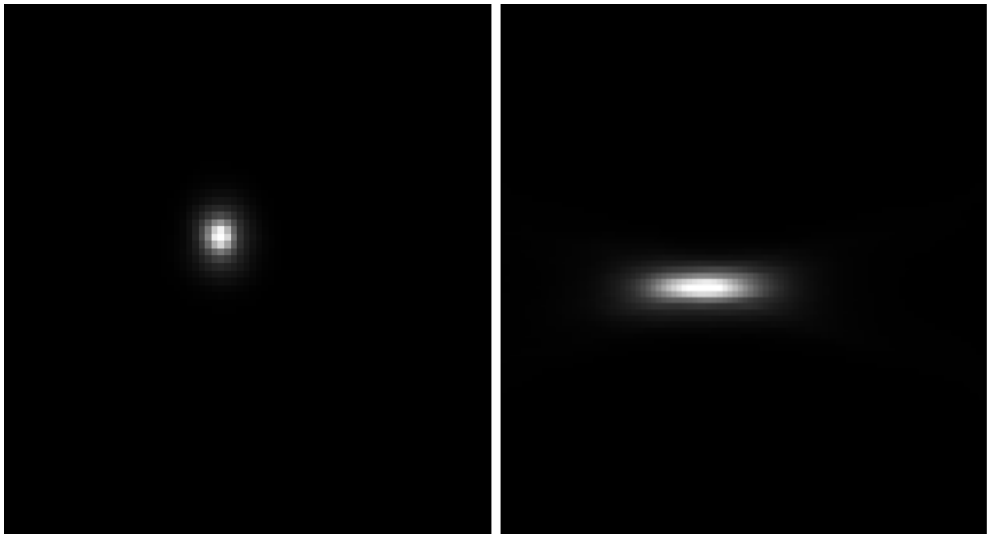

Figure 6.43: Central reconstructed slice (voxel size $0.75 \times 0.75 \times 0.75$) in the xz (left) and yz (right) planes. Data acquired with a ^{22}Na point-source placed in air at the center of the field of view.

Applying a threshold of 150 keV, the sensitivity is 1.1%, while increasing the value of the threshold to 350 keV the sensitivity decreases to 0.75%. Table 6.4 summarized the results. Both energy selections analyzed (150 - 850 keV and 350 - 850 keV) produce similar results, demonstrating that lutetium background events and photon scattering introduce negligible effects. The axial direction of z, is the relevant unit for the dose delivery measurements and the obtained resolution along this axis is about 1 mm σ. Along the y direction, which is the one orthogonal to the detector faces, the spatial resolution is poor. This happens because of the small sensitive area of the detectors with respect to their relative distance, that causes a very limited angular coverage. However, along the y-axis is less relevant for our application.

[1]The endpoint of ^{22}Na β^+ spectrum is 0.545 MeV.

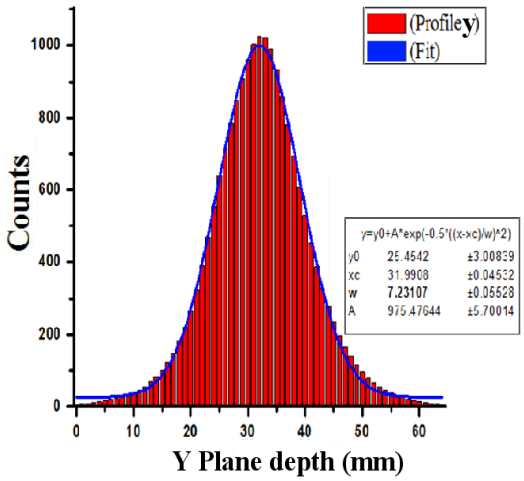

Figure 6.44: Central reconstructed slice (voxel size $0.75 \times 0.75 \times 0.75$) in the y plane. Data acquired with a ^{22}Na point-source placed in air at the center of the field of view.

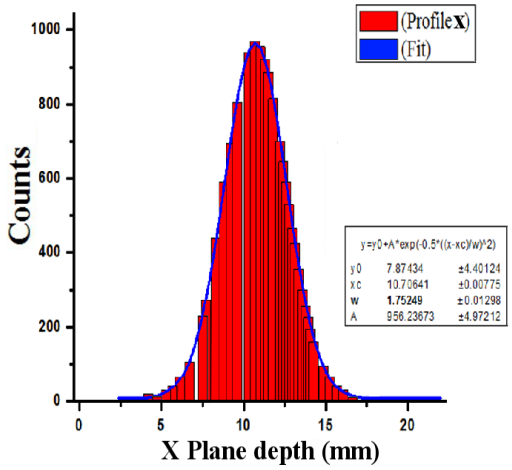

Figure 6.45: Central reconstructed slice (voxel size $0.75 \times 0.75 \times 0.75$) in the x plane. Data acquired with a ^{22}Na point-source placed in air at the center of the field of view.

Table 6.4: The tomographic spatial resolution evaluated for different energy thresholds.

Measure Type Lower Energy Cut	$FWHM_x$ (mm)	$FWHM_z$ (mm)	$FWHM_y$ (mm)
$E > 150keV$	2.62	2.54	10.85
$E > 350keV$	2.62	2.54	10.85

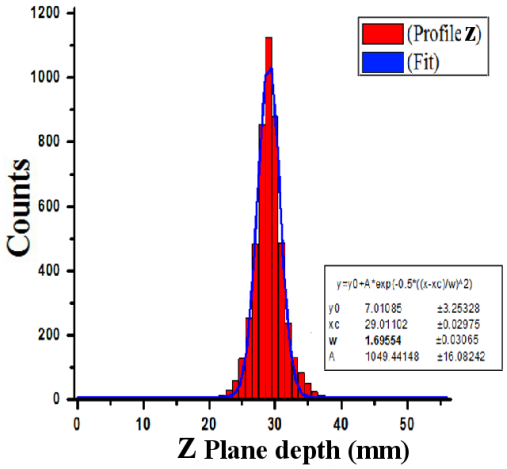

Figure 6.46: Central reconstructed slice (voxel size $0.75 \times 0.75 \times 0.75$) in the z plane. Data acquired with a ^{22}Na point-source placed in air at the center of the field of view.

X/Z is the plane parallel to the crystal surfaces; Y is the directions perpendicular to crystal surfaces.

6.10 Sensitivity

The tomographic prototype sensitivity was evaluated using a ^{22}Na point source positioned at the center of the field of view of the tomographic prototype. The maximum absolute sensitivity with the detector heads 20 cm apart, measured at Center of FoV (CFOV), was 19.3% (19.3 cps/kBq or 713 cps/Ci) for the energy window [50 - 850] keV and 0.90% (14 cps/ kBq or 518 cps/ Ci) for the energy window [50 - 450] keV [163].

6.11 System dead time estimation by simulation

One of the main figures of merit of a PET acquisition system is dead time. This is specially true for clinical systems, in which the radiation dose and scanning interval have to be minimized, thus making of paramount importance to minimize events losses.

In a realistic scenario, if 100 μCi is injected, the isotope disintegration rate would be around 3.7 MHz [164]. Given that the detector scintillators of choice are 16 mm thick pixellated LYSO blocks, we can calculate the absorption probability, which is $\alpha = e^{-d/\mu}$ = 0.75. Where d is the scintillator depth and μ = 12 mm is the attenuation length of LYSO [165]. If we scale the disintegration rate by the absorption efficiency and the solid angle seen from the center to $15cm \times 15cm$ detector plates separated by 8 cm, which is 54%, we obtain single photon rate of approximately 1.5 MHz per detector, without taking into account the single photons coming from the torso and the intrinsic radioactivity of scintillating crystals [132]. At this rate, and given that front-end electronics behave as paralyzable counting devices with dead time τ, The losses and dead time characteristics can be derived from Eq. 6.4 [166]:

$$Looses\,[\%] \approx 100 \times 1.5MHz \times deadtime\,(d) \tag{6.4}$$

The actual efficiency for a given detector material is dominated by the product of the dead time and the front surface area of the detector [167, 168]. Although it is difficult to quantify dead-time losses, state-of-

the-art electronics can handle dead-time management in PET imaging. Detectors modularization has been addressed as the most practical solution for reducing dead time [167, 168, 147].

The motivation behind this study is to gain a sound understanding of the operation of our detection system at high count rates to provide an early characterization of the detection system efficiency. If the detector is subdivided into n modules of dead time, τ, each, the resulting total dead time can be roughly estimated as $\tau_n = \tau / h_n \simeq \tau /$ n , where $1/h_n$ is the fraction of the system being occupied in the acquisition of a coincidence. In fact, if it is supposed that coincidences are evenly distributed among the modules, and that the dead time of the acquisition system is dominated by the contribution of modularized electronics, we can expect $h_n \simeq$ n. The two aforementioned dead-time models are arbitrarily chosen and the actual experimental results "always fall somewhat in between" the two models [169, 170, 161, 171, 118, 172]. Based on this assumption dead time and event losses are estimated by the simulation according to the individual dead times, which have been considered for each part of the detection system. The input event files are created based on the Poissonian distribution [170, 161].

6.11.1 Materials and methods for the implementation

The model, used to estimate event losses has been divided to several phases. Firstly, input events files have been created from a decay source with a shape of Poissonian distribution at the input of CFD module. The CFD is considered as the modularized block, which obeys the paralyzable dead time model.

6.11.1.1 Phase A

Depending on the study, the dosage, and the characteristics of the tomograph, the singles event rate may be 10-100 times the true coincidence rate [113, 111, 173]. Thus, the single event file with mean rate value of 2 MHz and the coincidence event file with mean rate value of 100 kHz are generated. The single events are merged and sorted. A time threshold, which depends on the simulation time, has been imposed to stabilize and synchronize the different Poissonian processes. The same procedure has been done for the coincidence events. The procedure for random events is different, because they are coming from 2 different decaying sources. Two sets of independent single events were generated (with the two event files). The mean rate value for random-coincidences is calculated according to the formula: $R[Hz] = Singles[Hz] \cdot Singles[Hz] \cdot (2\tau)$, (the mean rate value for singles) and 2τ (coincidence window) are considered 2 MHz and 10 ns, respectively. Then the separated sources are merged and sorted with a time threshold (to acquire the events). After doing a filtration with value of 100 ns, random events file is generated.

6.11.1.2 Phase B

In the second stage, the single and the coincidence events, which have been generated from previous stage, are merged together and are entered as the inputs for CFD block. The CFDs are "Paralyzed-Modularized Block" and they obey paralyzable dead time model. Moreover, they are modularized, which means each detection head of the DoPET is subdivided into 4 and 9 segments. After this stage the acquired and lost single and coincidence event rates are estimated and also dead time of the stage is calculated. Figure 6.47, illustrates the explained procedure. The generated events of singles and coincidences after processing in CFDs got got the new values. Due to the paralyzed model:

$$R_{Output,p} = f_p\left(R_{Input}\right) \tag{6.5}$$

Where $R_{Output,p}$ is the number of recorded events (or attended events) and R_{Input} is the number of input events. By considering the modularization of CFD the formula is written as:

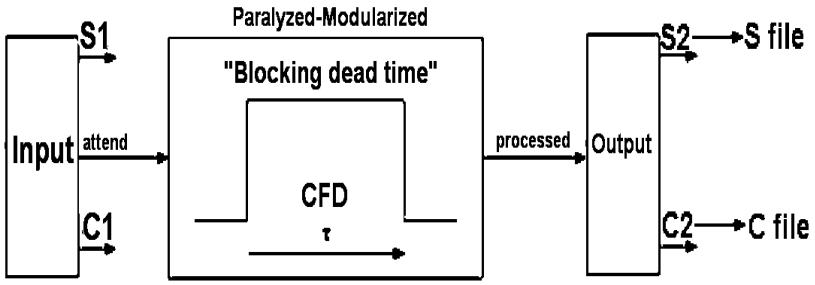

Figure 6.47: The CFDs are considered as a "Paralyzed-Modularized Block" . They process the events as Blocks of dead time of 200 ns.

$$f_{p,m}(R_{Input}, \tau) \rightarrow f_p(R_{Input}, \frac{\tau}{m}) \tag{6.6}$$

In other words, the mentioned relationship indicates that we expect the dead time of modularized CFDs to decrease by factor of m. For instance, if CFD is divided to 4 modules, the dead time decreases by the factor of 4 respect to un-modularized CFD (or 1 module).

6.11.1.3 Phase C

Firstly, the single and coincidence events acquired from the CFD block are merged and sorted. They are prepared as inputs to the coincidence block, which is "Paralyzed-Centralized Block" . Figure 6.48, illustrates the explained procedure. The model for dead time obeys the "paralyzable model" , but it is a centralized block with a small dead time of 30 ns.

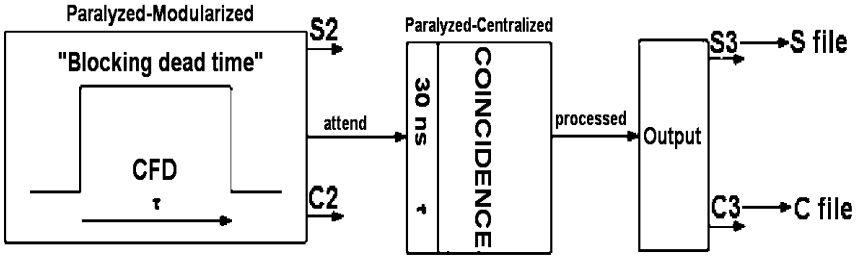

Figure 6.48: The CFD's outputs were entered to the coincidence block, which is a "Paralyzed-Centralized Block" with processing time of 30 ns.

6.11.1.4 Phase D

The single and coincidence events, which have been processed in the coincidence module, are merged and sorted to enter the block of DAQ. Figure 6.49, illustrates the explained procedure. This block is "Non-paralyzed-Modularized Block" , which obeys to the non-paralyzed dead time model. Due to the non-paralyzed model:

$$R_{Output,np} = f_{np}\left(R_{Input}\right) \tag{6.7}$$

Where $R_{Output,np}$, is the number of recorded events (or attended events), R_{Input} is the number of the input events. By considering that the block is modularized, it is expected that the dead time is decreased by a factor of f_{dead} (Eq. 6.8):

$$f_{dead} = \frac{m^2}{m^2 - (m-1)^2} \tag{6.8}$$

Therefore, Eq. 6.7 will be changed to Eq. 6.9.

$$f_{np,m}\left(R_{Input}, \tau\right) \rightarrow f_{np}\left(R_{Input}, \frac{\tau}{f_{dead}}\right) \tag{6.9}$$

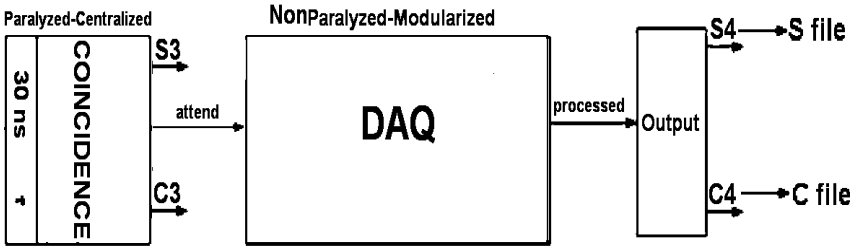

Figure 6.49: The coincidence block outputs were entered to the DAQ, which is a "Non-Paralyzed-Modularized Block" .

At this stage, we are interested on the coincidence events rather the single events.
The transfer function of a PET system is achieved with the following formula [174]:

$$R \sim \frac{FN\exp^{-N\tau}}{1 + FN\exp^{-N\tau}(T-\tau)} \tag{6.10}$$

The total transfer function of the PET system is combination of the following constants:

1. Front-end dead time τ, paralyzable
2. Coincidence network dead time, negligible
3. Acquisition system dead time T, non-paralyzable
4. Loss factor F, due to the CFD discrimination efficiency

The F factor can be considered here equal to 1.

6.11.2 Results

In the results of the simulation, we are looking after some important factors. The first one is the estimation of dead time when each module of detection is modularize to 4 and 9 modules. As it has been shown in Table 6.5, Table 6.6 and Table 6.7, when the events (singles and coincidences) pass through the first block "Paralyzable-Modularized"according to Eq. 6.6, the dead time should be reduced by the number of modules. For instance, in the case of modularizing each module to 4, the dead time should be $200ns/4 = 50ns$ and from the simulation it is calculated 52.57 ns and for the case of modularizing each module to 9, it should be $200ns/9 = 22.22ns$ and it is seen from the results that it was estimated 23.60 ns. Table 6.5, illustrates the

results, which was achieved for the configuration 1 Vs. 1 of module detection. The rate of observed single events through its passing th CFD block was 65.6%. The acquired value has a good correspondence with the paralyzable model (see section 3.10.3.2, Eq. 3.15).

Table 6.5: Assessment of losses of single and coincidence events for the configuration 1 Vs. 1 of module detection. This estimation of events has been illustrated for three blocks of CFD, coincidence and DAQ. The mean rates for single and coincidence events are 2 MHz and 100 kHz, respectively.

Stage	Observed single events (%)	Observed single count rate (MHz)	Observed coincidence events (%)	Observed coincidence count rate (kHz)	Expected Dead time (ns)
CFD	65.5574	1.3111	70.948	70.948	200
COINCIDENCE	95.988	1.258552	100	70.948	30
DAQ	49.36	0.621232	71.39313	50.652	1000

Table 6.6: Assessment of losses of single and coincidence events for the configuration 4 Vs. 4 of module detection. This estimation of events has been illustrated for three blocks of CFD, coincidence and DAQ. The mean rates for single and coincidence events are 2 MHz and 100 kHz, respectively.

Stage	Observed single events (%)	Observed single count rate (MHz)	Observed coincidence events (%)	Observed coincidence count rate (kHz)	Calculated Dead time (ns)
CFD	90.0188	1.800376	90.116	90.116	52.5758
COINCIDENCE	96.567	1.630548	96.24	86.728	
DAQ	74.69611	1.217956	78.9733	68.492	321.0477

The second aim of the simulation was to estimate the loss of events in the block of DAQ (as a part of the acquisition system). In this block, we expected to have a dead time reduction due to Eq. 6.9. According to this equation that dead time should have a minimum value reduction of f_{dead} (Eq. 6.8). The results, which have been presented in Table 6.6 and Table 6.7, show that for a detection system that has been modularized to 4 and 9 modules the acquired dead time are 321.05 and 179.56, respectively. These values have good correspondence with Eq .6.9 and Eq .6.8 (for 4 and 9 modules: f_{dead} are calculated $\simeq$ 2.28 and $\simeq$ 4.76, respectively. From the simulation, we have reductions of $\simeq$ 3.14 and $\simeq$ 5.56, respectively.). The simulation results provided good estimation for the dead time of paralyzable and non-paralyzable block.

In the next step, we try to present how the modularization could be effective in reducing the loss of events when the single and coincidence event are passing through three blocks of dead time. The singles event rate could be 10-100 times the true coincidence rate [173]. The single and coincidence events with different mean rates are generated. The generated single event rates and coincidence event rates were in the range of 2 - 3 MHz and 100 - 150 kHz, respectively. The considered acquisition time for data collecting was

Table 6.7: Assessment of losses of single and coincidence events for the configuration 9 Vs. 9 of module detection. This estimation of events has been illustrated for three blocks of CFD, coincidence and DAQ. The mean rates for single and coincidence events are 2 MHz and 100 kHz, respectively.

Stage	Observed single events (%)	Observed single count rate (MHz)	Observed coincidence events (%)	Observed coincidence count rate (kHz)	Calculated Dead time (ns)
CFD	95.3888	1.907776	95.26	95.26	23.6045
COINCIDENCE	89.2777	1.70322	94.9527	90.452	
DAQ	86.3975	1.47154	87.3975	79.0	179.56

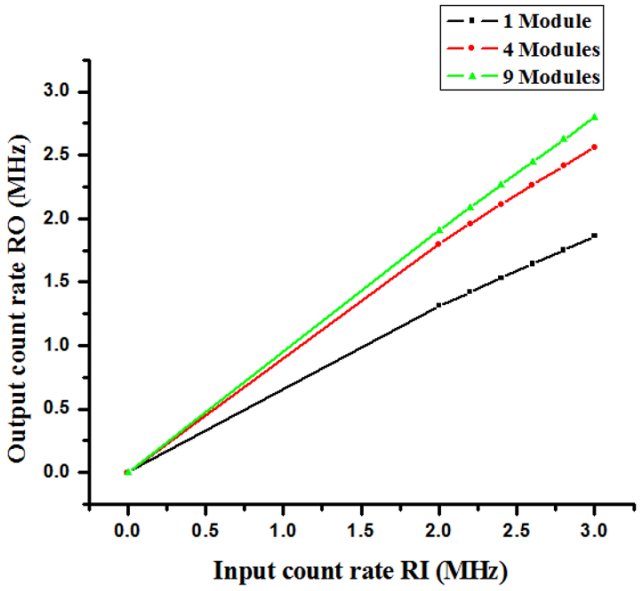

Figure 6.50: The loss of single events, which were acquired from the generated single events, which passed through the CFDs as blocks of "Modularized-Paralyzed". Three different configurations (1 Vs. 1 and 4 Vs. 4. 9 Vs. 9) were considered in order to present how modularization can affect the performance of new DoPET.

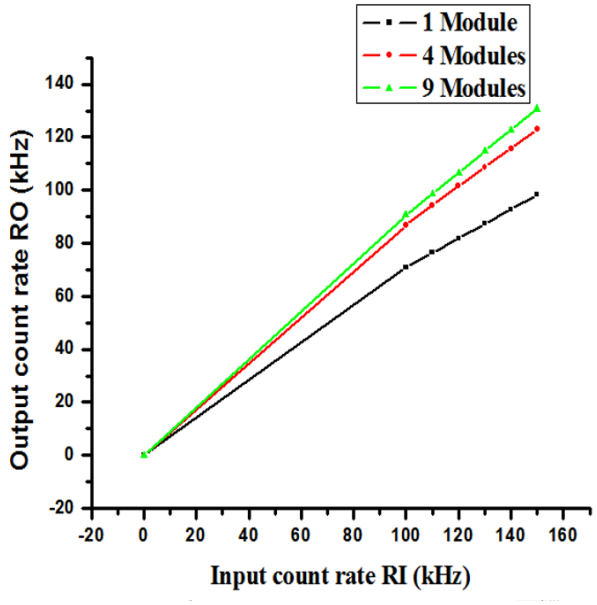

Figure 6.51: The loss of coincidence events, which were acquired from the CFD block. The events passed through the coincidence part as a block of "Centralized-Paralyzed". Three different configurations (1 Vs. 1 and 4 Vs. 4. 9 Vs. 9) were considered in order to present how modularization can affect the performance of new DoPET.

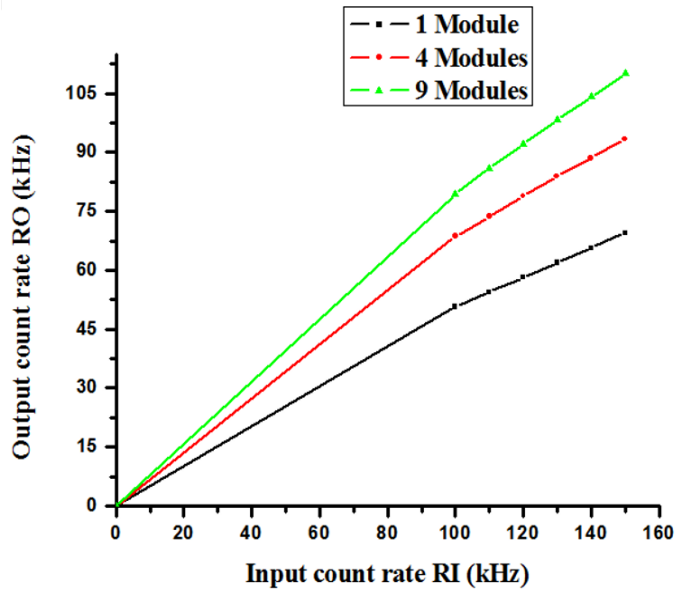

Figure 6.52: The loss of coincidence events, which were acquired from the coincidence block. The events passed through the DAQ part as blocks of "Modularized-Non-paralyzed". Three different configurations (1 Vs. 1 and 4 Vs. 4. 9 Vs. 9) were considered in order to present how modularization can affect the performance of new DoPET.

long enough so as to cover an acceptable statistical range.)

It was understood that in the block of coincidence we have a small amount of dead time. Therefore, most of the coincidence event that arrive at this block are accepted and most of the dead time of the system is related to the CFD modules. In Figure 6.53 and Figure 6.54, plots of transfer functions for the system in the 1 vs 1, 4 vs 4 and 9 vs 9 configurations are reported. Due to Eq. 6.10, we can briefly present the transfer function of a modularized PET [174].

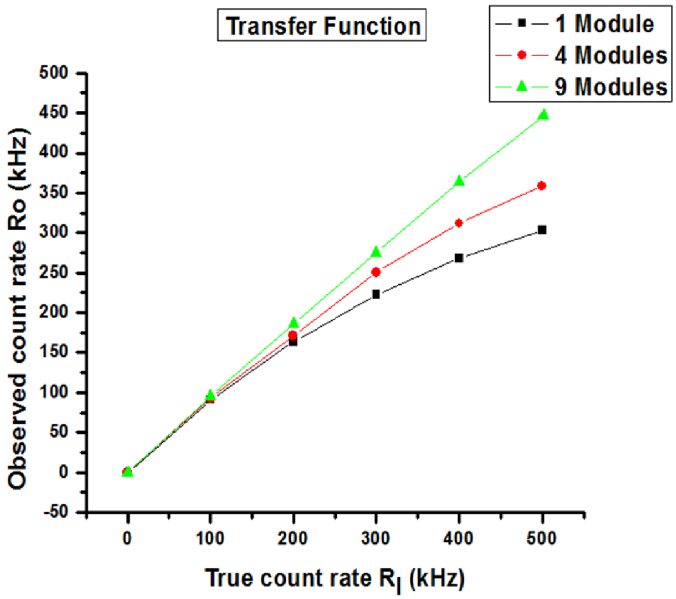

Figure 6.53: Comparison between the acquisition efficiency of the system between the configurations with 1, 4 and 9 modules per detectors.

Figure 6.54, expresses how modularization is necessary to keep event losses under 10% (for modular configuration of 9 Vs. 9) at rates starting from 100 kHz. The 4 vs. 4 implementation is expected to keep such low losses up to rates of 300-400 kHz.

It is evident from the plot that if we want event losses to be below 10% we must keep the dead time below 700 ns. But if we consider that the dead time of the CFD varies from 200 ns to 700 ns, it results that our constraint is hardly achievable with a single processing module per detector plate. Reducing CFD dead time by fine-tuning of comparators thresholds and dynode pulse amplification is not expected to change considerably these values. Deeper technological changes, such as replacing the pulse discriminating technique could solve the problem, but would imply a significant development effort. Conversely, by adopting the modular approach, the total detector dead time it is expected to be reduced by a maximum factor f_{dead}, which was mentioned is Eq. 5.3. where n is the number of modules per detector. This factor is calculated considering the probability that two subsequent photons hit different modules, thus being both accepted even if the first pair is still busy. A summary of expected dead time for different module configurations is reported in Table 6.8.

Table 6.8 shows how the modular approach conveniently reduces the dead time while increasing detector area in a way that the $Area \times Deadtime$ figure of merit increases, thus enhancing the actual detection efficiency. Modularization appears therefore a correct approach for achieving a wide area, efficient PET scanner. However, the reduction in dead time has been roughly estimated, and an experimental validation is

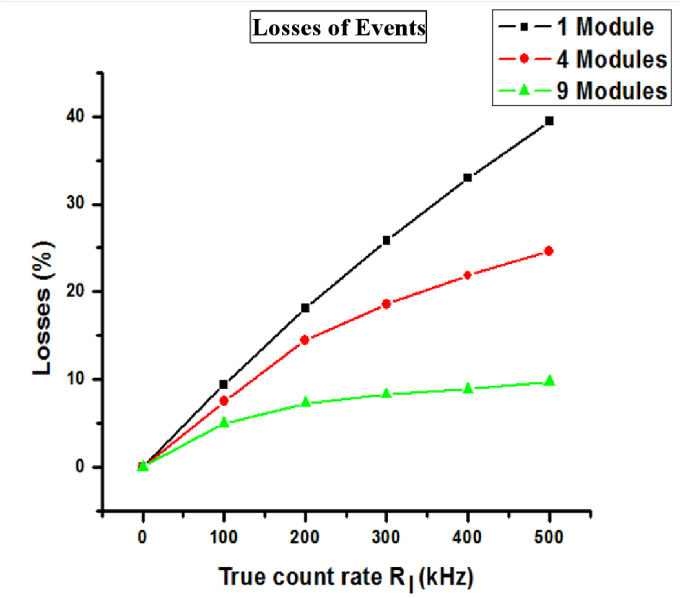

Figure 6.54: Comparison between the acquisition efficiency of the system between the configurations with 1, 4 and 9 modules per detectors.

Table 6.8: Dead time reduction expected by modularizing detector plates.

Modules	Detector area	$Area \times DeadT$.product	f	Expected mean dead time
1	25 cm^2	1.1 cm^2.ns	1	450
2	50 cm^2	1.7 cm^2.ns	1.3	337
4	100 cm^2	2.0 cm^2.ns	2.3	197
9	225 cm^2	2.1 cm^2.ns	4.8	94

required to assess the real performance enhancements. Moreover, the development effort is expected to be low, given that most of detector technology is reused from previous systems.

It is evident from the plot of Figure 6.54 that if we want event losses to be below 10% we must keep the dead time below 700 ns. But if we consider that the dead time of the CFD varies from 200 ns to 700 ns, it results that our constraint is hardly achievable with a single processing module per detector plate.

Chapter 7

Hadron-therapy Dosimetry

7.1 Introduction

The "off line" technique allows analysis of the activity patterns in more detail, e.g. dynamic scans to identify a certain isotope can be performed. Our study is focused on the "off line" analysis of PET activity profiles and its spatial correlation to dose, especially for the case of dose depth profiles.

The technique of PET imaging to measure the β^+ isotopes produced by the proton beam through inelastic collisions inside the patient. Dose is mainly produced by atomic interactions, while β^+ isotopes are produced through nuclear interactions. Hence, the measured activity signal is correlated but not directly proportional to the spatial pattern of the delivered dose. The experiments were set to compare the distal fall-off regions of measured and predicted PET images in order to be done proton range verification [98, 175].

During proton therapy, different β^+ isotopes are produced by nuclear inelastic interactions of protons with the target elements that compose human tissues. Several nuclear reaction channels contribute to the production as shown in table 7.1. It has been observed [176, 177] that up to 95% of the β^+ isotopes produced in the patient are produced by three nuclear reaction channels: ^{16}O(p,pn)^{15}O, ^{12}C(p,pn)^{11}C and ^{16}O(p,3p3n)^{11}C.

Table 7.1: Proton-nuclear reaction channels and β^+ isotopes produced in human tissue.

Target	Nuclear Reaction Channels	β^+ isotopes	Half-Life
C	^{12}C(p,pn)^{11}C, ^{12}C(p,p2n)^{10}C	^{10}C,^{11}C	19.29s,20.33m
N	^{14}N(p,2p2n)^{11}C,^{14}N(p,pn)^{13}N,^{14}N(p,n)^{14}O	^{13}N	9.96m
O	^{16}O(p,pn)^{15}O,^{16}O(p,3p3n)^{11}C,^{16}O(p,2p2n)^{13}N ^{16}O(p,p2n)^{14}O,^{16}O(p,3p4n)^{10}C	^{14}O,^{15}O	70.61s,122.24s
P	^{31}P(p,pn)^{30}P	^{30}P	2.50m
Ca	^{40}Ca(p,2pn)^{38}K	^{38}K	7.64m

Different phantoms where these main reaction channels could be studied independently were built.

7.1.1 The proton beam line

Laboratori Nazionali del Sud (INFN-LNS) in Catania, Italy, the first Italian proton-therapy facility, named Centro di AdroTerapia e Applicazioni Nucleari Avanzate (CATANA) has been built in collaboration with the University of Catania. It is based on the use of the 62 MeV proton beam delivered by the

Superconducting Cyclotron installed and working at INFN-LNS since 1995. The facility is mainly devoted to the treatment of ocular diseases like uveal melanoma. A beam treatment line in air has been assembled together with a dedicated positioning patient system. The facility has been in operation since the beginning of 2002 and 66 patients have been successfully treated up to now.

The CATANA proton beam line has been entirely built at INFN-LNS. The proton beam exits in air through a 50 μm - Kapton window placed at about 3 m from iso-center. Just before the exit window, under vacuum, is placed the first scattering foil made from 15 μm tantalum. The first element of the beam in air is a second tantalum foil 25 μm - thick provided with a central brass stopper of 4 mm in diameter (Figure 7.1). The double foils scattering system is optimized to obtain a good homogeneity in terms of lateral off-axis.

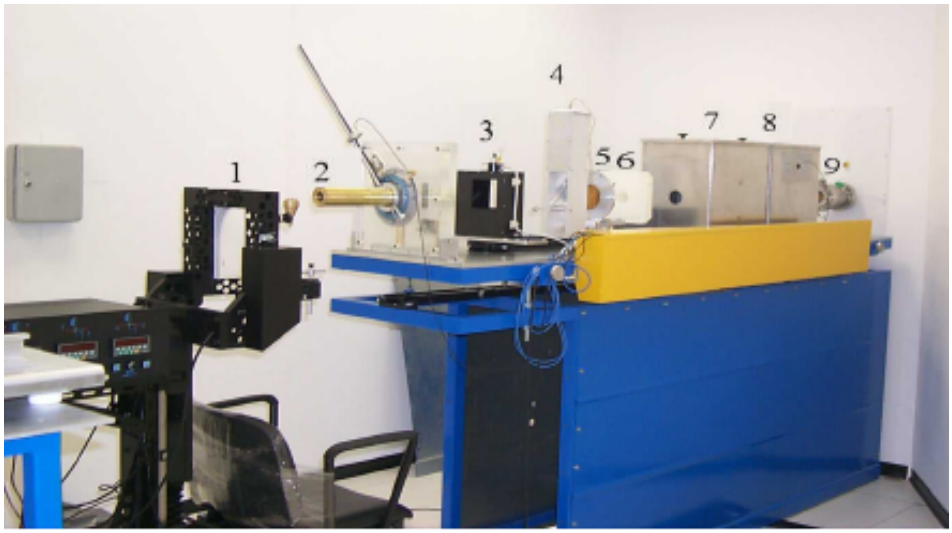

Figure 7.1: View of the CATANA beam line. 1. Treatment chair for patient immobilization. 2. Final collimator. 3. Positioning laser. 4. Light field simulator. 5. Monitor chambers. 6. Intermediate collimator. 7. Box for the location of modulator wheel and range shifter.

7.1.2 Detector design

A 62 MeV proton beam, extracted from the LNS Superconducting Cyclotron, is steered to the CATANA beam line, where it is transversally spread by a scatterer and flattened out over an area larger than the eye dimensions. A range shifter followed by an energy modulator are set to position the Spread Out Bragg Peak (SOBP) at the right place. A 25 mm diameter collimator defines the beam transverse dimensions which are finally matched to the tumor shape by the patient final collimator. The detector has been designed to be placed immediately upstream of the 25 mm collimator. The main constraint of the design of the chamber were:

1. As little as possible thickness crossed by the beam. In fact, the material mass along the beam perturbates the beam energy and shape: it absorbs some of the proton energy and consequently decreases the proton range in the target; the multiple scattering tends to increase the beam dimensions;

2. High granularity to measure the beam profile along both directions;

3. Fast read-out to detect any beam variation in real time.

7.1.3 Materials and methods

A PMMA phantom was activated with 62 MeV protons at the CATANA. The beam direction was perpendicular to the entrance surface of the two detector heads and the third axis of the coordinate system.

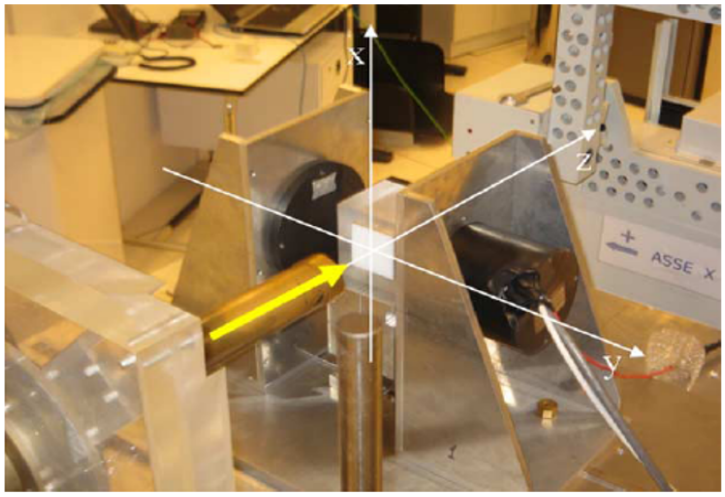

Figure 7.2: The installation of the experimental setup at the CATANA beam line. The brass nozzle is visible on the left, the plastic phantom is centered on the beam line and the two detector heads are mounted at the phantom sides, at a distance of 14 cm from each other. The mechanical holder has been built so as to be able to position the detector heads with precision and reproducibility, both in the calibration and in the validation measurements. The chosen coordinate system has been superimposed on the picture.

Figure 7.2 illustrates the beam direction, the direction perpendicular to the entrance surface of the two detector heads and the third axis of the coordinate system. In the actual experimental set-up, the PET prototype allows a spatial resolution of 1 mm σ along z and at the center of the field of view (FOV), but its limited angular acceptance prevents from reaching the same resolution along the y-axis (currently of $\approx$ 7 mm) [108, 109].

The PMMA phantom of 10 mm has been constructed. The effect of target activation dependency on the proton energy in the FOV has been studied (phantom positioned along the beam direction). The measurement was done with PMMA along the z-axis set side by side and located between the detector heads so that the beam direction was perpendicular to the slab. Pencil-like proton beams of 62 MeV with an initial energy spread of about 300 keV, shaped by a brass collimator with an aperture diameter of 25 mm, were delivered to the phantoms into the CATANA treatment room for eye tumors [178]. During irradiation, phantom was positioned at the center of the field of view with the detector heads at a distance of 14 cm.

Scanning of the induced activity started about 20 - 40 min after the irradiation. Different sets of data were taken. Firstly, the activity signal for a dose profile of a Raw Bragg Peak (RBP) of 62 MeV protons was recorded; then the activity pattern induced by a spread out Bragg peak (SOBP) of 2 cm plateau width with 62 MeV protons was analyzed to compare with the activity induced by a raw Bragg peak. Furthermore, our experiment is not sensitive to the strong ^{15}O activity signal arising from the process ^{16}O(p, pn)^{15}O because most of the produced ^{15}O isotopes, with a half-life of 2.02 min, decay before the PET scanning procedure is done.

The choice of PMMA (Figure 7.3) as a phantom material therefore yields an activity signal whose analysis and comparison to model calculations is not affected by insufficient or poor data for the isotope production mechanism. Clearly PMMA cannot serve as a tissue equivalent probe; however, it can serve

well to study the general mechanism of proton dose monitoring with PET techniques. PMMA was chosen as phantom material because its nuclear composition ($C_5H_8O_2$) together with our "Off-line " scanning technique guarantees a strong and almost clean activity signal from the activation process ^{12}C(p,pn)^{11}C.

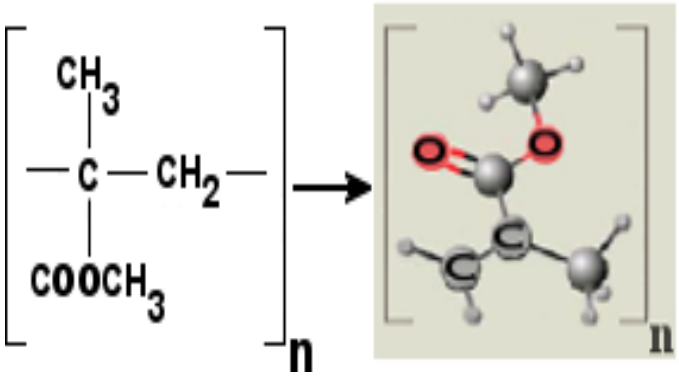

Figure 7.3: Structure of Polymethyl-Methacrylate.

A mono-energetic proton field with 10 cm range ($\sim$ 62 MeV) and a spread-out Bragg peak (SOBP) field with 10 cm range and 6 cm modulation (Figure 7.1) were delivered to the phantom at one of the gantry rooms of the Laboratorio dell sud (Catania, Italy). The mono-energetic field was used in order to minimize the spread of the energy spectrum of proton contributing at different depths of the phantom, while the SOBP field was The dimensions are $12 \times 12 \times 6cm^3$.

The mono-energetic field was used in order to minimize the spread of the energy spectrum of proton contributing at different depths of the phantom, while the SOBP field was used to analyze a realistic case scenario. A $7 \times 7cm^2$ square aperture and no compensator was used in both cases and the beams were directed perpendicular to one of the bases of the phantom and centered with the interfaces of the different materials (Figure 7.1). Thus, all materials are irradiated at the same time allowing simultaneous analysis of the measured data. The entrance dose delivered with the mono-energetic field was calculated in order to produce similar activity level to the one achieved when 2 Gy are delivered at the flat region of the SOBP field. The time between the two irradiations was 2 h, which corresponds to 6 half-lives of the produced β^+ isotope with longer half-life (^{11}C, $T1/2$ = 20.33 min). After each irradiation the phantom was taken manually from the treatment couch, placed inside the PET scanner's field of view (FOV) and acquired in list mode for 45 min.

For the irradiations a proton current ranging between 1.0 nA and 5.0 nA was extracted from the cyclotron. The phantom, a PMMA cylinder of 4 cm diameter and 5 cm length placed 10 cm downstream from the final collimator was irradiated with a uniform lateral beam profile of 20 mm or 30 mm in diameter. The irradiation time varied between 15 and 30 min, and an estimated total dose from 30 Gy up to 60 Gy was delivered to the phantom. The proton ranges in PMMA for the selected energies of 62 MeV are approximately 2.9 cm, respectively. Table 2 summarizes the irradiation parameters of our experiments, i.e., the proton energy E_0, the proton flux ϕ, the irradiation time t_R and the estimated total dose delivered to the phantom.

The total activity induced in the PMMA phantom right after the beam was turned off was estimated to range between 5.9 MBq and 0.2 MBq. An activity of 5.9 MBq will produce a single rate well below 2 MHz on each head. The estimate of the induced activity per volume only takes into account the main activation of ^{11}C from ^{12}C. After a time delay of 20 - 40 min, the phantom was scanned with our PET scanner. This scanner analyses an axial field of view of 10.4 cm in depth so we obtain 31 lateral activity profiles, each separated by a depth of 3.375 mm.

7.2 Measurements by applying the final detector assembly

The high anode luminosity of the PMT used were compatible with the preamplification stage. To avoid the ADC saturation the PMTs have been operated at a voltage much lower than the suggested operating one (850 V instead of 1000 V). The final step of detector optimization has been the tuning of front-end electronics amplification. This has allowed to use the PMTs in a more reliable operating condition, obtaining much less instabilities.

The reproducibility of look-up tables each time the detector is assembled has been then assured by gluing the crystal matrices to the PMT photo-cathodes. Minimal relative shifts were now possible between the crystal grid and the photo-cathode. This has allowed us to perform the final characterization measurements in Pisa laboratory, and to use the results in the last run in Catania.

Figure 7.5 presents the in-depth profile of the measured activity distributions. The shifts in beam range up to 1 mm are successfully detected as shift in activity distribution fall-off. It is interesting to compare results obtained in different runs with the same dose configurations. The minor changes introduced in the acquisition setup has not altered results and conclusions. The reliability of the results is then well supported by their reproducibility. Measurement reproducibility is fundamental for the quality assurance of clinical treatments, since images produced from different fractions delivered to the same patient in different days will be compared.

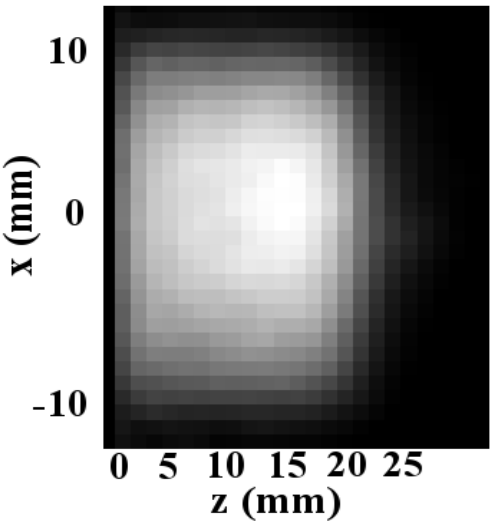

Figure 7.4: Reconstructed 2D distribution of integrated β^+-activity in central xz plane.

Shifts in activity profile has been measured as shifts in the 50% distal fall-off of the activity profile along the beam direction in the central slice of the reconstructed images. Profiles are evaluated on a single voxel row. Integration on more pixel rows would lead to a reduced statistical fluctuation in the results on beam direction, but would make the results dependent from the coronal profile of the beam. Shifts in proton range have been measured as shifts in practical range measured from in-depth dose profiles.

The depth of the Bragg peak depends on the initial energy of the ions, while its width on the straggling and on the energy spread of the beam which, to make good use of the distal steep drop of the peak, has to be nearly 1%. By varying the energy during the irradiation in a controlled way. By the modulation of the beam energy of the accelerator during the irradiation many narrow Bragg peaks superimposed and SOBP (Spread-out Bragg Peak) obtained.

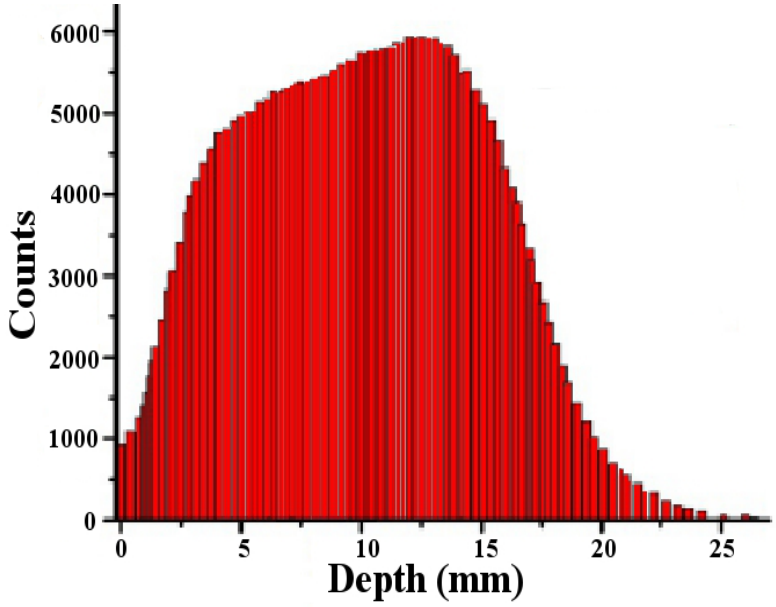

Figure 7.5: Measured β^+ activity depth profile for proton ion irradiation of PMMA target at 62 MeV.

The PET prototype has allowed geometrical information to be inferred from the reconstructed images. Figure 7.4 shows the PET images of the irradiated PMMA phantom. In this figure, the two-dimensional positron emitter distribution in the central xz plane shows a significant activity contrast.

The results achieved in the phantom study highlighted the potentialities of the PET method in the monitoring of dose delivery in proton therapy. Irradiating PMMA phantom at different position along z-axis, we tested the PET scanner response dependence on the position of the PMMA interface within the field of view, demonstrating that it is possible to detect the PMMA layer thickness up to few millimeter before the Bragg peak.

Chapter 8

Conclusions and Future Work

The "On-Line" PET is one of the most promising techniques for quality assurance in hadron-therapy. Within the DoPET project we started an evaluation of potentiality of dedicated PET scanners for hadron-therapy monitoring. To such aim we have designed a dedicated PET scanner based on a pair of opposing detector heads, made up of a $1.9mm \times 1.9mm \times 16.0mm$, with a 2.0 mm pitch LYSO scintillator matrix.

The DoPET project had the goal to achieve the detection of 1 mm range differences in proton beam irradiations performed at the CATANA facility on plastic phantoms. Theoretical prediction (section 8.2) demonstrates the feasibility of such purpose.

For The new version of the detector a new readout system was developed. An independent readout of all the PMTs of one head is applied in order to avoid an increase of pile-up and dead time in the acquisition. The coincidence procedure as logical functions was implemented in Stratix III FPGA in order to to handle the coincidence events, which are detected between each PMT of one head and any PMT of the opposite head. By combining the information of all the PMTs, a recovery of the dead area at the photo-multipliers is also achieved.

After detector optimization and calibration, the characterization of planar has been done and the 3D performances have been evaluated. Flood field images have shown an average peak-to-valley ratio of 4.6, an average crystal pixel resolution of about 0.7 mm and an energy resolution lower than 18.9%. Data contamination from random and ^{176}Lu coincidences, as well as non-uniformities in pixel sensitivity, have been characterized and corrected for in the image reconstruction.

Image reconstruction is performed with a 3D ML-EM iterative algorithm, using a probability matrix based on a multi-ray method. Geometrical symmetries and physical processes which lead to event detection can be modeled. At present the crystal depth of interaction is not implemented, but future improvements are foreseen.

Further funds have been received for the next stage of the DoPET project, for realizing a larger version ($15 \times 15\ cm^2$) of the detectors. The realization of next stage of DoPET project with the field-of-view of $15 \times 15 \times 20\ cm^3$ has been started. The new one produce a significant increase of angular coverage. For typical clinical irradiations of 15 Gy over a 15 cm^3 volume, the statistic collected in ten minutes would then increase to approximately 1×10^6 events, about a factor nine with respect to the one module detector.

The new version of the detector would require developing a new readout system. In fact, an independent readout of all the PMTs of one head is required in order to avoid an increase of pile-up and dead time in the acquisition. On the other side, this forces us to develop a system able to handle coincidences between each PMT of one head and any PMT of the opposite head. By combining the information of all the PMTs, some recovery of the dead area at the PMTs periphery could also be obtained.

Regarding the reconstruction algorithm, some changes will be needed for the larger planar version of the detector. All the attention could be then focused to improve the precision of physics modelization within the probability matrix. For the clam shell heads, the new detector geometry should be also implemented.

The unfolding algorithm would not require substantial modifications (except for the point-spread function and the efficiency adopted), to be adapted to the clinical device for proton therapy monitoring. Present work on 3D dose filtering and on computation of the inverse filter can go on as foreseen by the original project.

The larger device, however, will also sign the evolution from proton eye-therapy monitoring to a more general hadron-therapy monitoring device. Further carbon beam irradiation will be then planned, and a more general algorithm for dose unfolding will need to be developed.

In the "Off-beam" PET method: the β^+ emitter distribution induced in the patient by the irradiation is measured with a commercial PET outside of the irradiation room. The advantage of such approach is that it does not require particular developments but the moving of the patient from the treatment site to the PET scanner introduces large uncertainties. The "Off-beam" strategy investigate, e.g. using PET / CT instead of PET imaging alone, using the same patient positioning system for irradiation and PET measurement and moving the patient without release from the positioning system to a scanner installed as close as possible to the treatment site. However, "In-beam" PET method is used for the quality assurance at hadron-therapy center since 1997: the acquisition is performed during the irradiation and some minutes after which allows the detection of both short-lived and long-lived isotopes and avoids to move the patient. Moreover we can imagine that such "In-Line" PET could be improved to become an "On-Line" PET in conditions that number of LOR (Lines of Responses) detected is large enough and time of reconstruction is short enough to provide typically an image every tens of seconds.

The properties of charge particle beams make it a sharp knife that has to be used with extreme precaution so that tissue exposure to a high dose within the high-RBE Bragg peak is restricted to the tumor volume only. For this reason, imaging techniques allowing to monitor the beam localization as it penetrates the target are highly desired. Making use of positron emission tomography by using β^+ decaying radioactive projectiles. The achieved activity densities within the irradiated volume, depending on the half-life of the isotope. The method offers the advantage of providing a high activity suitable for high-statistics (from the point of view of the positron tomograph) PET imaging. It delivers important clinical information by verifying the correspondence between the planned and delivered treatments. But it has two main drawbacks:

- the activity created in the tumor and surrounding healthy tissue is washed out by the blood circulation during the patient irradiation, transport to the PET room and during the PET scan itself, leading to image blurring and false different intensities in highly versus poorly perfused tissue and, more importantly,
- anatomical changes occurring during the course of any a-posteriori fractionated irradiation will no longer be detected, together with the impossibility of verifying the portal positioning during those irradiation.

In dose distribution evaluation, the use of PET to image β^+ activity distributions induced in the target volume during patient irradiation is currently the most promising technique for in situ, non-invasive dose delivery monitoring. "In-beam" PET is feasible for high energy photon irradiation with energies above $\simeq$20 MeV because of the generation of positron emitters in tissue (predominately ^{15}O and ^{11}C) by (γ,n) reactions. By means of the "In-beam" PET the ^{15}O and ^{11}C activity distributions could be measured. Higher activity concentrations are determined in comparison to "Off-beam" PET experiments depending on the oxygen content. Due to the different half-lives of ^{15}O and ^{11}C ($T_{1/2}(^{11}C)$ = 20.38 min, $T_{1/2}(^{15}O)$ = 2.03 min) a good contrast between materials with various density values can be achieved.

Discussions on how to further improve PET performance have focused on the two parameters that most affect lesion detectability: sensitivity and resolution. In 2D PET acquisition mode, sensitivity can be improved by reducing the length of the septa, thereby increasing the acceptance angle of the detectors, but this gain in sensitivity is at the cost of a reduction in image resolution. The larger focus is on how to improve 3D acquisition. Here the principal hurdles are how to remove the increased scatter fraction and how to reduce random events. It is with the objective of overcoming these hurdles that we are interested in exploring the

properties of LYSO detector materials. The property that affects sensitivity is ρZ_{eff}^4, which for our current detectors is the second highest after BGO. The property that affects the coincidence timing window is the lifetime of the fluorescent emission. The property that affects the accuracy in determining the position of an event within a detector block and also impacts on energy resolution is the light output that can be collected within the coincidence timing window. Higher light output can therefore improve spatial resolution and energy discrimination, thereby reducing the scatter fraction. It is for these reasons many research are invested in the development of crystals for PET detector blocks [165].

The acquisition system of the DoPET scanner, could sustain acquisition rates up to 50 kHz still giving good imaging results. We also know that "In-beam " scans see count rates that are significantly higher in the first minutes of the acquisition, which are at the same time the most important for isotope separation studies. It would then be safe to set a target data throughput bandwidth of 1 MHz that, being the event size 20 bytes, translates to a data streaming bandwidth to the host of 20 MB/s. This bandwidth is compatible with the proposed host interface, i.e. the USB, being its maximum bandwidth 60 MB/s. However the achievable bandwidth also depends on the acquisition protocol, and the software implementation, so that it is proper to do a test on-the-road in order to assess the real accessible capabilities.

The attained reconstructed images from our PET are affected by the two effects 1- Positron Range and 2- Non-collinearity. These effects place some finite limits on the spatial resolution attainable with the PET and manifest themselves as a blurring. In the other words, it could be expressed that it can be lead to errors in determining the line along which a positron-emitting radionuclide is to be found. Moreover, the ultimate resolution that was achieved, affected by the physics of the positron decay.

In contrast to the planar version of the detector, in continuous detector system, the crystal pixel resolution of the detector is largely determined by the number of scintillation photons available for determining the position of the event, not by geometric factors. But, the same types of physical components such as: detector scatter, light sharing, cross-talk and so on) contribute to the crystal pixel resolution. The crystal pixel resolution of a continuous detector can typically be approximated by a Gaussian with a particular FWHM.

By setting a head-to-head distance of 14 cm, an overall sensitivity of about 1% has been measured, and a spatial resolution lower than 3 mm (FWHM) has been obtained from image reconstruction along beam and vertical directions. The characterization along y is still unsatisfactory, but this was expected form the geometrical design of the prototype. This aspect has been taken into account in the choice of beam configuration for proton and carbon irradiations. The validation on plastic phantoms with proton irradiations has been successfully performed at the CATANA beam line, using sharp and spread-out Bragg peaks at proton ranges and finally reproducibility of results has been verified.

The independent readout of all the PMTs helped us to avoid an increase of pile-up and dead time in the acquisition. On the other side, this forces us to develop a system able to handle coincidences between each PMT of one head and any PMT of the opposite head. By combining the information of all the PMTs, some recovery of the dead area at the photo-multipliers periphery was obtained. Regarding the reconstruction algorithm, minor changes will be needed for the larger planar version of the detector. All the attention could be then focused to improve the precision of physics modelization within the probability matrix. The larger device, however, will also sign the evolution from proton eye-therapy monitoring to a more general hadron-therapy monitoring device. Further carbon beam irradiation will be then planned, and a more general algorithm for dose unfolding will need to be developed.

Appendices

Appendix A

Delayed Window Technique

With the delayed window method the determination of a random line-of-response (LOR) consists in measuring both LOR vertices, i.e., the points of interaction of the single events both in the delayed and non-delayed side. In this case the two detectors involved in the delayed coincidence are triggered to acquire the position of signals, when a delayed coincidence is detected. In principle, the correlation between the single events generating the delayed coincidence and those used for the random LOR is not required. Any randomly chosen single counts can be used for the generation of a random LOR. The only limitation is given by the fact that the random count rate for each LOR should be measured on-line in the exact conditions due to the time dependency of the random rate distribution. With this assumption, to avoid the problem of acquiring the signals produced by the event in the delayed side, a different approach for estimating a random LOR has been followed. A random LOR is measured when a delayed coincidence is detected, i.e., a delayed time signal in one detector is in time coincidence with a non delayed signal in a second detector. This technique has the advantage of a low systematic error. The random counts are measured by the same acquisition chain of the coincidence events with the same dead time, but the random distribution is usually affected by strong noise due to the relatively low statistics. This noise also affects the reconstructed image [179].

Innovative delayed window timing technique as the key to estimate random events

On the coincidence board a new scheme was designed to measure random counts. The system has been symmetrized by generating a delayed timing signal on both sides. The logic OR of the delayed signals on one side is in coincidence with the non-delayed signal of the other side and vice versa. Once a delayed coincidence is detected, only the signal on the non delayed side is acquired. In this way, only a single vertex of the LOR is measured. This event is called a random single. Since the system is completely symmetric, it is assumed to measure an equal number of random singles on both sides. The rate of these random singles will be equal to the actual system random count rate. The fluctuation of the numbers of random singles on both sides will be only related to the count statistics. Once the single random events are acquired, a random LOR can be generated by the coordinates of the first random singles available on each side [133].

Innovative delayed coincidence

In the new symmetrical delayed window approach, the delay ΔT is applied only at the OR of the timing signals on both sides. In this way only one side, the non-delayed one, is triggered when a delayed coincidence is detected. Figure A.1 and Figure A.2. illustrate the new approach.

The innovative method allows:

- A more flexible implementation.

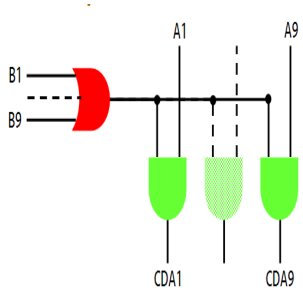

Figure A.1: New symmetrical delayed window approach.

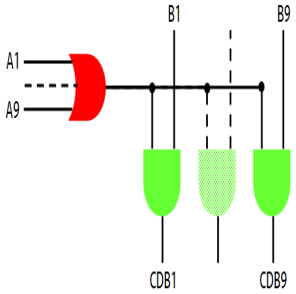

Figure A.2: New symmetrical delayed window approach.

- No additional dead time.
- Lesser pile-up.

Thus, the last two items create the possibility to exceed the solid angle limits, which is imposed by noise equivalent count rate.

The technique strongly reduces the noise in the estimated random distribution and does not require any single counts measurements and/or a-priori estimation of the width τ of the coincidence timing window. Moreover, the potential advantage of this approach resides on having the double blind distributions R_i and R_j readily available by analyzing the distribution of the random singles of the two heads separately [133].

When all of the elements i on head A are in coincidence with all of the elements j on head B, the expected random count rate in the LORs connecting element i on head A and element j on head B (R_i and R_j) are given by Eq. 1 and Eq. 2:

$$R_j = \Sigma_i \, r_{ij} = \Sigma_i \, c_i \cdot c_j \cdot 2\,\tau = C_A \cdot c_j \cdot 2\,\tau \tag{A.1}$$

$$R_i = \Sigma_j \, r_{ij} = \Sigma_j \, c_j \cdot c_i \cdot 2\,\tau = C_B \cdot c_i \cdot 2\,\tau \tag{A.2}$$

Where R_i and R_j are the double blind random distributions, i.e., the spatial distribution of the single counts involved in a delayed coincidence (random single) on heads B and A, respectively, whilst C_A and C_B are the total singles count rate on the head A and B, respectively. Multiplying Eq. 1 by Eq. 1, Eq. 3 has been achieved. r_{ij} can be fully estimated from the measured random count distributions because the estimation of C_A, C_B and τ, is not necessary since $R(= \Sigma_{ij} \cdot r_{ij}$ is the total random count rate).

$$R_i \cdot R_j = C_B \cdot c_i \cdot 2\,\tau \cdot C_A \cdot c_j \cdot 2\,\tau = (c_i \cdot c_j \cdot 2\,\tau) \cdot (C_A \cdot C_B \cdot 2\,\tau) = [(R_i \cdot R_j)/R] \cdot R = r_{ij} \cdot R \tag{A.3}$$

Appendix B

The rationale for passive delay line

The Passive Delay Line[1] as a special purpose "Low Pass Filter" was considered to delay (phase shift) the input signal by a specified increment of time from CFD that attends at DAQ board as a part of the acquisition system of DoPET.

The Design considerations for the DAQ's delay line

The PDL is a LC network that may be used to pass either analog or digital signals whose bandwidth is compatible with the intended range of operation for the delay line. A specific delay and impedance determine the required LC values of the network. Figure. B.1 illustrates the parameters, which are necessary to be considered to present concept of the passive delay line.

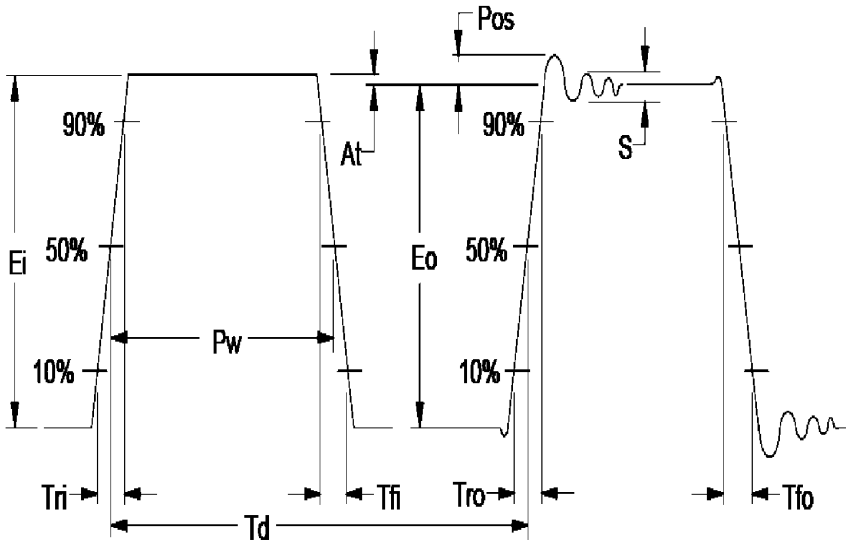

Figure B.1: Passive Delay Line Waveform Parameters: Attenuation (At), Input Fall Time (Tfi), Input Rise Time (Tri), Input Voltage (Ei), Output Rise Time (Tro), Output Fall Time (Tfo), Output Voltage (Eo), Delay Time (Td), Pulse Overshoot (Pos) and Pulse Width (Pw).

[1] PDL

As it is seen in Figure B.1, "Td" defines "Total Delay" the elapsed time (ns) between the respective 50% points on the leading edges of the input and output pulses and it is defined as:

$$Td = (L_t) \times (C_t) \tag{B.1}$$

In Eq. 4, "L_t" is "Total Line Inductance" and it is expressed in henry. "C_t" is "Total Line Capacitance" and is expressed in pF. The other parameter is "Z_O" , which is "Impedance" and it is expressed in ohm. The effective impedance of the delay line which is equal to the value of the terminating impedance, which provides a minimum reflection back to the input of the delay line (Eq. B.3):

$$Z_O = \frac{(L_t)}{(C_t)}^{1/2} \tag{B.2}$$

The rise time of a delay line (Eq. B.3) is typically measured from the 10% to 90% points of the leading edge of the output pulse. The measured output rise time (t_{ro}) is a function of the input rise time (t_{ri}) and the true rise time of the delay line (t_r):

$$t_r = \sqrt{{t_{ro}}^2 - {t_{ri}}^2} \tag{B.3}$$

An analog delay line's bandwidth (-3dB attenuation) is related to the network's rise time which is dependent upon the total number (N) of LC sections. The delay-to-rise time ratio is the figure of merit, or Quality Factor, used to characterize delay lines. Generally, the greater figure of merit implies higher number of sections, and therefore higher cost. The bandwidth for the network, and number of sections follow these approximations (Eq. B.4 and Eq. B.5):

$$BW \approx \frac{0.35}{t_r} \tag{B.4}$$

$$N \approx (\frac{Td}{t_r})^{1.36} \tag{B.5}$$

The output voltage attenuation of the delay line has several contributing factors:

1. Internal D.C. resistance (DCR),
2. Dielectric and ground plane losses,
3. Loading effects at taps,
4. Impedance mismatches at terminations and
5. Frequency limitations (BW) of the delay line

When the delay line is minimally loaded, properly terminated and the input pulse widths are significantly greater than the line's rise time, attenuation is given by (Eq. B.6):

$$Attenuation\,(\%) = 1 - \left(\frac{Zo}{Zo + DCR}\right) \tag{B.6}$$

The passive delay lines of the same impedance can be connected input-to-output (cascaded) to optimize rise time and/or obtain specific delay values. Termination is required only at the output of the final stage. The rise time of the grouped lines is given by (Eq. B.7):

$$t_{ro} \;=\; \sqrt{{t_{ri}}^2 + {t_{r1}}^2 + {t_{r2}}^2 + {t_{rN}}^2} \tag{B.7}$$

The architecture design of the passive delay line

In the acquisition system of DoPET, each DAQ board is provided with an input inductive delay stage, which is required to compensate coincidence processing delay. The implemented delay must be sufficiently long in order to turn on the peak detector before the actual energy signal peak has passed through (this also was hinted in Figure 4.3). If the generated output signal after the delay line has the characteristics: rise time of 35 ns with delay length of 100 ns respect to input signal, the aim has been satisfied.

To acquire the desired characteristics, values of inductances and capacitors were calculated (from Eq. B.1 and Eq. B.2) and then by the assistance of "Altium Designer 2009" software, all of the calculated values of L and C were implemented in the simulation. After the simulation, the delay line was constructed. Figure B.2, illustrates the applied test circuit for the designed passive delay line. As it is seen from Figure B.2., all the values for the testing have been provided.

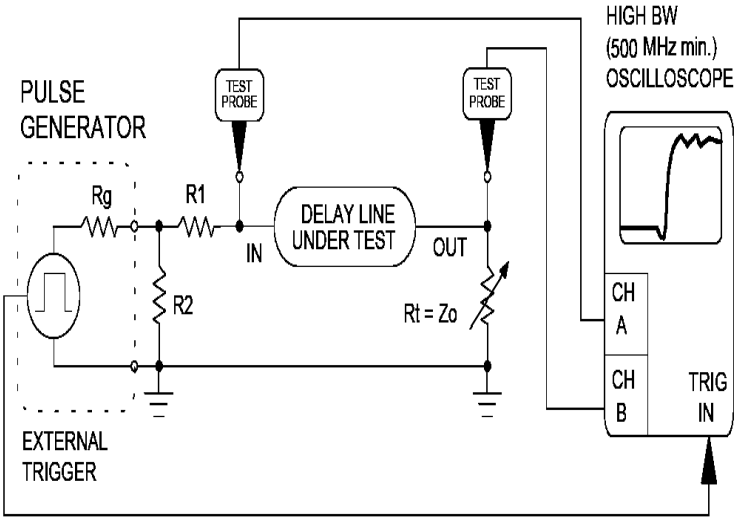

Figure B.2: The applied test circuit for the Passive Delay Line. R_g is the generator source impedance = 50 Ohms, R1, R2 are the input matching pad resistors, Rt is the terminating resistor, $R1 = ((Rg \times Zo)/R2)$, $R2 = \sqrt{Rg^2 \times Zo/Zo - Rg}$ and Zo is the delay lines characteristic impedance.

Output of the designed delay line

Overshoot and ringing are problems of LC circuits, which are designed by employing passive components (LC) as a passive network and they must be damped down and reduced as much as possible. If energy is removed at frequencies of ringing frequency, we will not have a loss in gain and / or efficiency of the circuit.

The solution to overcome this difficulty is that: once a point in the circuit that changes the ringing frequency is found, add capacitance to this point until the ringing frequency approximately halves (the period doubles and the time between zero crossings doubles). Firstly, it is considered the values ($t_{with-cap}$) and

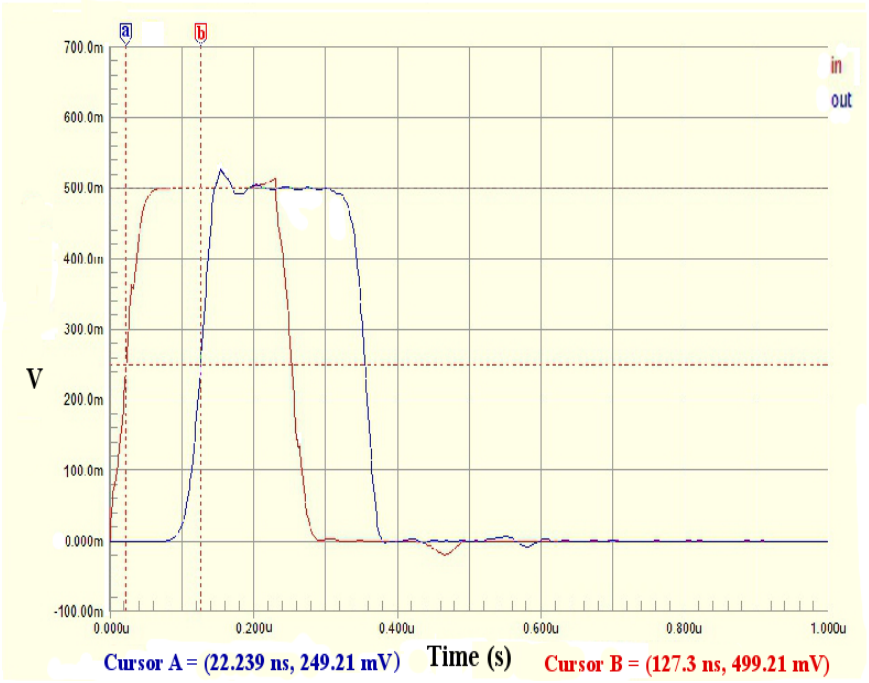

Figure B.3: The output signal of the designed delay line, which shows a delay of 100 ns respect to the input signal.

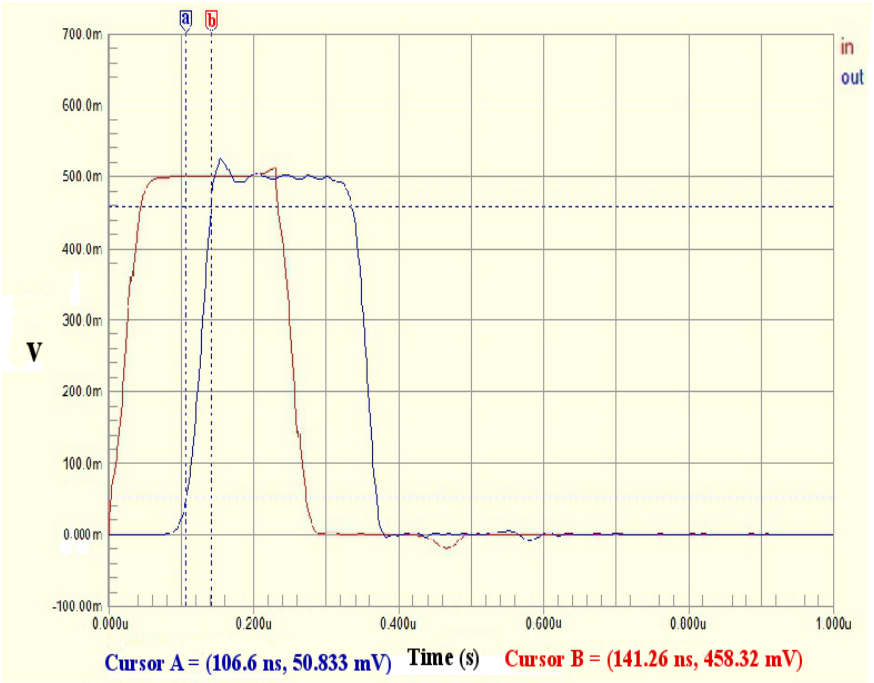

Figure B.4: The output signal of the designed delay line, which shows a rise time of 35 ns respect to the input signal.

($t_{without-cap}$). The first value ($t_{with-cap}$) is the ringing period without capacitor the second one ($t_{with-cap}$) is the ringing period with the capacitor. Both values should be recorded and the value of C_{add} is considered as value for capacitor, which must be added in the passive network in the simulation. The parasitic capacitance $C_{parasitic}$ and parasitic inductance $L_{parasitic}$ are responsible for the ringing and they are calculated by the following equation:

$$C_{parasitic} = \frac{C_{add}}{(\frac{t_{with-cap}}{t_{without-cap}})^2 - 1} - \ Scope\ probe\ capacitance\ (usually\ 10\,pF) \tag{B.8}$$

$$L_{parasitic} = \frac{1}{C_{parasitic} \times [2 \times PI \times F_{orig}]^2} \tag{B.9}$$

Firstly, F_{orig} should be calculated in order to have the value $L_{parasitic}$. The original parasitic ringing frequency is calculated from:

$$F_{orig} = \frac{1}{t_{without-cap}} \tag{B.10}$$

The circuit inductance and characteristic impedance (Ro) of the LC circuit are calculated from Eq. B.9 and Eq. B.11, respectively.

$$Ro = \sqrt{\frac{L_{parasitic}}{C_{parasitic}}} \tag{B.11}$$

The aforementioned procedure was followed and the values of F_{orig}, C_{add} were calculations for the LC ringing. Then they were implemented in the simulation. The results, which have been illustrated in Figure B.3 and Figure B.4 show that the existed LC ringing was reduced to an accepted level (The LC ringing of a level of 30 - 40 mV of amplitude respect to plateau is seen in the simulation results). Figure 5 and Figure 6 show the input and output signals after passing the delay line. The obtained results (output signal after the delay with values of 35-36 ns for rise time and a delay length of 100-105 ns) satisfied our expectation. Moreover, Figure B.5 shows a measurement which was done with a delay line (with rise time of 35-40 ns and the delay length of 100 ns). Figure B.6, illustrates the result, which was achieved by the constructed filter. The applied solution was precise and the values of inductances and capacitors obtained by the formulas and they removed major part of ringing in order to extend the frequency bandwidth of input signal.

The rationale for using Voltage Level Translator

Due to the complexity that is faced for the PET electronic system, we shift to lower voltage logic instead of using standard for logic circuits (TTL and 5V CMOS), which in turn can cause incompatibility between input and output levels for the logic families within our system. For instance, in our case, the digital section of acquisition system operates at 3.3 V and must communicate with the analog subsection of detection module, which operates at 5 V. Hence, translation between different domains of logic voltage is needed (Figure B.7).

Also, the applied digital ICs's features like:

- Incompatible voltage rails for V_{CORE} and V I/O,
- Lower V_{DD} rails for V_{CORE} and V I/O,

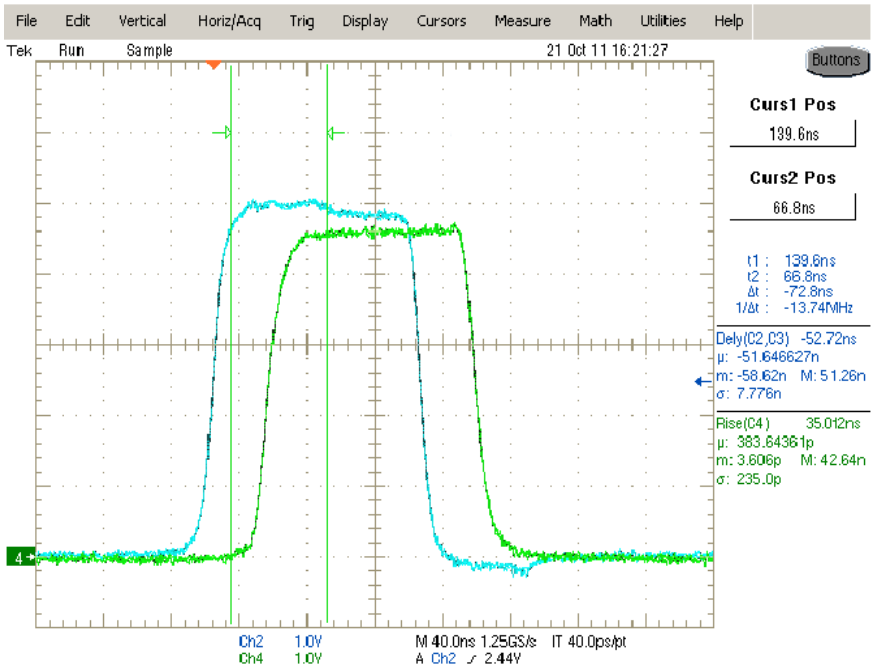

Figure B.5: The output signal of a delay line, which delays the signal with a length of 30 ns and with a rise time of 35 ns respect to the input signal.

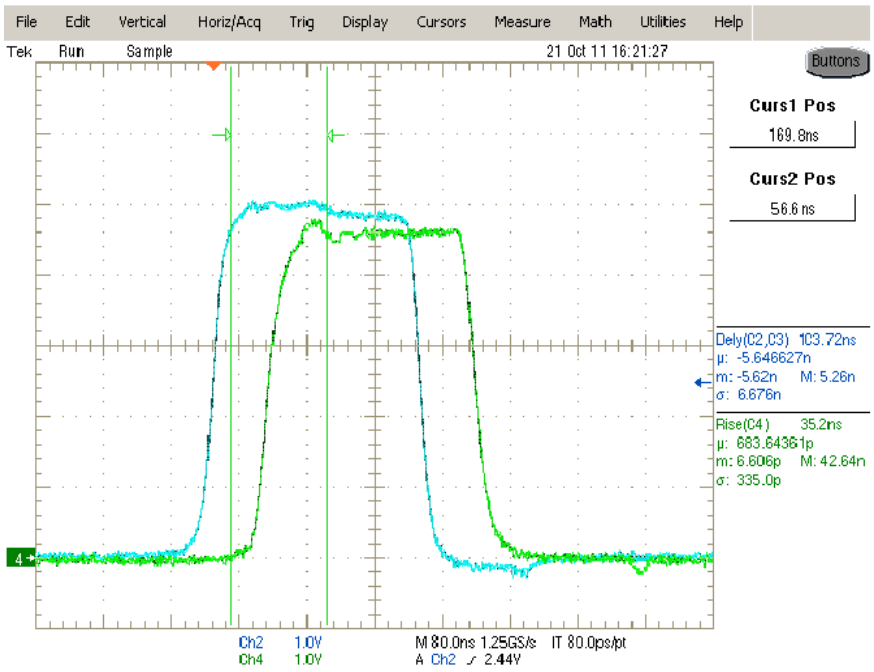

Figure B.6: The output signal of the designed delay line, which delays the signal with a length of 103 ns and with a rise time of 35.2 ns respect to the input signal.

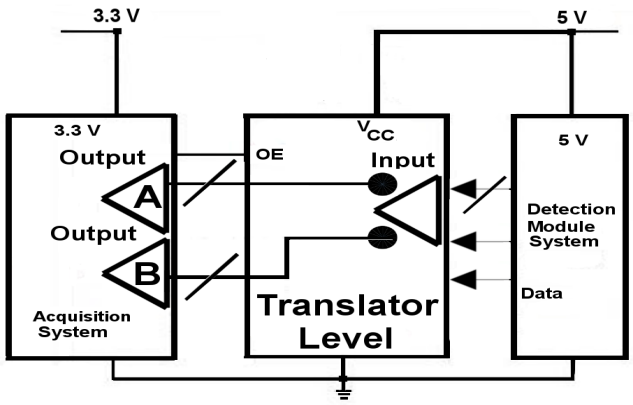

Figure B.7: Voltage level translation of digital section of the DoPET acquisition system, which operates as a block at 3.3 V communicate with an analog subsection of the module detection, which operates as a block at 5 V.

- Dual rails for for V_{CORE} and V I/O,
- The use of mixed-signal ICs with lower supply voltages that have not kept pace with those of their digital counterparts

have created the need for logic-level translation.

The architecture design of Translator for DoPET (9 Vs. 9)

Translation methods vary according to the range of voltages encountered the number of lines to be translated, and the speed of the digital signals and the parasitic capacitance inherent in these methods can reduce the data-transfer rate.

The applied structure for the translator level requires a component that can translate between any two logic levels at any speed. In our case, the applied logic ICs has the capability to translate from the low voltage level of 3.3 V to high level of voltage level of 5V.

In the designing the voltage level translator, the main utilized component was SY100E116. The Figure B.8 illustrates the pinout of SY100E116, which is quint differential line receiver that designed for use in new, high-performance ECL systems. This device have emitter-follower outputs and an internally generated reference supply (VBB) for single ended reception.

Table B.1: The functional pin of SY100E116

Pin	Function
D0, $\bar{D}$0-D4, $\bar{D}$4	Differential Input Pairs
Q0, $\bar{Q}$0-Q4, $\bar{Q}$4	Differential Output Pairs
VBB	Reference Voltage Output
VCCO	VCC to Output

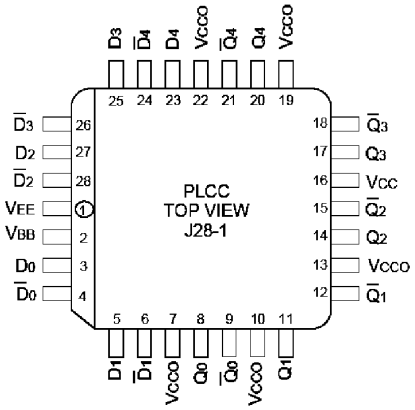

Figure B.8: The applied Quint Differential Line Receiver for designing of the DoPET voltage translator level.

This Line receiver has some characteristics which are listed in the following:

- Propagation Delay of maximum 450 ps,
- Extended 100E VEE range of -4.2 V to -5.5 V,
- VBB output for single-ended reception (which is intended for use as a reference voltage for single-ended reception of ECL signals to that device only.),
- Fully compatible with industry standard 10 KH, 100 K I/O level,
- Internal 75 KΩ input pull-down resistors

The functionality of its' pin has been illustrated in Table B.1.

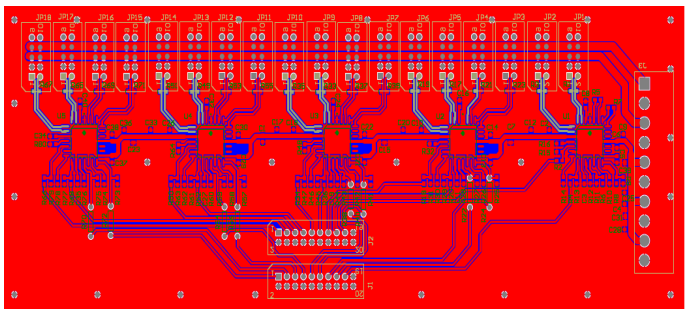

Figure B.9: The designed Voltage Level Translator for the DoPET when each head of the PET has 9 module of detection (9 PMTs).

Figure B.10 illustrates the translator voltage level board that was constructed.

We decided 5 number of SY100E116 components (quint differential line receiver) in order to simplify the designation of the translator board and to be sure that the introduced delay for each channel (module of the detection) are similar. This also could be a good choice to reduce the problem of cross-talk, because for each chip we have only four signals that are coming from each head of DoPET and in this way the consumed current decreases and reducing of the electronic noise source is feasible.

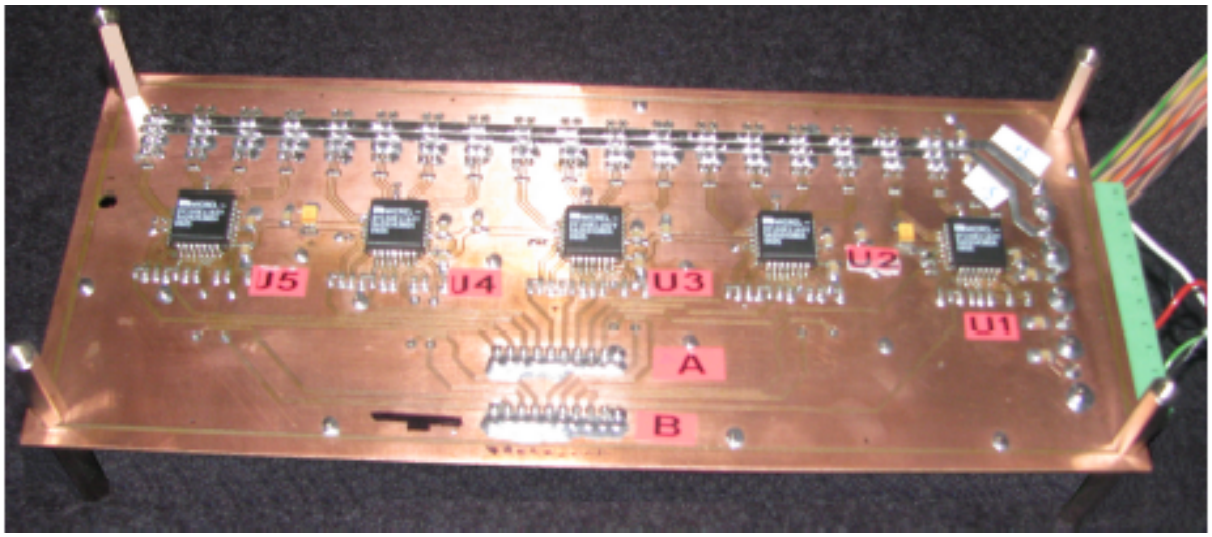

Figure B.10: The digital outputs, which come from the CFDs of each head of DoPET.

Checking output of the translator board

The next step after constructing new voltage level translator board was to check its performance. Hence, the detection module of the two head of DoPET was set up according to the figure of section 6.3.6 and the digital signal from CFD of each detector in each head was acquired. Figure B.11, illustrated the output that was acquired on oscilloscope. As it is seen the out put was satisfactory and the translator board was well done.

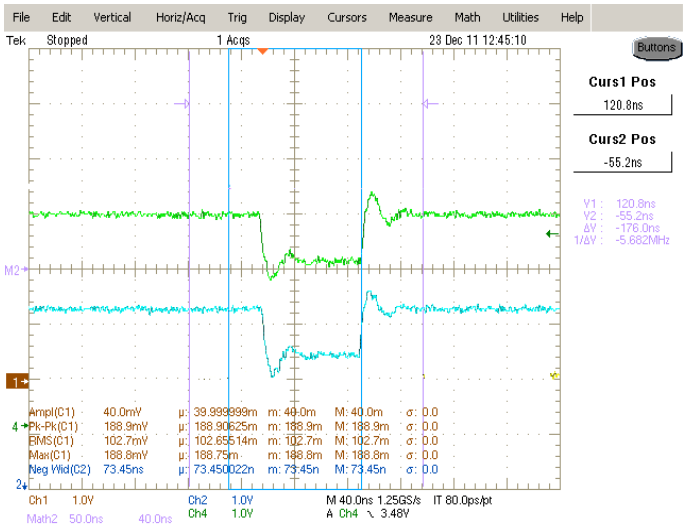

Figure B.11: The digital outputs, which come from the CFDs of each head of DoPET.

Appendix C

Part of ideas for events estimation in the block of CFD

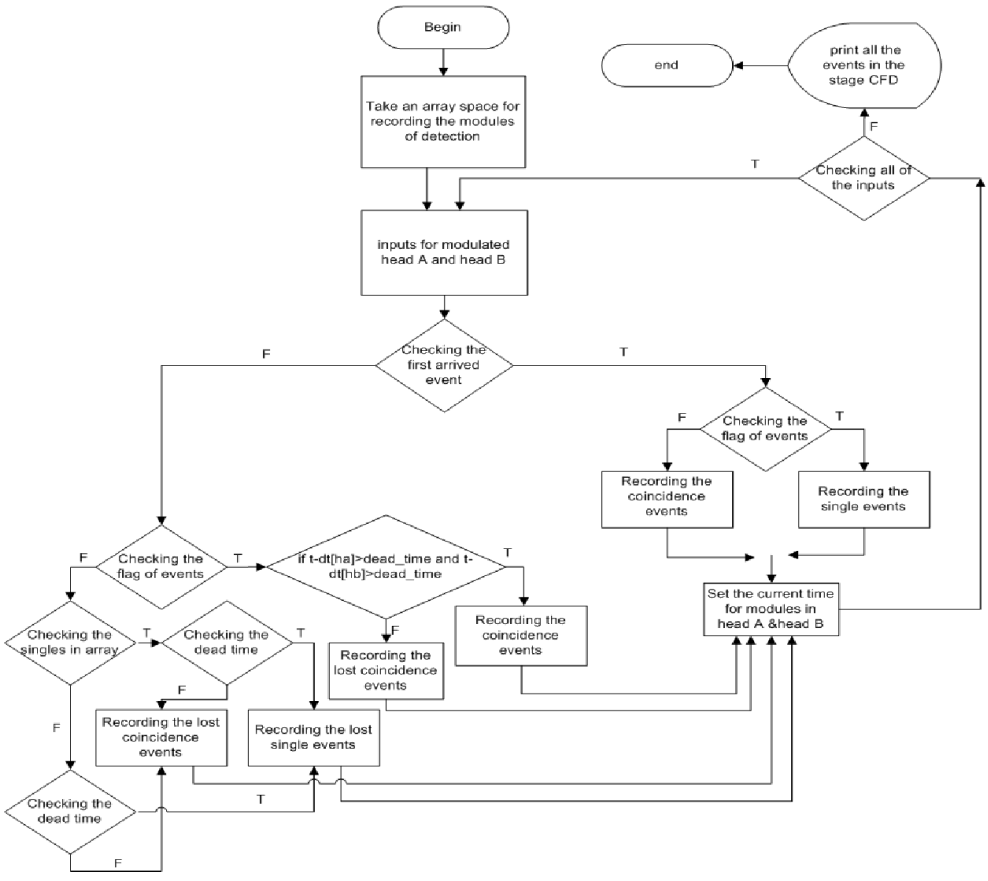

Figure C.1: Part of the idea that has been done to estimate the coincidence and single events, which are passing CFD board “Paralyzed-Modularized Block” as a part of the acquisition system of DoPET.

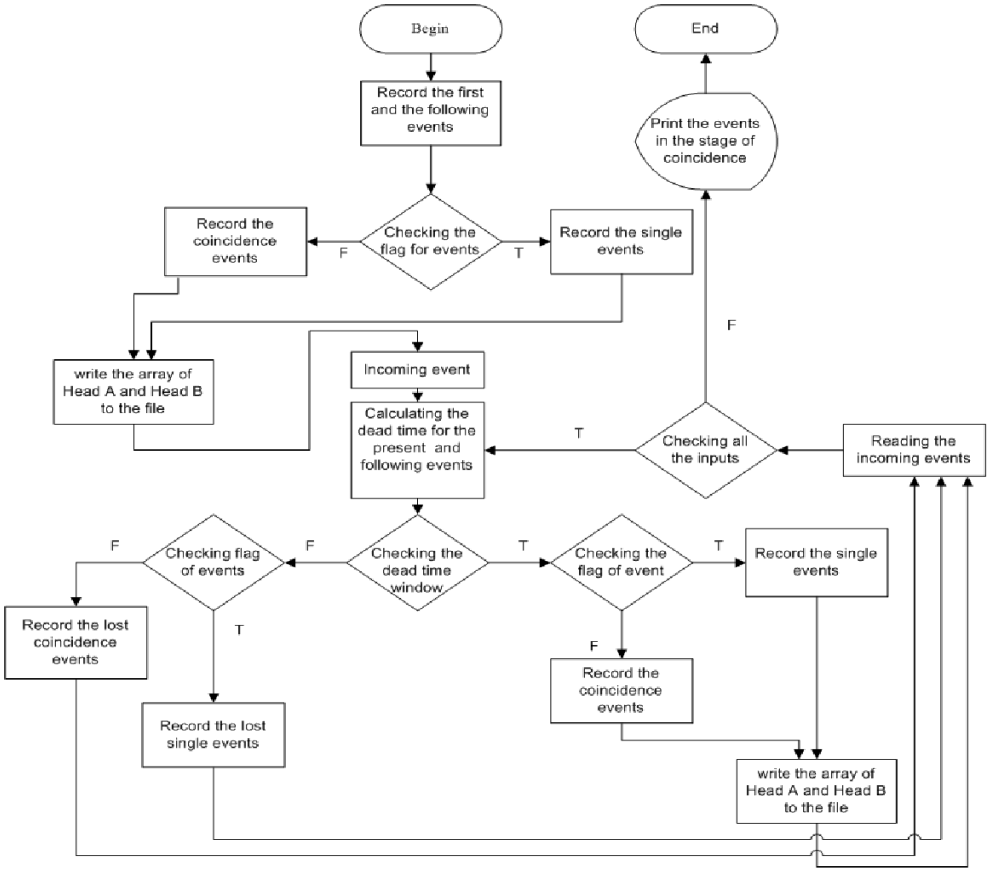

Figure C.2: Part of the idea that has been done to estimate the coincidence and single events, which are passing coincidence module “Paralyzed-Centralized Block” as a part of the acquisition system of DoPET.

Part of ideas for events estimation in the block of COINCIDENCE

Part of ideas for events estimation in the block of DAQ

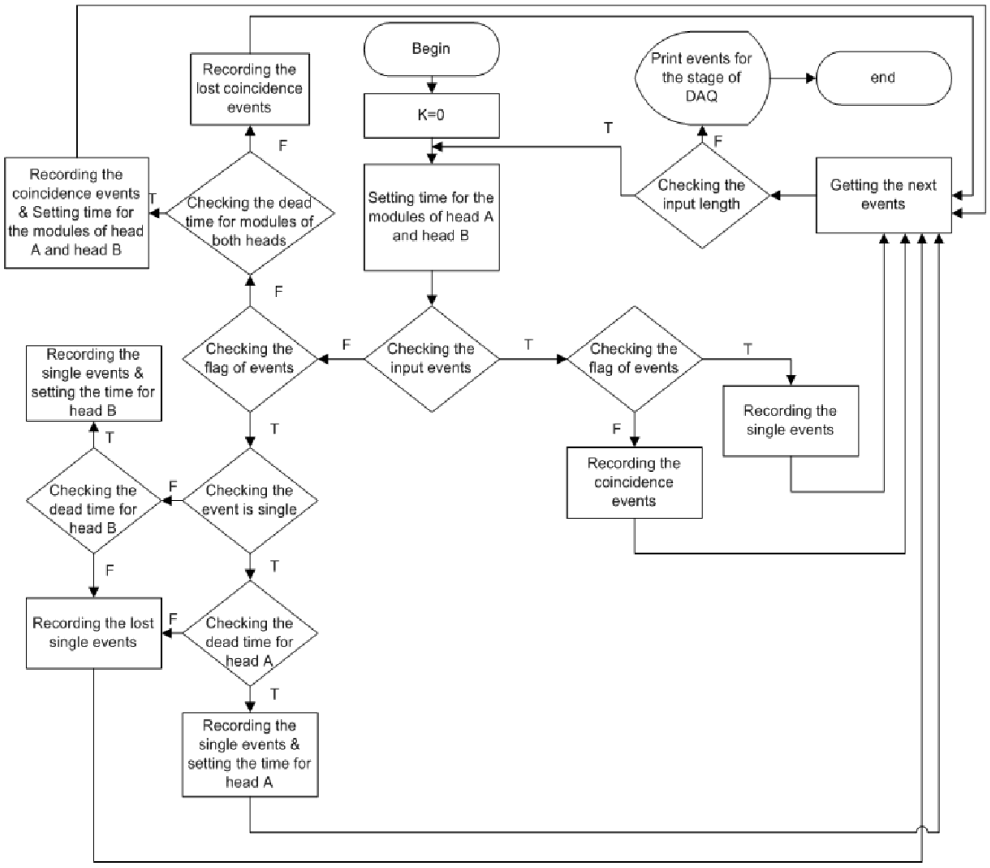

Figure C.3: Part of the idea that has been done to estimate the coincidence and single events, which are passing DAQ board “Non-Paralyzed-Modularized Block” as a part of the acquisition system of DoPET.

Bibliography

[1] E. S. Gragoudas, M. Goitein, A. Koehler, et al. Proton beam irradiation of choroidal melanomas. *Arch Ophthalmol*, 96:1583–1591, 1978.

[2] M. M. Austin-Seymour, S. S. Donaldson, P. R. Egbert, I. R. McDougall, and J. P. Kriss. Radiotherapy of lymphoid diseases of the orbit. *International Journal of Radiation Oncology-Biology-Physics*, 11(2):371–379, February 1985.

[3] J. P. Pignol, L. Meyer, A. Methlin, J. P. Wagner, J. C. Abbe, and J. Sahel. [Radiotherapy of ocular melanoma: physical and radiobiological bases, current techniques and future prospects]. *Bulletin Du Cancer. Radiothérapie: Journal De La Société Française Du Cancer: Organe De La Société Française De Radiothérapie Oncologique*, 81(2):127–142, 1994. PMID: 7702893.

[4] A. Courdi, J. P. Caujolle, J. D. Grange, L. Diallo-Rosier, J. Sahel, F. Bacin, C. Zur, P. Gastaud, N. Iborra-Brassart, J. Hérault, and P. Chauvel. Results of proton therapy of uveal melanomas treated in nice. *International Journal of Radiation Oncology-Biology-Physics*, 45(1):5–11, August 1999.

[5] J. E. Munzenrider. Uveal Melanomas: conservation treatment. *Hematology/Oncology Clinics of North America*, 15(2):389–402, April 2001.

[6] L. Desjardins, L. Lumbroso, C. Levy, A. Mazal, S. Delacroix, J. C. Rosenwald, R. Dendale, C. Plancher, and B. Asselain. Treatment of uveal melanoma with iodine 125 plaques or proton beam therapy: indications and comparison of local recurrence rates. *Journal Français D'ophtalmologie*, 26(3):269–276, March 2003. PMID: 12746603.

[7] B. Damato, A. Kacperek, M. Chopra, M. A. Sheen, I. R. Campbell, and R. D. Errington. Proton beam radiotherapy of iris melanoma. *International Journal of Radiation Oncology-Biology-Physics*, 63(1):109–115, September 2005.

[8] B. Damato, A. Kacperek, M. Chopra, I. R. Campbell, and R. D. Errington. Proton beam radiotherapy of choroidal melanoma: The Liverpool-Clatterbridge experience. *International Journal of Radiation Oncology-Biology-Physics*, 62(5):1405–1411, August 2005.

[9] D. W. Miller. A review of proton beam radiation therapy. *Medical Physics*, 22(11):1943–1954, 1995.

[10] U. Amaldi and G. Kraft. Radiotherapy with beams of carbon ions. *Reports on Progress in Physics*, 68(8):1861–1882, 2005.

[11] K. Parodi, H. Paganetti, H. A. Shih, S. Michaud, J. S. Loeffler, T. F. DeLaney, N. J. Liebsch, John E. Munzenrider, Alan J. Fischman, Antje Knopf, and Thomas Bortfeld. Patient study of in vivo verification of beam delivery and range, using positron emission tomography and computed tomography imaging after proton therapy. *International Journal of Radiation Oncology-Biology-Physics*, 68(3):920–934, July 2007.

[12] W. Enghardt, P. Crespo, F. Fiedler, R. Hinz, K. Parodi, J. Pawelke, and F. Pönisch. Charged hadron tumour therapy monitoring by means of PET. *Nuclear Instruments and Methods in Physics Research Section A: Accelerators, Spectrometers, Detectors and Associated Equipment*, 525(1-2):284–288, June 2004.

[13] A. Knopf, K. Parodi, T. Bortfeld, H. A. Shih, and H. Paganetti. Systematic analysis of biological and physical limitations of proton beam range verification with offline PET/CT scans. *Physics in Medicine and Biology*, 54(14):4477–4495, 2009.

[14] H. Mizuno, T. Tomitani, M. Kanazawa, A. Kitagawa, J. Pawelke, Y. Iseki, E. Urakabe, M. Suda, A. Kawano, R. Iritani, S. Matsushita, T. Inaniwa, T. Nishio, S. Furukawa, K. Ando, Y. K. Nakamura, T. Kanai, and K. Ishii. Washout measurement of radioisotope implanted by radioactive beams in the rabbit. *Physics in Medicine and Biology*, 48(15):2269–2281, 2003.

[15] W. Enghardt, J. Debus, T. Haberer, B.G. Hasch, R. Hinz, O. Jäkel, M. Krämer, K. Lauckner, J. Pawelke, and F. Pönisch. The routine PET monitoring of tumor therapy with ^{12}C ions. *Forschungszentrum Rossendorf Annual Report FZR-271*, pages 89–90, July 1999.

[16] K. Parodi, W. Enghardt, and T. Haberer. In-beam PET measurements of β + radioactivity induced by proton beams. *Physics in Medicine and Biology*, 47(1):21–36, 2002.

[17] F. Attanasi, N. Belcari, A. Del Guerra, W. Enghardt, S. Moehrs, K. Parodi, V. Rosso, and S. Vecchio. Comparison of two dedicated In-Beam PET systems via simultaneous imaging of ^{12}C-induced β-activity. *Physics in Medicine and Biology*, 54(2):N29–N35, 2009.

[18] C. Agodi, A. Antoccia, F. Attanasi, A. Attili, G. Battistoni, F. Berardinelli, F. Bourhaleb, R. Cherubini, R. Cirio, G. A. P. Cirrone, et al. The INFN TPS project. *Nuovo Cimento C Geophysics Space Physics C*, 31:99–108, 2008.

[19] M. Dosanjh et al. Development of hadron therapy for cancer treatment in europe. In *Medical Physics(AIP Conference Proceedings Volume 1032)*, volume 1032, pages 12–16, 2008.

[20] U. Amaldi. The importance of particle accelerators. *europhysics news*, 31(6):5–9, 2000.

[21] E. J. Hall and A. J. Giaccia. *Radiobiology for the radiologist*. Lippincott Williams & Wilkins, 2006.

[22] A. J Lomax. Charged particle therapy: the physics of interaction. *The Cancer Journal*, 15(4):285–291, 2009.

[23] J. J Coen and A. L Zietman. Proton radiation for localized prostate cancer. *Nature Reviews Urology*, 6(6):324–330, 2009.

[24] M. Goitein. Radiation oncology: a physicist's-eye view. *Radiation Oncology: A Physicist's-Eye View, by Michael Goitein. Berlin: Springer, 2008. ISBN 978-0-387-72644-1*, 1, 2008.

[25] E Pedroni, S Scheib, T BÃűhringer, A Coray, M Grossmann, S Lin, and A Lomax. Experimental characterization and physical modelling of the dose distribution of scanned proton pencil beams. *Physics in Medicine and Biology*, 50(3):541–561, 2005.

[26] O. Jäkel. Medical physics aspects of particle therapy. *Radiation protection dosimetry*, 137(1-2):156–166, 2009.

[27] G. Kraft. Tumor therapy with heavy charged particles. *Progress in Particle and Nuclear Physics*, 45(Supplement 2):S473–S544, 2000.

[28] G. Kraft. The radiobiological and physical basis for radiotherapy with protons and heavier ions. *Strahlentherapie Und Onkologie: Organ Der Deutschen Röntgengesellschaft ... et al*, 166(1):10–13, January 1990. PMID: 2154042.

[29] R. R. Wilson et al. Radiological use of fast protons. *Radiology*, 47(5):487–491, 1946.

[30] B. Larsson. *On The application of A 185 Mev proton beam to experimental cancer therapy and neurosurgery. a biophysical study*. December 1962.

[31] Wilson. *A brief history of the Harvard University cyclotrons*. Harvard Univ., Cambridge, MA, 2004.

[32] B. Larsson, L. Leksell, B. Rexed, P. Sourander, W. Mair, and B. Andersson. The High-Energy proton beam as a neurosurgical tool. *Nature*, 182(4644):1222–1223, November 1958.

[33] History of proton beam therapy. *Synthesis*, 9(2), 2006.

[34] American Cancer Society. *Cancer facts & figures*. The Society, 2008.

[35] P. A Vieira Crespo. *Optimization of In-Beam Positron Emission Tomography for Monitoring Heavy Ion Tumor Therapy*. PhD thesis, TU Darmstadt, 2006.

[36] M. Garcia, A. Jemal, E. M. Ward, M. M. Center, Y. Hao, R. L. Siegel, and M. J. Thun. Global cancer facts & figures 2007. *Atlanta, GA: American Cancer Society*, 1(3), 2007.

[37] H. Bethe. Zur theorie des durchgangs schneller korpuskularstrahlen durch materie. *Annalen der Physik*, 397(3):325–400, 1930.

[38] F. Bloch. Bremsvermogen von atomen mit mehreren elektronen. *Zeitschrift fur Physik*, 81(5-6):363–376, 1933.

[39] F. Bloch. Zur bremsung rasch bewegter teilchen beim durchgang durch materie. *Annalen der Physik*, 408(3):285–320, 1933.

[40] W. H. Barkas. Nuclear research emulsions. vol.1: Techniques and theory. http://adsabs.harvard.edu/abs/1963nre..book.....B, 1963.

[41] G. Moliere. Single scattering in a screened coulomb® eld: Theory of scattering of fast charged particles. *Z. Naturforsch., A*, 2:133–145, 1947.

[42] B. Gottschalk, A. M. Koehler, R. J. Schneider, J. M. Sisterson, and M. S. Wagner. Multiple coulomb scattering of 160 MeV protons. *Nuclear Instruments and Methods in Physics Research Section B: Beam Interactions with Materials and Atoms*, 74(4):467–490, June 1993.

[43] L. J. Verhey and J. E. Munzenrider. Proton beam therapy. *Annual Review of Biophysics and Bioengineering*, 11(1):331–357, 1982.

[44] Raju. *Heavy particle radiotherapy*. Academic Press, New York, NY, 1980.

[45] D. J. Cole. The case of proton therapy in the UK. *Private communication to AEA*, 1990.

[46] G. Kantor, B. Destembert, N. Breteau, and M. Sclienger. Les protons en radiothérapie: avantages théoriques et applications médicales= proton beam therapy: theoretical advantages and medical applications. *Gazette médicale de France*, 92(18):101–103, 1985.

[47] S. Webb. *The physics of three-dimensional radiation therapy: conformal radiotherapy, radiosurgery, and treatment planning*. Taylor & Francis, 1993.

[48] H. Bichsel. *Passage of charged particles through matter*. 3rd ed., sec. 8d edition, 1968.

[49] V. L. Highland. Some practical remarks on multiple scattering. *Nuclear Instruments and Methods*, 129(2):497–499, November 1975.

[50] W. T. Chu, B. A. Ludewigt, and T. R. Renner. Instrumentation for treatment of cancer using proton and light-ion beams. *Review of Scientific Instruments*, 64(8):2055–2122, 1993.

[51] A. M. Koehler, R. J. Schneider, and J. M. Sisterson. Range modulators for protons and heavy ions. *Nuclear Instruments and Methods*, 131(3):437–440, December 1975.

[52] H. M. Kooy, M. Schaefer, S. Rosenthal, and T. Bortfeld. Monitor unit calculations for range-modulated spread-out bragg peak fields. *Physics in Medicine, Biology*, 48(17):2797–2808, 2003.

[53] M. Urie, M. Goitein, W. R. Holley, and G. T. Y. Chen. Degradation of the bragg peak due to inhomogeneities. *Physics in Medicine and Biology*, 31(1):1–15, 1986.

[54] E. A. Blakely. New measurements for hadrontherapy and space radiation: Biology. *Physica Medica*, 17:50–58, 2001.

[55] W. Schimmerling, J. Miller, M. Wong, M. Rapkin, J. Howard, H. G. Spieler, and B. V. Jarret. The fragmentation of 670A MeV neon-20 as a function of depth in water: I. experiment. *Radiation research*, 120(1):36–71, 1989.

[56] R. Kaufmann and R. Wolfgang. Nucleon transfer reactions in grazing collisions of heavy ions. *Physical Review*, 121(1):192–205, January 1961.

[57] R. Kaufmann and R. Wolfgang. Single-Nucleon transfer reactions of ^{19}F, ^{16}O, ^{14}N, and ^{12}C. *Physical Review*, 121(1):206–208, January 1961.

[58] C. A. Tobias, J. T. Lyman, and J. H. Lawrence. *Some consideration of physical and biological factors in radiotherapy with high-LET radiations including heavy particles, pi mesons, and fast neutrons.* Progr. Atomic Med., December 1971.

[59] H. H. Heckman, D. E. Greiner, P. J. Lindstrom, and F. S. Bisser. Fragmentation of nitrogen-14 nuclei at 2.1 gev per nucleon. *Science (New York, N.Y.)*, 174(4014):1130–1131, December 1971. PMID: 17779401.

[60] H. D. MacCabee. Composition of High-Energy Heavy-Ion beams: Preliminary measurements. *Radiation Research*, 54(3):495–509, June 1973.

[61] A. Wambersie. The future of high-LET radiation in cancer therapy. In *Chauvel P. and Wambersie A., Eulima Workshop on the Potential Value of Light Ion Beam Therapy, Publication No. EUR*, volume 12165, 1989.

[62] G. Kraft, U. Amaldi, B. Larsson, and Y. Lemoigne. *Advances in hadrontherapy*. Excerpta Medica, Int. Congr. Series 1144, Elsevier, 1997.

[63] J. L. Habrand, P. Schlienger, L. Schwartz, D. Pontvert, C. Lenir-Cohen-Solal, S. Helfre, C. Haie, A. Mazal, and J. M. Cosset. Clinical applications of proton therapy. *Radiation and Environmental Biophysics*, 34(1):41–44, 1995.

[64] J. L. Habrand, L. Desjardins, H. Mammar, and A. Mazal. [Protontherapy. clinical features]. *Bulletin Du Cancer. Radiothérapie: Journal De La Société Française Du Cancer: Organe De La Société Française De Radiothérapie Oncologique*, 83(4):247–253, 1996. PMID: 9081322.

[65] J. S. Loeffler, A. R. Smith, and H. D. Suit. The potential role of proton beams in radiation oncology. *Seminars in Oncology*, 24(6):686–695, December 1997. PMID: 9422264.

[66] M. Krengli, N. J. Liebsch, E.B. Hug, and R. Orecchia. Review of current protocols for protontherapy in USA. *Tumori*, 84(2):209–216, 1998.

[67] B. Glimelius, A. Ask, G. Bjelkengren, T. Björk-Eriksson, E. Blomquist, B. Johansson, M. Karlsson, and B. Zackrisson. Number of patients potentially eligible for proton therapy. *Acta Oncologica*, 44(8):836–849, 2005.

[68] J. Lundkvist, M. Ekman, S. R. Ericsson, B. Jönsson, and B. Glimelius. Proton therapy of cancer: potential clinical advantages and cost-effectiveness. *Acta oncologica*, 44(8):850–861, 2005.

[69] M. M. Austin-Seymour, J. E. Munzenrider, M. Goitein, R. Gentry, E. Gragoudas, A. M Koehler, P. McNulty, D. K Ryugo E. Osborne, and J. Seddon. Progress in low-LET heavy particle therapy: intracranial and paracranial tumors and uveal melanomas. *Radiation Research*, 104(2):219–226, 1985.

[70] A. Mazal, L. Schwartz, F. Lacroix, H. Mammar, S. Delacroix, R. Ferrand, C. Nauraye, L. Desjardins, P. Schlienger, F. D'Hermies, E. Frau, J. L. Habrand, and J. C. Rosenwald. A preliminary comparative treatment planning study for radiotherapy of age-related maculopathy. *Radiotherapy and Oncology*, 47(1):91–98, April 1998.

[71] C. A. Tobias. Pretherapeutic investigations with accelerated heavy ions. *Radiology*, 108(1):145–158, July 1973. PMID: 4196728.

[72] L. E. Antonuk. Electronic portal imaging devices: a review and historical perspective of contemporary technologies and research. *Physics in Medicine and Biology*, 47(6):R31–R65, 2002.

[73] G. T. Y. Chen, R. P. Singh, J. R. Castro, J. T. Lyman, and J. M. Quivey. Treatment planning for heavy ion radiotherapy. *International Journal of Radiation Oncology-Biology-Physics*, 5(10):1809–1819, October 1979.

[74] B. Schaffner and E. Pedroni. The precision of proton range calculations in proton radiotherapy treatment planning: experimental verification of the relation between CT-HU and proton stopping power. *Physics in Medicine and Biology*, 43(6):1579–1592, 1998.

[75] M. Krämer, O. Jäkel, T. Haberer, G. Kraft, D. Schardt, and U. Weber. Treatment planning for heavy-ion radiotherapy: physical beam model and dose optimization. *Physics in Medicine and Biology*, 45(11):3299–3317, 2000.

[76] O. Jäkel, M. Krämer, C. P. Karger, and J. Debus. Treatment planning for heavy ion radiotherapy: clinical implementation and application. *Physics in Medicine and Biology*, 46(4):1101–1116, 2001.

[77] G. W. Bennett, J. O. Archambeau, B. E. Archambeau, J. I. Meltzer, and C. L. Wingate. Visualization, transport of positron emission from proton activation in vivo. *Science*, 200(4346):1151–1153, June 1978.

[78] J. Llacer. Positron emission medical measurements with accelerated radioactive ion beams. *Nucl. Sci. Appl*, 3:111–131, 1988.

[79] S. Vynckier, S. Derreumaux, F. Richard, A. Bol, C. Michel, and A. Wambersie. Is it possible to verify directly a proton-treatment plan using positron emission tomography? *Radiotherapy, Oncology*, 26(3):275–277, March 1993.

[80] A. M. J. Paans and J. M. Schippers. Proton therapy in combination with PET as monitor: a feasibility study. *Nuclear Science, IEEE Transactions on*, 40(4):1041–1044, 1993.

[81] K. Yoshikawa et al. The initial imaging of ^{12}C distribution yielded by auto activation of ^{12}C beams in the heavy ion therapy. *J. Nucl. Med. Technol*, 24:167–168, 1996.

[82] U. Oelfke, G. K. Y. Lam, and M. S. Atkins. Proton dose monitoring with PET: quantitative studies in lucite. *Physics in Medicine and Biology*, 41(1):177–196, 1996.

[83] Y. Matsuzaki, H. Date, K. L Sutherland, and Y. Kiyanagi. Nuclear collision processes around the bragg peak in proton therapy. *Radiological Physics and Technology*, 3(1):84–92, 2010.

[84] M Moteabbed, S EspaÃśa, and H Paganetti. Monte carlo patient study on the comparison of prompt gamma and PET imaging for range verification in proton therapy. *Physics in Medicine and Biology*, 56(4):1063–1082, 2011.

[85] Chul-Hee Min, Chan Hyeong Kim, Min-Young Youn, and Jong-Won Kim. Prompt gamma measurements for locating the dose falloff region in the proton therapy. *Applied Physics Letters*, 89(18):183517–1–183517–4, 2006.

[86] C. H. Min, J. W. Kim, M. Y. Youn, and C. H. Kim. Determination of distal dose edge location by measuring right-angled prompt-gamma rays from a 38 MeV proton beam. *Nuclear Instruments and Methods in Physics Research Section A: Accelerators, Spectrometers, Detectors and Associated Equipment*, 580(1):562–565, 2007.

[87] V. Bom, L. Joulaeizadeh, and F. Beekman. Real-time prompt gamma monitoring in spot-scanning proton therapy using imaging through a knife-edge-shaped slit. *Physics in Medicine and Biology*, 57(1).

[88] Chul Hee Min, Han Rim Lee, Chan Hyeong Kim, and Se Byeong Lee. Development of array-type prompt gamma measurement system for in vivo range verification in proton therapy. *Medical Physics*, 39(4):2100–2107, 2012.

[89] W. Enghardt, W. D. Fromm, H. Geissel, H. Heller, G. Kraft, A. Magel, P. Manfrass, G. Munzenberg, F. Nickel, J. Pawelke, et al. The spatial distribution of positron-emitting nuclei generated by relativistic light ion beams in organic matter. *Physics in Medicine and Biology*, 37(11):2127–2131, 1992.

[90] Michela Lecchi, Piero Fossati, Federica Elisei, Roberto Orecchia, and Giovanni Lucignani. Current concepts on imaging in radiotherapy. *European Journal of Nuclear Medicine and Molecular Imaging*, 35(4):821–837, 2008.

[91] P. Crespo, T. Barthel, H. Frais-Kolbl, E. Griesmayer, K. Heidel, K. Parodi, J. P Pawelke, and W. Enghardt. Suppression of random coincidences during In-Beam PET measurements at ion beam radiotherapy facilities. *IEEE Transactions on Nuclear Science*, 52(4):980–987, 2005.

[92] G. Lucignani. Aptamers and in-beam PET for advanced diagnosis and therapy optimisation. *European journal of nuclear medicine and molecular imaging*, 33(9):1095–1097, 2006.

[93] J. Pawelke, L. Byars, W. Enghardt, W. D. Fromm, H. Geissel, B. G. Hasch, K. Lauckner, P. Manfrass, D. Schardt, and M. Sobiella. The investigation of different cameras for In-beam PET imaging. *Physics in Medicine and Biology*, 41(2):279–296, 1996.

[94] P. Crespo, G. Shakirin, and W. Enghardt. On the detector arrangement for In-beam PET for hadron therapy monitoring. *Physics in Medicine and Biology*, 51(9):2143–2163, 2006.

[95] W. Enghardt, J. Debus, T. Haberer, B.G. Hasch, R. Hinz, O. Jäkel, M. Krämer, K. Lauckner, J. Pawelke, and F. Pönisch. Positron emission tomography for quality assurance of cancer therapy with light ion beams. *Nuclear Physics A*, 654(1, Supplement 1):1047c–1050c, July 1999.

[96] K. Parodi. *On the feasibility of dose quantification with In-beam PET data in radiotherapy with* ^{12}C *and proton beams*. Forschungszentrum, 2004.

[97] H. Müller and W Enghardt. In-beam PET at high-energy photon beams: a feasibility study. *Physics in Medicine and Biology*, 51(7):1779–1789, 2006.

[98] Falk Pönisch, K. Parodi, B. G. Hasch, and W. Enghardt. The modelling of positron emitter production and PET imaging during carbon ion therapy. *Physics in Medicine and Biology*, 49(23):5217–5232, 2004.

[99] Y. Hishikawa, K. Kagawa, M. Murakami, H. Sakai, T. Akagi, and M. Abe. Usefulness of positron-emission tomographic images after proton therapy. *International Journal of Radiation Oncology-Biology-Physics*, 53(5):1388–1391, August 2002.

[100] Y. Iseki, H. Mizuno, Y. Futami, T. Tomitani, T. Kanai, M. Kanazawa, A. Kitagawa, T. Murakami, T. Nishio, M. Suda, E. Urakabe, A. Yunoki, and H. Sakai. Positron camera for range verification of heavy-ion radiotherapy. *Nuclear Instruments and Methods in Physics Research Section A: Accelerators, Spectrometers, Detectors and Associated Equipment*, 515(3):840–849, December 2003.

[101] T. Nishio, T. Ogino, K. Nomura, and H. Uchida. Dose-volume delivery guided proton therapy using beam on-line PET system. *Medical Physics*, 33(11):4190–4197, 2006.

[102] K. Parodi, T. Bortfeld, W. Enghardt, F. Fiedler, A. Knopf, H. Paganetti, J. Pawelke, G. Shakirin, and H. Shih. PET imaging for treatment verification of ion therapy: Implementation and experience at GSI darmstadt and MGH boston. *Nuclear Instruments and Methods in Physics Research Section A: Accelerators, Spectrometers, Detectors and Associated Equipment*, 591(1):282–286, June 2008.

[103] D. W. Litzenberg, D. A. Roberts, M. Y. Lee, K. Pham, A. M. Vander Molen, R. Ronningen, and F. D. Becchetti. On-line monitoring of radiotherapy beams: Experimental results with proton beams. *Medical Physics*, 26(6):992–1006, 1999.

[104] T. Inaniwa, T. Tomitani, T. Kohno, and T. Kanai. Quantitative comparison of suitability of various beams for range monitoring with induced β+ activity in hadron therapy. *Physics in Medicine and Biology*, 50(6):1131–1145, 2005.

[105] F. Fiedler, P. Crespo, K. Parodi, M. Sellesk, and W. Enghardt. The feasibility of In-Beam PET for therapeutic beams of ^3He. *Nuclear Science, IEEE Transactions on*, 53(4):2252–2259, 2006.

[106] T. Inaniwa, T. Kohno, T. Tomitani, and S. Sato. Monitoring the irradiation field of ^{12}C and ^{16}O SOBP beams using positron emitters produced through projectile fragmentation reactions. *Physics in Medicine and Biology*, 53(3):529–542, 2008.

[107] D. Möckel, H. Müller, J. Pawelke, M. Sommer, E. Will, and W. Enghardt. Quantification of β + activity generated by hard photons by means of PET. *Physics in Medicine and Biology*, 52(9):2515–2530, 2007.

[108] F. Attanasi, N. Belcari, M. Camarda, G. A. P. Cirrone, G. Cuttone, A. Del Guerra, F. Di Rosa, N. Lanconelli, V. Rosso, G. Russo, and S. Vecchio. Preliminary results of an In-beam PET prototype for proton therapy. *Nuclear Instruments and Methods in Physics Research Section A: Accelerators, Spectrometers, Detectors and Associated Equipment*, 591(1):296–299, June 2008.

[109] S. Vecchio, F. Attanasi, N. Belcari, M. Camarda, G. A. P. Cirrone, G. Cuttone, F. Di Rosa, N. Lanconelli, S. Moehrs, and V. Rosso. A PET prototype for In-Beam monitoring of proton therapy. *Nuclear Science, IEEE Transactions on*, 56(1):51–56, 2009.

[110] S. Moehrs, M. Defrise, N. Belcari, A. Del Guerra, A. Bartoli, S. Fabbri, and G. Zanetti. Multi-ray-based system matrix generation for 3D PET reconstruction. *Physics in Medicine and Biology*, 53(23):6925–6945, 2008.

[111] M. E. Phelps. *PET: physics, instrumentation, and scanners*. Springer, 2006.

[112] W.W. Moses, P.R.G. Virador, S.E. Derenzo, R.H. Huesman, and T.F. Budinger. Design of a high-resolution, high-sensitivity PET camera for human brains and small animals. *Nuclear Science, IEEE Transactions on*, 44(4):1487 –1491, August 1997.

[113] D. L. Bailey, D. W. Townsend, P. E. Valk, and M. N. Maisey, editors. *Positron Emission Tomography*. Springer-Verlag, London, 2005.

[114] E. J Hoffman, S. C Huang, M. E Phelps, D. E Kuhl, et al. Quantitation in positron emission computed tomography: 4. effect of accidental coincidences. *Journal of computer assisted tomography*, 5(3):391, 1981.

[115] Margaret E Daube-Witherspoon, Joel S Karp, Michael E Casey, Frank P DiFilippo, Horace Hines, Gerd Muehllehner, Vilim Simcic, Charles W Stearns, Lars-Eric Adam, Steve Kohlmyer, and Vesna Sossi. PET performance measurements using the NEMA NU 2-2001 standard. *Journal of Nuclear Medicine*, 43(10):1398–1409, October 2002.

[116] K. Iniewski. *Electronics for radiation detection*. Taylor & Francis.

[117] H. Spieler. Fast timing methods for semiconductor detectors. *Nuclear Science, IEEE Transactions on*, 29(3):1142–1158, 1982.

[118] G. F. Knoll. *Radiation Detection and Measurement*. John Wiley, New York, 2000.

[119] H. Spieler. *Semiconductor detector systems*, volume 12. Oxford University Press, USA, 2005.

[120] G. B. Saha. *Basics of PET Imaging: Physics, Chemistry, and Regulations*. Springer, December 2010.

[121] D.L. Bailey, T. Jones, and T.J. Spinks. A method for measuring the absolute sensitivity of positron emission tomographic scanners. *European Journal of Nuclear Medicine and Molecular Imaging*, 18(6):374–379, 1991.

[122] National Electrical Manufacturers Association et al. NEMA standards publication NU 2-2001: performance measurements of positron emission tomographs. *Rosslyn, VA: National Electrical Manufacturers Association*, pages 26–33, 2001.

[123] D.L. Bailey and T. Jones. A method for calibrating three-dimensional positron emission tomography without scatter correction. *European Journal of Nuclear Medicine and Molecular Imaging*, 24(6):660–664, 1997.

[124] G. F. Knoll. Radiation detection and measurement, john wiley & sons. *Inc., New York*, 1999.

[125] M. E. Daube-Witherspoon and R. E. Carson. Unified deadtime correction model for PET. *Medical Imaging, IEEE Transactions on*, 10(3):267–275, 1991.

[126] L. Eriksson, K. Wienhard, and M. Dahlbom. A simple data loss model for positron camera systems. *Nuclear Science, IEEE Transactions on*, 41(4):156–1570, 1994.

[127] G. Germano and E. J Hoffman. Investigation of count rate and deadtime characteristics of a high resolution PET system. *Journal of computer assisted tomography*, 12(5):836–846, 1988.

[128] W. S. Diethorn. Counter deadtime: A question of poor textbook advice. *The International Journal of Applied Radiation and Isotopes*, 25(2):55–60, February 1974.

[129] S Janek, R Svensson, C Jonsson, and A Brahme. Development of dose delivery verification by PET imaging of photonuclear reactions following high energy photon therapy. *Physics in Medicine and Biology*, 51(22):5769–5783, November 2006.

[130] F. Attanasi, N. Belcari, S. Moehrs, V. Rosso, S. Vecchio, G. A. P. Cirrone, G. Cuttone, P. Lojacono, F. Romano, and N. Lanconelli. Characterization of an In-Beam PET prototype for proton therapy with different target compositions. *Nuclear Science, IEEE Transactions on*, 57(3):1563–1569, 2010.

[131] G. Sportelli, F. Attanasi, N. Belcari, G. Franchi, P. Guerra, S. Moehrs, V. Rosso, A. Santos, F. Spinella, and S. Vecchio. A flexible acquisition system for modular dual head positron emission mammography. In *Nuclear Science Symposium Conference Record (NSS/MIC), 2009 IEEE*, pages 3395–3398, 2009.

[132] G. Sportelli, N. Belcari, P. Guerra, and A. Santos. Low-resource synchronous coincidence processor for positron emission tomography. *Nuclear Instruments and Methods in Physics Research Section A: Accelerators, Spectrometers, Detectors and Associated Equipment*, In Press, Corrected Proof, 2010.

[133] N. Belcari, F. Attanasi, S. Moehrs, V. Rosso, A. Santos, F. Spinella, G. Sportelli, and A. Del Guerra. A novel random counts estimation method for PET using a symmetrical delayed window technique and random single event acquisition. In *Nuclear Science Symposium Conference Record (NSS/MIC), 2009 IEEE*, pages 3611–3614, 2010.

[134] P. D Olcott, J. A Talcott, C. S Levin, F. Habte, and A. M. K. Foudray. Compact readout electronics for position sensitive photomultiplier tubes. *Nuclear Science, IEEE Transactions on*, 52(1):21–27, 2005.

[135] D. P. McElroy, E. J. Hoffman, L. MacDonald, B. E. Patt, J. S. Iwanczyk, and C. S. Levin. Evaluation of performance of dedicated, compact scintillation cameras. In *Nuclear Science Symposium Conference Record, 2000 IEEE*, volume 3, pages 15–20, 2000.

[136] Hamamatsu technical data of H8500C PSPMT. 2000.

[137] N. Belcari, A. Del Guerra, M. Camarda, L. Spontoni, S. Vecchio, and D. Bianchi. Performance of a four-output front-end electronics for multi-anode PMTS readout of scintillator arrays. *Nuclear Instruments and Methods in Physics Research Section A: Accelerators, Spectrometers, Detectors and Associated Equipment*, 572(1):335–337, March 2007.

[138] V. Popov, S. Majewski, A. G. Weisenberger, and R. Wojcik. Analog readout system with charge division type output. In *Nuclear Science Symposium Conference Record, 2001 IEEE*, volume 4, pages 1937–1940, 2001.

[139] V. Popov. Matrix output device readout system, June 2004. undefinedFiling Date: 7 Dec 2001.

[140] C. J. Borkowski and M. K. Kopp. Some applications and properties of one-and Two-Dimensional Position-Sensitive proportional counters. *Nuclear Science, IEEE Transactions on*, 17(3):340–349, 1970.

[141] V. Popov, S. Majewski, and A. G. Weisenberger. Readout electronics for multianode photomultiplier tubes with pad matrix anode layout. In *Nuclear Science Symposium Conference Record, 2003 IEEE*, volume 3, pages 2156–2159, 2003.

[142] D. A. Gedcke and W. J. McDonald. Design of the constant fraction of pulse height trigger for optimum time resolution. *Nuclear Instruments and Methods*, 58(2):253–260, January 1968.

[143] M. R. Maier and P. Sperr. On the construction of a fast constant fraction trigger with integrated circuits and application to various photomultipliertubes. *Nuclear Instruments and Methods*, 87(1):13–18, October 1970.

[144] M. R Maier. A simple multifunction discriminator for multichannel triggers. *Nuclear Science, IEEE Transactions on*, 30(1):335–338, 1983.

[145] D. A. Gedcke and W. J. McDonald. A constant fraction of pulse height trigger for optimum time resolution. *Nuclear Instruments and Methods*, 55(2):377–380, 1967.

[146] V. T Jordanov and G. F Knoll. Digital synthesis of pulse shapes in real time for high resolution radiation spectroscopy. *Nuclear Instruments and Methods in Physics Research Section A: Accelerators, Spectrometers, Detectors and Associated Equipment*, 345(2):337–345, 1994.

[147] G. Sportelli, N. Belcari, P. Guerra, F. Spinella, G. Franchi, F. Attanasi, S. Moehrs, V. Rosso, A. Santos, and A. Del Guerra. Reprogrammable acquisition architecture for dedicated positron emission tomography. *IEEE Transactions on Nuclear Science*, 58(3):695–702, June 2011.

[148] A. Hemani, T. Meincke, S. Kumar, A. Postula, T. Olsson, P. Nilsson, J. Oberg, P. Ellervee, and D. Lundqvist. Lowering power consumption in clock by using globally asynchronous locally synchronous design style. In *Proceedings of the 36th annual ACM/IEEE Design Automation Conference*, pages 873–878, 1999.

[149] M. A. Tétrault, M. D. Lepage, N. Viscogliosi, F. Belanger, J. Cadorette, C. M. Pepin, R. Lecomte, and R. Fontaine. Real time coincidence detection system for digital high resolution APD-based animal PET scanner. In *Nuclear Science Symposium Conference Record, 2005 IEEE*, volume 5, pages 2849–2853, 2006.

[150] G. Franchi, N. Belcari, and A. Del Guerra. Proposta di realizzazione di sottoparti per PET. internal documentation in possession of the fiig - dipartimento di fisica - universita di pisa. 2008.

[151] G. Franchi, N. Belcari, G. Sportelli, and F. Spinella. Internal documentation in possession of the fiig - dipartimento di fisica - universita di pisa, and the bit - e.t.s.i. de telecomunicacion - universidad politecnica de madrid. 2009.

[152] C. M. Laymon, R. S. Miyaoka, B. K. Park, and T. K. Lewellen. PET Instrumentation-Simplified FPGA-Based data acquisition system for PET. *IEEE Transactions on Nuclear Science*, 50(5):1483–1486, 2003.

[153] J. Imrek, D. Novak, G. Hegyesi, G. Kalinka, J. Molnar, J. Vegh, L. Balkay, M. Emri, G. Molnar, L. Tron, et al. Development of an FPGA-based data acquisition module for small animal PET. *Nuclear Science, IEEE Transactions on*, 53(5):2698–2703, 2006.

[154] L. S. Kim and R. W. Dutton. Metastability of CMOS latch/flip-flop. *Solid-State Circuits, IEEE Journal of*, 25(4):942–951, 1990.

[155] F. H. Tenney. Idealized pulse pileup effects on energy spectra. *Nuclear Instruments and Methods in Physics Research*, 219(1):165–172, January 1984.

[156] R. Lecomte, D. Schmitt, and G. Lamoureux. Geometry study of a high resolution PET detection system using small detectors. *Nuclear Science, IEEE Transactions on*, 31(1):556–561, 1984.

[157] M. Watanabe, T. Omura, H. Kyushima, Y. Hasegawa, and T. Yamashita. A compact position-sensitive detector for PET. *Nuclear Science, IEEE Transactions on*, 42(4):1090–1094, 1995.

[158] M. O. Bedwell and T. J. Paulus. A versatile constant fraction 100 mhz discriminator. *Nuclear Science, IEEE Transactions on*, 25(1):86–92, 1978.

[159] Y. Shao, H.B. Barber, S.J. Balzer, and S.R. Cherry. Measurement of coincidence timing resolution with CdTe detectors. In *Proceedings of SPIE*, volume 41–42, page 254, 2000.

[160] Measurement of coincidence timing resolution of scintillation detectors compared to semiconductor detectors to image three-photon positron annihilation. 278(3).

[161] J.E. Arnold, A.S. Johnston, and S.M. Pinsky. The influence of true counting rate and the photopeak fraction of detected events on anger camera deadtime. *Journal of Nuclear Medicine*, 15(6):412–416, 1974.

[162] D.A.B. Bonifacio, N. Belcari, S. Moehrs, M. Moralles, V. Rosso, S. Vecchio, and A. Del Guerra. A time efficient optical model for GATE simulation of a LYSO scintillation matrix used in PET applications. *Nuclear Science, IEEE Transactions on*, 57(5), 2010', pages =.

[163] A. Del Guerra, A. Bartoli, N. Belcari, D. Herbert, A. Motta, A. Vaiano, G. Di Domenico, N. Sabba, E. Moretti, G. Zavattini, et al. Performance evaluation of the fully engineered YAP-(S) PET scanner for small animal imaging. *Nuclear Science, IEEE Transactions on*, 53(3):1078–1083, 2006.

[164] I.N. Weinberg, D. Beylin, V. Zavarzin, S. Yarnall, P.Y. Stepanov, E. Anashkin, D. Narayanan, S. Dolinsky, K. Lauckner, L.P. Adler, et al. Positron emission mammography: high-resolution biochemical breast imaging. *Technology in cancer research & treatment*, 4(1):55–60, 2005.

[165] J.L. Humm, A. Rosenfeld, and A.D. Guerra. From PET detectors to PET scanners. *European journal of nuclear medicine and molecular imaging*, 30(11):1574–1597, 2003.

[166] S.R. Cherry, J.A. Sorenson, and M.E. Phelps. *Physics in nuclear medicine*. Saunders, 2003.

[167] W.W. Moses, S.E. Derenzo, and T.F. Budinger. PET detector modules based on novel detector technologies. *Nuclear Instruments and Methods in Physics Research Section A: Accelerators, Spectrometers, Detectors and Associated Equipment*, 353(1–3):189–194, 1994.

[168] R.R. Raylman, M.F. Smith, P.E. Kinahan, and S. Majewski. Quantification of radiotracer uptake with a dedicated breast PET imaging system. *Medical physics*, 35(11):4989–4997, 2008.

[169] W. Feller. On probability problems in the theory of counters. *Courant anniversary volume*, 8:105–115, 1948.

[170] R.D. Evans and A. Noyau. *The atomic nucleus*, volume 112. McGraw-Hill New York, 1955.

[171] J.W. Muller. Generalized dead times. *Nuclear Instruments and Methods in Physics Research Section A: Accelerators, Spectrometers, Detectors and Associated Equipment*, 301(3):543–551, 1991.

[172] A.S. Radović and S. Usman. Dead-time correction for nonparalyzing detectors when measuring short-lived nuclides. *Nuclear Technology*, 157(1):106–109, 2007.

[173] J. Prekeges. *Nuclear medicine instrumentation*. Jones and Bartlett Publishers, 2010.

[174] R. Wicks and M. Blau. The effect of window fraction on the deadtime of anger cameras: concise communication. *Journal of nuclear medicine: official publication, Society of Nuclear Medicine*, 18(7):732–735, 1977.

[175] K Parodi and W Enghardt. Potential application of PET in quality assurance of proton therapy. *Physics in Medicine and Biology*, 45(11):N151–N156, November 2000.

[176] S. España and H. Paganetti. The impact of uncertainties in the CT conversion algorithm when predicting proton beam ranges in patients from dose and PET-activity distributions. *Physics in medicine and biology*, 55(24):7557–7571, 2010.

[177] X. Zhu, S. España, J. Daartz, N. Liebsch, G. El Fakhri, T. Bortfeld, and H. Paganetti. Feasibility of In-Room PET imaging for in vivo proton beam range verification. *Medical Physics*, 37(6):3180, 2010.

[178] GAP Cirrone, G. Cuttone, PA Lojacono, S. Lo Nigro, V. Mongelli, IV Patti, G. Privitera, L. Raffaele, D. Rifuggiato, MG Sabini, et al. A 62-MeV proton beam for the treatment of ocular melanoma at laboratori nazionali del Sud-INFN. *Nuclear Science, IEEE Transactions on*, 51(3):860–865, 2004.

[179] R. D. Badawi, M. P. Miller, D. L. Bailey, and P. K. Marsden. Randoms variance reduction in 3D PET. *Physics in Medicine and Biology*, 44(4):941–954, 1999.